DEFORMATION OF NANOCRYSTALLINE NICKEL BY COLD ROLLING

by

Andreas Kulovits

Magister der Physik, University of Vienna, 2002

Submitted to the Graduate Faculty of

School of Engineering in partial fulfillment

of the requirements for the degree of

Doctor of Philosophy

University of Pittsburgh

2007

UNIVERSITY OF PITTSBURGH

SCHOOL OF ENGINEERING

This dissertation was presented

by

Andreas Kulovits

It was defended on

April 3, 2007

and approved by

John A. Barnard, PhD, Professor, Department of Mechanical Engineering and Materials Science

Ian Nettleship, PhD, Associate Professor, Department of Mechanical Engineering and Materials Science

John P. Leonard, PhD, Assistant Professor, Department of Mechanical Engineering and Materials Science

Luis E. Vallejo, PhD, Professor, Civil and Environmental Engineering Department

Dissertation Director: Jörg M. K. Wiezorek, PhD, Associate Professor, Department of Mechanical Engineering and Materials Science

DEFORMATION NANOCRYSTALLINE NICKEL BY COLD ROLLING

Andreas Kulovits, Ph.D.

University of Pittsburgh, 2007

In the last few years it has become possible to produce reasonable sized metal samples with average grain sizes of less than 100nm. Concomitantly computational power has increased tremendously allowing simulation of processes in such nanocrystalline metals. Due to these new capabilities and the fact that these materials promise at least theoretically enhanced properties the scientific interest in this field has increased. As in every new area usually some discrepancies emerge during early stages of research. This study is focused on the behavior of nanocrystalline metals during plastic deformation. One size effect is that below a certain size regime for energetic reasons only one dislocation can be supported at a time by an individual grain. Work hardening in coarse grained materials is based on dislocation interactions. This raised the question, how these materials deform and whether they work harden or not.

Cold rolling of nanocrystalline electrodeposited Nickel to small, intermediate and large strains has been chosen as the model system to answer this question. An advantage of this choice is that cold deformation by rolling of Nickel has been extensively studied allowing direct comparison with the new findings for nanocrystalline Nickel. As mentioned, the material will be carefully deformed to different amounts of strain, starting with as small a strain as possible. The microstructural changes, such as micro- and macro-texture, changes in the grain boundary character and the distribution thereof, the changes in apparent grain sizes and the amount of strain stored in the microstructure will be carefully monitored by means of XRD and TEM.

Microhardness measurements will link the microstructural changes with mechanical property evolution. The results form the property measurements will be correlated to XRD and microstructural analysis. The findings will be compared to plastic deformation behavior of coarse grained Ni. An in depth discussion will be presented.

TABLE OF CONTENTS

PREFACE XV

1.0 INTRODUCTION 1

1.1 OPENING REMARKS 1

1.2 THE ROLE OF DISLOCATIONS 6

1.3 THE ROLE OF GRAIN BOUNDARIES 12

1.4 ALTERNATIVE MECHANIMS NOT BASED ON GRAIN INTERIOR DISLOCATION ACTIVITY 16

1.5 SUMMARY OF THEORETICAL FINDINGS 21

1.6 IMPORTANT KNOWN EXPERIMENTAL RESULTS 22

1.7 SUMMARY 30

2.0 EXPERIMENTAL 33

3.0 RESULTS 34

3.1 XRD / TEXTURE RESULTS 34

3.2 UNDEFORMED NC NICKEL 41

3.3 NC NICKEL 7% DEFORMED 48

3.4 NC NICKEL 16% DEFORMED 55

3.5 NC NICKEL 34% DEFORMED 59

3.6 NC NICKEL 53% DEFORMED 70

3.7 NC NICKEL 75% DEFORMED 76

3.8 GRAIN SIZE TRENDS 84

3.9 HARDNESS RESULTS 92

4.0 DISCUSSION 94

4.1 TEXTURE CHANGES 94

4.2 CHANGES IN MORPHOLOGY AND GRAIN SIZE POPULATION 101

4.3 HARDNESS MEASUREMENTS 110

5.0 SUMMARY AND CONCLUSIONS 114

6.0 FUTURE WORK 117

APPENDIX A NANOCRYSTALLINE METALS AND ALLOYS BY PULSED LASER DEPOSITION 120

BIBLIOGRAPHY 154

LIST OF FIGURES

Figure 1. Deformation mechanism map for Ni 2

Figure 2. The grain-size dependence of the flow stress. (A) Typical cell constructions used for t the simulation (B) The flow stress, defined as the average stress in the strain interval from 7 to 10% deformation. The error bars indicate the fluctuation in this strain interval (1 standard deviation). A maximum in the flow stress is seen for grain sizes of 10 to 15 nm, caused by a shift from grain boundary– mediated to dislocation-mediated plasticity. 4

Figure 3. Simulation results on the effect of grain size on changes in strain concentration: (A) 10% deformed Nc Cu with an average grain size of 49nm; (B) depicts the additional strain accumulated when increasing the strain from 10 to 11%; (C and D) Show the same for a system with 7nm average grains 6

Figure 4. Schematic illustration of the operation of a Frank Read source under an applied stress 7

Figure 5. Schematic illustrations of a grain boundary in a rectangular grain acting as a source (on the left) and the traverse motion of a dislocation through a rectangular grain leaving dislocation debris in the side boundaries (right) 9

Figure 6. Schematic illustration how the emission of multiple dislocations on parallel glide planes introduces a shear strain 11

Figure 7. Snap shots showing stress in the loading direction (σ_{yy}). White lines represent dislocation traces. (a) 0.65% strain, (b) 0.66% strain, (c) 0.69% strain 13

Figure 8. Schematic illustration how grains cluster together, locally change their orientation, eventually change the grain boundary character from high to low angle boundaries and subsequently coalesce 15

Figure 9. Schematic illustration of a core mantel model comparing relative grain boundary fractions (blue area) of a micro crystalline grain (on the left) with a nanocrystalline grain (on the right) 18

Figure 10. Schematic illustration of Core Mantel models: (a) Meyers – Ashworth model; (b) Kim et al. model 19

Figure 11. High resolution TEM images of grain boundaries in (a,b) electrodeposited nc-Ni, and (c,d) nc-Cu produced by gas-phase condensation. In all cases, crystallinity is maintained right up to the boundary and no second phase is observed. 20

Figure 12. Schematic illustration of grain boundary sliding 20

Figure 13. TEM Bright Field images of undeformed NC Co (on the left) and cold deformed NC Co after a reduction in thickness of 24%..... 22

Figure 14. XRD scans of the undeformed NC Co (black) and the deformed Nc Co (red) 23

Figure 15. FWHM as a function of true stress for the 400 reflection (left) and 222 reflection in the middle (for both curves: dark squares 1st loading; red circles 2nd loading; green triangles 3rd loading); Peak position vs. true strain (right) 24

Figure 16. TEM Bright Field with inset diffraction pattern (left) and grain size population of the undeformed NC Ni (right) 26

Figure 17. Series of Dark Field images taken at different times 26

Figure 18. Dark field images and corresponding diffraction patterns of the undeformed sample (A,B) and of a sample post deformation (C,D) 28

Figure 19. High resolution TEM image of the deformed NC Ni showing the presence of a dislocation near the grain boundary 29

Figure 20. Bright field TEM images of undeformed NC Al (a), 9% (b) and 23% deformed NC Al and weak beam dark field image of the 23% deformed sample 30

Figure 21. Collection of XRD scans of undeformed and deformed NC Ni 35

Figure 22. Peak intensities normalized by the total intensity vs. percent reduction 35

Figure 23. FWHM of different peaks vs. percent reduction 36

Figure 24. Peak position vs. percent reduction 37

Figure 25. 002 pole figures of undeformed and deformed NC Ni 39

Figure 26. 111 pole figures of undeformed and deformed NC Ni 40

Figure 27. Plan view TEM bright field images and corresponding diffraction pattern of the undeformed sample 41

Figure 28. Plan view dark field images and corresponding diffraction (the numbers indicate where dark field images were taken from) pattern of undeformed NC Ni..... 42

Figure 29. Local orientation change analysis of an area of the undeformed NC Ni: Plan view bright field TEM of several grains with nano diffraction patterns taken from the labeled grains. 44

Figure 30. Dark field image (upper left) taken with the diffraction spot shown in the diffraction pattern (upper right); the bright grain identified and outlined in the upper left dark field image is marked in the corresponding bright field image (lower left); tthe nano-diffraction (lower right) pattern of the region identified by the dark field imaging (upper left an right) is shown and corresponds to a 111 systematic row being excited, which is consistent with the spot used for dark field imaging indicated in the upper right panel. 46

Figure 31. Bright field image with grain outlines. Neighboring grains with same or similar colors indicate similar orientation 47

Figure 32. Plan view bright field (upper left), corresponding diffraction pattern (upper right), two dark field images (lower left and right)..... 49

Figure 33. Local orientation distribution measurement: Bright field image including nano-diffraction patterns form the indicated area 50

Figure 34. Dark field image (upper left) taken with the indicated diffraction vector (diffraction pattern on the upper right); bright field image (lower left) with matched region and nano-diffraction patterns of the locations labeled in the bright field image..... 51

Figure 35. Combined nano-diffraction and dark field imaging results: Bright field image with outlined grains 52

Figure 36. Local orientation distribution measurement: Bright field image including nano-diffraction patterns form the indicated area 53

Figure 37. Combined nano-diffraction and dark field imaging results: Bright field image with outlined grains 54

Figure 38. Plan view bright field (upper left), corresponding diffraction pattern (upper right) and two plan view example dark field images (lower left and right)..... 55

Figure 39. Local orientation distribution measurement: Bright field image including nano-diffraction patterns form the indicated area 56

Figure 40. Dark field image (upper left), diffraction pattern (upper right), bright field image(lower left) and corresponding nano-diffraction patterns..... 57

Figure 41. Combined nano-diffraction and dark field imaging results: Bright field image with outlined grains 58

Figure 42. Plan view bright field image (upper left) corresponding diffraction pattern (upper right) and two plan view dark field images (lower left and right) 59

Figure 43. Local orientation distribution measurement: Bright field image including nano-diffraction patterns form the indicated area 60

Figure 44. Nano-diffraction pattern including the rotation axis over which regions in the area are misoriented 61

Figure 45. Dark field image (upper left corner), corresponding diffraction pattern (upper right), bright field image (lower left corner) and nano-diffraction patterns of the corresponding area 61

Figure 46. Combined nano-diffraction and dark field imaging results: Bright field image with outlined grains 62

Figure 47. Schematic representation of the origin of moiré fringes. 63

Figure 48. Moiré fringe analysis: Bright field image including misorientation 64

Figure 49. Local orientation distribution measurement: Bright field image including nano-diffraction patterns form the indicated area 65

Figure 50. Dark field image (upper left) corresponding diffraction pattern (upper right); bright field image (lower left) and nano-diffraction patterns 66

Figure 51. Combined nano-diffraction and dark field imaging results: Bright field image with outlined grains 67

Figure 52. Local orientation distribution measurement: Bright field image including nano-diffraction patterns form the indicated area 68

Figure 53. Combined nano-diffraction and dark field imaging results: Bright field image with outlined grains 69

Figure 54. Bright field image (upper left), corresponding diffraction pattern (upper right) and two example dark field images 70

Figure 55. Dark field of a heavily defected area 71

Figure 56. Local orientation distribution measurement: Bright field image including nano-diffraction patterns form the indicated area 72

Figure 57. Combined nano-diffraction and dark field imaging results: Bright field image with outlined grains 73

Figure 58. Local orientation distribution measurement: Bright field image including nano-diffraction patterns form the indicated area..... 74

Figure 59. Combined nano-diffraction and dark field imaging results: Bright field image with outlined grains 74

Figure 60. Plane view bright field (upper left), corresponding diffraction pattern (upper right) and two dark field images 76

Figure 61. Bright field image showing large elongated regions the indicated region was investigated for local orientation differences. 77

Figure 62. Local orientation distribution measurement: Bright field image including nano-diffraction patterns form the indicated area 78

Figure 63. Combined nano-diffraction and dark field imaging results: Bright field image with outlined grains 79

Figure 64. Local orientation distribution measurement: Bright field image including nano-diffraction patterns form the indicated area 79

Figure 65. Combined nano-diffraction and dark field imaging results: Bright field image with outlined grains 80

Figure 66. Bright field image, dark field image and corresponding diffraction pattern. 81

Figure 67. Bright and dark field image and corresponding nano-diffraction pattern..... 81

Figure 68. Local orientation distribution measurement: Bright field image including nano-diffraction patterns form the indicated area..... 82

Figure 69. Combined nano-diffraction and dark field imaging results: Bright field image with outlined grains 83

Figure 70. Number fraction versus grain size to represent the change in grain size population with strain vs. size bins..... 85

Figure 71. Relative change in grain size population with strain vs. size bins..... 86

Figure 72. Change in area fraction with strain vs. size bins..... 87

Figure 73. Change in cumulative area fraction with strain vs. size bins..... 89

Figure 74. D_{ave} and D_m vs. percent reduction 90

Figure 75. Vickers micro hardness vs. percent reduction as compared to undeformed and deformed coarse grained Ni 92

Figure 76. 100, 110, and 111 pole figures of cold rolled high stacking fault Cu (top row) of cold rolled low stacking fault brass (middle row) measured by synchrotron radiation and the 100, 110 and 111 pole figures of the deformed NC Ni (bottom row) 96

Figure 77. Illustration of grain orientations when a strong cube texture is present. The colored grain areas have one cube direction parallel to the foil normal whereas the other cube directions are rotated about the foil normal 102

Figure 78. HREM image and FFT of a grain boundary showing a step in the boundary of undeformed NC Ni 104

Figure 79. . Dislocation based model schematic of a (small) low angle symmetric tilt grain boundary 105

Figure 80. Change in Vickers hardness due to a change in median grain size Dm from 26 to 68nm using data from 110

Figure 81. Backscatter SEM or BSE micrographs of Au on SiO2 thin films deposited using different background gas pressures and different substrate temperatures, scale bar is 2um (top row), 200nm (bottom row) 123

Figure 82. a) θ/2θ symmetric Bragg Brentano XRD scans, deposited at room temperature, 0 mTorr (upper), and at 500 mTorr (lower); b) 111 pole figures measured by XRD (with inset 200 pole figures) for 0 mTorr background gas (left), room temperature with 500 mTorr background (right). The highest intensities are about a factor of 5 larger than random. 124

Figure 83. Microstructure map for physical vapor deposition of gold on SiO2 for various deposition rates and substrate temperatures. Current experimental conditions are shown as crosses. 125

Figure 84. Microstructure map for physical vapor deposition of gold on SiO2 for various flux energies and substrate temperatures. Current experimental conditions are shown as crosses. 126

Figure 85. Figure 1. a) Typical energy distributions in deposition flux for DC sputtering Au (solid line) and vacuum pulsed laser ablation of Cu, adapted from. b) Mean energy of flux in PLD plume arriving at substrate positioned 40 mm from the target, adapted from. 128

Figure 86. Binary FePd phase diagram including schematic extensions of metastable phase fields, marked in dotted lines..... 133

Figure 87. Effects of deposition temperature and post-deposition annealing on normalized grain size distribution n(s)/N with N the total number of grains of PLD Fe50Pd50 (on the left) and Fe60Pd40 (on the right) on Si3N4; deposited at 300K≈25˚C=RT, at 494K≈220ºC and deposited at 220˚C with subsequent annealing for 30min at 823K ~550˚C respectively..... 134

Figure 88. θ/2θ XRD scans of the PLD Fe50Pd50 (blue curve) and Fe60Pd40 (green curve) films on SiO2 (300K substrate temperature). The excessively intense Si peak at 69˚=2θ has been blocked. 135

Figure 89. TEM bright field micrographs, inset selected area diffraction patterns; effects of deposition temperature and post-deposition annealing on microstructure of PLD Fe50Pd50 (top three images)and Fe60Pd40 (bottom three images) on Si3N4; left - deposited at 300K; middle - deposited at 494K; right - deposited at 494K with subsequent annealing for 30min at 823K, respectively..... 136

Figure 90. Grain size measurement results: Comparison of FePd on amorphous Si3N4 (blue) and (100)-NaCl (red) (number of grains normalized by the total number of measurements n(s)/N plotted vs. size regimes) 144

Figure 91. TEM of Fe50Pd50 thin films on Si3N4, a) Bright field, b) dark field and c) corresponding diffraction pattern for zero degrees of sample tilt and d) diffraction pattern for +10˚ of sample tilt; arching in the intensity of the SADP was symmetric for equal and opposite tilts about the two mutually perpendicular tilt-axis, thus indicating the presence of a fiber texture. 145

Figure 92. a) XRD symmetric Bragg-Bretano diffractogram (the strong substrate peak centered at 2θ=70.5˚, Si 400 is suppressed in this depiction), b) 111 and c) 200 as measured pole (small inset in the upper right corner) figures of FePd SiO2 (strong intensities {red} are about 8 times as large as weak intensities {black} in the case of the 111 pole figure and about 2.5 times as large in case of the 200 pole figure) 146

Figure 93. TEM of FePd on NaCl, a) Bright field, b) dark field and c) corresponding diffraction pattern. 147

Figure 94. Simulated diffraction pattern of FePd on NaCl (on the left) as compared to inverted measured TEM diffraction pattern. 149

Figure 95. Schematic depiction of possible lattice matching and atom configurations for the FePd on NaCl thin film. Schematic depiction of a) the NaCl and FCC FePd unit cells in cube orientation; b) the lattice matching for the 45 degree rotated lattices in cubeplane normal; c) angular range of arches associated with the 020 reflections in the experimental TEM diffraction pattern of about 16˚. 152

PREFACE

To

My Parents and my Grandmother

And all my

Advisors

1.0 INTRODUCTION

1.1 OPENING REMARKS

The study of plastic deformation of metals and alloys has always played a very important role in the field of Materials. The mechanisms by which materials deform mainly depend on three quantities: The temperature T (or homologous temperature T/T_m with T_m = melting temperature) at which the material is deformed; the applied stress σ (or normalized tensile strength σ/μ with μ = shear modulus); and the strain rate $\dot{\varepsilon}$ at which the deformation is performed. If any two of these quantities are fixed the third is determined as well. Based on this concept deformation mechanism maps can be created. Figure 1 shows an example of a deformation mechanism map, which has been obtained by experiment [1]. The normalized tensile stress is plotted as a function of the homologous temperature. The various lines delineating fields related to different dominant deformation mechanisms are iso - strain rate lines or lines of constant strain rate. Points of abrupt slope change for the lines of constant strain rate indicate a change in rate dominating mechanism.

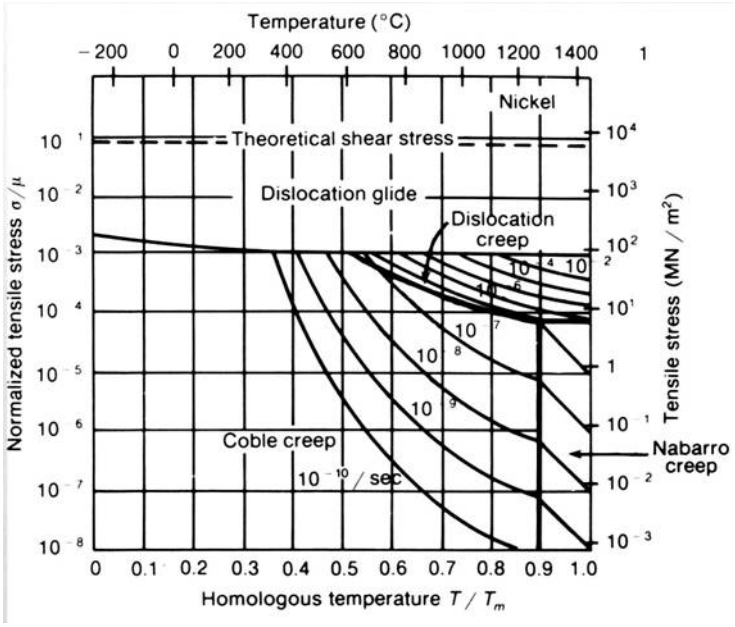

Figure 1. Deformation mechanism map for Ni [1]

Analyzing the map in this way, regions of different deformation conditions can be determined where one mechanism is kinetically dominant. What tends to be neglecting in discussing the deformation mechanism maps is that they are calculated and/or experimentally determined for a given materials for very specific microstructures. In the figure caption it is already indicated that this particular map (Figure 1) was determined for Ni with a specific average grain size of 20µm. The boundaries between the fields for the different deformation mechanisms can shift considerably for the same material with different microstructures, for example different grain sizes. Microstructural properties strongly influence plastic behavior. The Yield stress and related properties depend on texture, amount of work hardening, solute concentration, presence and concentration of precipitates, grain size etc.. The famous empirical Hall Petch relationship [2] expresses the functional dependency of the Yield Stress and the average grain size.

$$\sigma_{Y.S.} = \sigma_0 + K(D)^{-n}; n \approx \frac{1}{2}$$ Equation 1

($\sigma_{Y.S.}$ = Yield strength, D = average grain size, σ_0 and K = constants). This empirical relationship, which can be rationalized via a dislocation pile up model [2], is the reason why extensive research in grain refinement has been conducted in the past and up to this point. The common and obvious implication of the relationship expressed above is that the smaller the grain size is, the higher the yield stress is. Depending on the prefactor K, the Hall-Petch slope, considerable increases in yield stress are expected if grain refinement from the typical range of 10^1 μm to the range of 10^{-1} μm or smaller can be established via processing of polycrystalline solids.

As technology improved, various different techniques have been developed that allow the production of materials with average grain sizes of several hundred nanometers (nm) and below. Severe plastic deformation techniques such as Equal Angular Channel Pressing (ECAP) or High Pressure Torsion (HPT) techniques allow grain refinements of pure metals to average grain sizes around 150nm. Thin film deposition techniques and electro-deposition techniques can yield metal samples with average grain sizes well below 50nm. At the same time new testing methods like nano indentation or miniature tensile test aperati have been developed that require smaller and smaller samples. Along with the improvement of manufacturing techniques investigations of mechanical properties of these materials became not only possible but also raised the interest.

Parallel to the development of new processing techniques computers and computational techniques and methods improved considerably. As a result it became possible to use Molecular dynamics calculations to simulate dynamic behaviors of assemblies of nanocrystalline grains, providing insight into basic phenomena occurring when plastically deforming them. Use of

computer simulation for the study of the change in Yield stress as a function of grain size of virtual nanocrystalline (NC) aggregates of metals provided some astonishing findings. Studies showed that with decreasing grain size the yield stress first increases as predicted by the Hall-Petch relationship. Subsequently, the yield stress reaches a peak value at a critical grain size, followed by a yield stress plateau or even a decrease for further reduction in NC grain size [3],[4],[5].

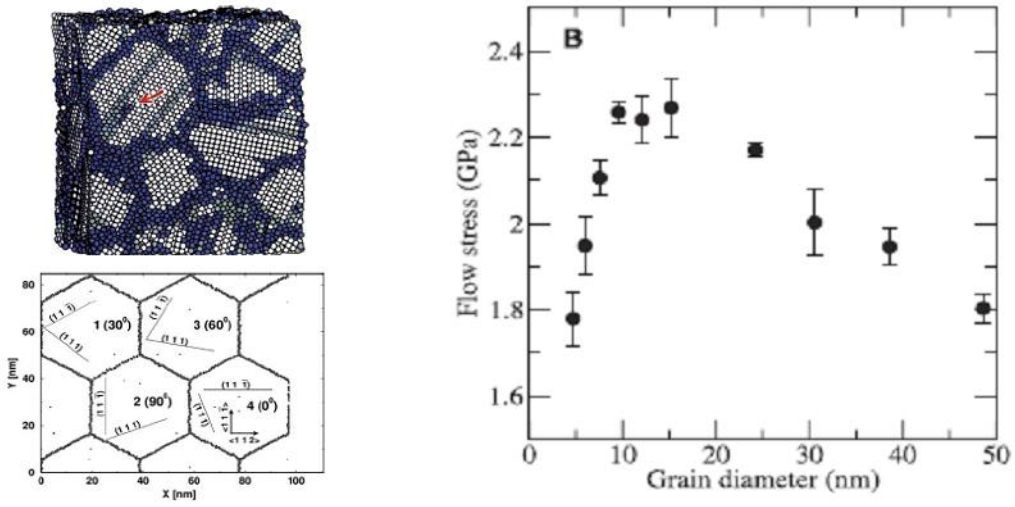

Figure 2. The grain-size dependence of the flow stress. (A) Typical cell constructions used for the simulation [6] (B) The flow stress, defined as the average stress in the strain interval from 7 to 10% deformation. The error bars indicate the fluctuation in this strain interval (1 standard deviation). A maximum in the flow stress is seen for grain sizes of 10 to 15 nm, caused by a shift from grain boundary– mediated to dislocation-mediated plasticity [3].

The apparent decrease of the yield stress, flow stress, the stress required to initiate and to maintain plastic deformation in NC metals, is often referred to as the inverse Hall-Petch behavior. This behavior is unique to NC materials, systems with increased internal atom to grain boundary atom ratio. The graphs of simulated and experimental data sets reproduced from the literature in Figure 2 illustrate this unexpected behavior of NC metals [7], [8]. The simulation

results displayed in Figure 4 have been obtained from molecular dynamics calculations. Unfortunately calculations have to invoke extremely high strain rates (at least about 10 orders of magnitude higher than typical experimental rates) along with very low total strains (only a few percent) in order to keep computational time reasonable. This considerably limits the interpretation of the interesting results. How and to what extent experimentally accessible conditions can be related to and compared with the interesting molecular dynamics simulation results remains a question that has to be approached with great caution. Regardless of these fundamental limitations, the molecular dynamics simulations qualitatively predict an apparent 'softening', a decrease in flow stress, for NC metals with critical or sub-critical average grain sizes. Interestingly, this inverse Hall-Petch behavior and the existence of a peak strength and critical grain size of NC metals have also been observed in some experimental works, supporting the predictions of molecular dynamics simulations [4], [5]. In summary these early findings seem to indicate that the mechanism by which the NC material facilitates plastic deformation changes as a lower limit in grain size is crossed. They also show that for decreasing grain size increasingly shifts the deformation affected areas from the grain interior towards and into the grain boundaries [3].

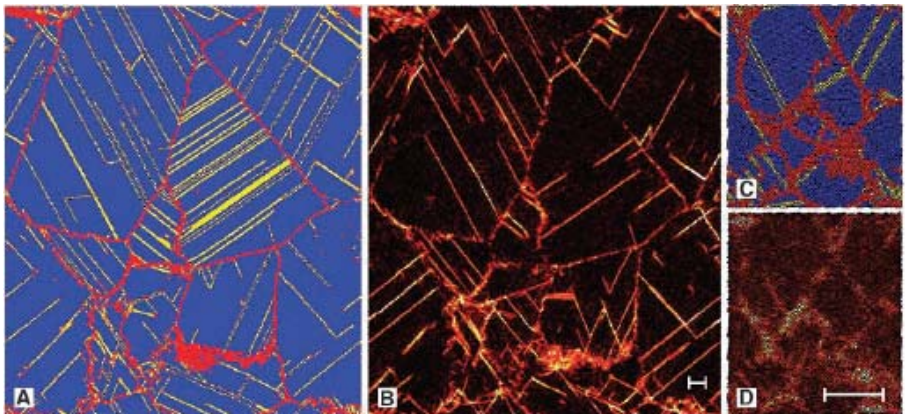

Figure 3. Simulation results on the effect of grain size on changes in strain concentration: (A) 10% deformed Nc Cu with an average grain size of 49nm; (B) depicts the additional strain accumulated when increasing the strain from 10 to 11%; (C and D) Show the same for a system with 7nm average grains [3]

Figure 3 shows the change in strain localization if the average grain size is reduced from 49nm to 7nm.

1.2 THE ROLE OF DISLOCATIONS

These findings triggered a discussion as to what extend the knowledge for coarse grained materials can be applied or at least be adapted to explain and perhaps predict the mechanical and deformation behavior of NC metals. What could be the alternative deformation mechanism? The Hall Petch relationship can be explained using a glide dislocation pile up model. Can the alternative mechanism still be based on glide dislocation mechanisms? Can glide dislocation source operation and general glide be suppressed? What is and how does the dislocation density evolve in these materials during plastic straining?

Some of these questions can be answered by simple estimates using established theories. In coarse grained metals dislocation networks are stabilized through the mutual interactions of the dislocations contained in the grains. Dislocations form self stabilizing networks. For the

extremely small grains in NC metals, however, the presence of more than one dislocation at a time is energetically very unfavorable. The resulting stresses to support two or more dislocations can be shown to even exceed the fracture stress and would make the grain highly unstable. This important conclusion constitutes one of the major differences between coarse grained and nanocrystalline metals. Moreover a single dislocation will most likely disappear into a nearby grain boundary due to line tension arguments.

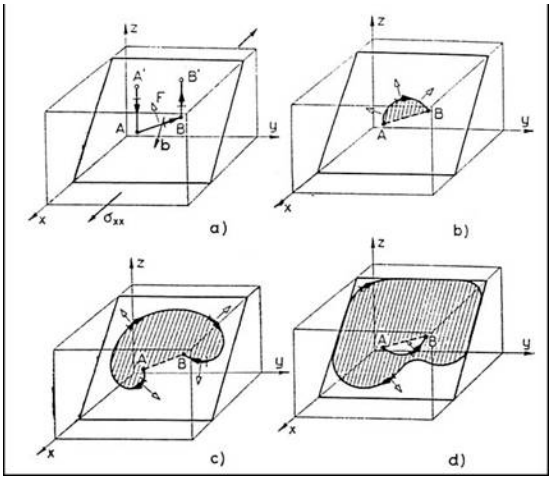

Figure 4. Schematic illustration of the operation of a Frank Read source [9] under an applied stress

If as a result the grain interiors are essentially dislocation free, what source mechanisms can operate and what stresses are required to operate them? Hence the question, whether dislocations even operate below a certain grain size, created more and more interest. In coarse grained materials pinned dislocation segments can start bowing out and multiply by operating in a Frank Read type mechanism [9]. However, this and other mechanisms rely on the presence of pre-existing dislocations within the grain interiors of the grains of the polycrystalline aggregate. As in NC metals the dislocation density was originally assumed and later found to be rather low, the grains essentially being dislocation free [3], [10], [11], these sources are very unlikely to operate.

The stress to operate a source is inversely proportional to the separation between the two pinning points [9]

$$\tau \approx \frac{2\alpha\mu b}{L} \qquad \text{Equation 2}$$

(τ = shear stress; μ = shear modulus, b = Burgers vector and L the length of the dislocation segment, a = constant that describes the dislocation character). Even if a dislocation line segment was present in grains of a NC metal, it would require stresses in the order of several GPa's to operate the source, since the maximum Frank Read source size, L above, is limited by the grain diameter. A proposed alternative mechanism is that the grain boundary acts as a source mechanism. In other words the dislocation line segment that bows out under an applied stress is in the grain boundary. As the segment bows out it travels across the grain by glide and eventually disappears into the opposite boundary segment (Figure 5) [11]. Grain boundaries can act as dislocation sources and sinks. In the absence of easily activated dislocation sources, for instance the Frank-Reed type, pre-existing in the grain interiors the grain boundary sources are critically important for plasticity in NC metals. It should be mentioned at this point that every time a dislocation is emitted from a source the grain boundary segment from which the dislocation was emitted will likely change, since it is rare to expect these sources to be perfectly regenerative. Concomitantly every boundary segment that acts as a dislocation sink also will change its character upon deposition of the glide dislocation segments into it.

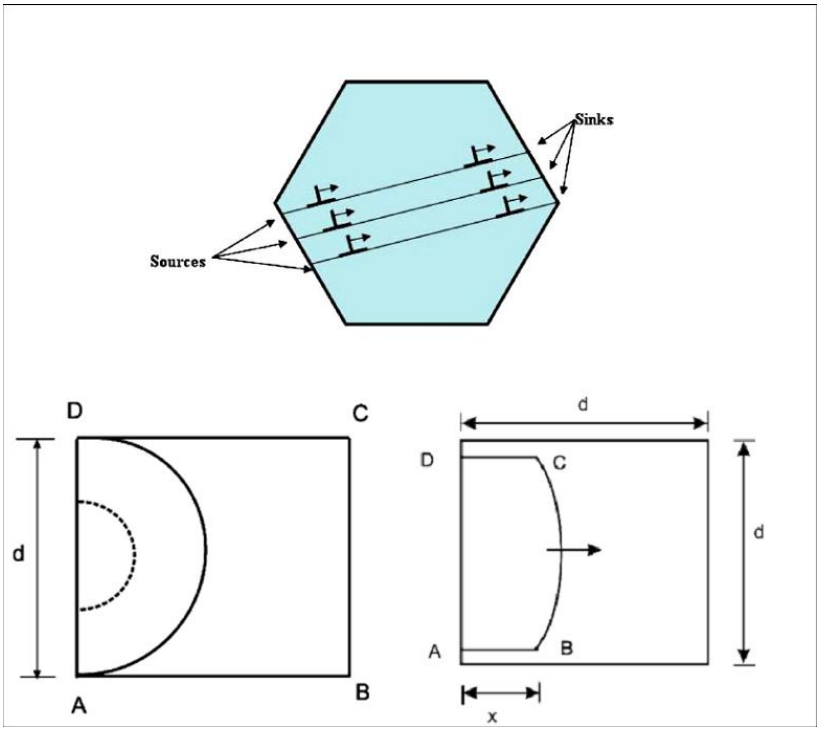

Figure 5. Schematic illustrations of a grain boundary in a rectangular grain acting as a source (on the left) and the traverse motion of a dislocation through a rectangular grain leaving dislocation debris in the side boundaries (right) [11]

In other words in NC metals glide dislocations interact with grain boundaries rather than with other dislocations as is typically the dominant mechanism of defect-defect interactions in CG metals. At best the length of the line segment that forms a dislocation source of length L, the source size, can be on the order of the grain size L ~ D (D = grain diameter). Hence,

$$\tau \approx \frac{2\alpha\mu b}{D} \qquad \text{Equation 3}$$

Using μ = 76GPa = 7.6 10^5N/cm^2 as the shear modulus and a = 3.52 A = 3.52 10^{-8}cm the lattice constant for Ni and α =0.5 for a rough "back of the envelope" estimation yields shear stresses of τ ~ 1.9GPa for 10nm sized grains and τ ~ 3.8GPa for 5nm sized grains. Using an average Schmid

factor or inverse of the Taylor factor of 0.31 (appropriate for a random grain orientation distribution FCC metal) these shear stresses imply that stresses on the order of ~6GPa to 12GPa are required to produce yielding by Frank Read source mechanism based dislocation generation and glide. As indicated before these stresses appear to be rather high but they are actually still smaller than the theoretical strength. Also, the Burgers vector of a single dislocation with $\vec{b} = \frac{1}{2}\langle 110 \rangle$ and $\left|\vec{b}\right| \approx 0.25nm$ introduces a strain of ~2.5% into a 10nm grain. A one time operation of one dislocation sources can accommodate a large amount of strain and possibly lead to considerable lattice rotation in order to minimize the acting resolved stresses. Thus, just as in coarse grained (CG) metals dislocation glide in nanocrystalline metals should result in texture changes during plastic deformation, both for the local and global texture. Figure 6 illustrates how the emission and subsequent glide introduces a shear strain into an idealized rectangular grain [11]. It can be seen that induced by subsequent dislocation glide on parallel slip systems the grain boundary character changes along with the shearing of the grain shape. The way this grain is depicted it appears to be unconstrained or isolated. In reality it will be surrounded by other grains, linked to its neighbors across the grain boundaries they share and thus experience some complex constraint from its surroundings.

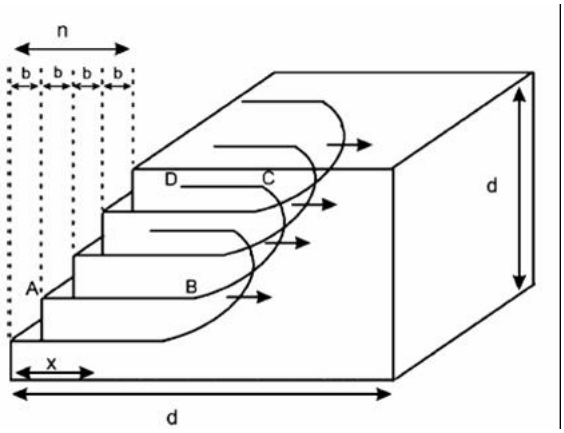

Figure 6. Schematic illustration how the emission of multiple dislocations on parallel glide planes introduces a shear strain

Hence, accommodation of the externally applied deformation by dislocation source operation and glide results in a shear strain which will simultaneously cause a rotation of the grain. Due to this dislocation interaction with the grain boundaries neighboring grains are going to change their orientation with respect to each other at the very least. Do they actually come closer in orientation? Could grain coalescence occur? As depicted in Figure 3 the boundaries can also act as sinks. How does the grain boundary change when a dislocation is absorbed? How does their character change? Clearly, given the small dimensions of the average grain in NC metals small numbers of dislocations emanating from a source, for instance those unidentified sources proposed to exist in grain boundaries, gliding through and being absorbed into the opposite side grain boundary segments can result in considerable grain boundary character change. For example, considering for simplicity a 10nm side length cubic shape Ni grain we find that 10 edge dislocations with b = 0.25nm being incorporated into an existing grain boundary evenly spaced by D = 1nm produce an additional tilt of about b/D = 0.25 rad ~14 degrees. Can high angle boundaries turn into low angle boundaries and concomitantly lower the systems free energy?

In the very least this proposed model shows that the operation of dislocation mechanisms is at least feasible. Some experimental studies also confirmed the presence of dislocations after plastic deformation of NC Ni [12]. It also shows that grain boundaries become more important for the deformation behavior of NC metals than they are in their coarse grained counterparts. Another question that immediately arises is if and how these materials accomplish work hardening. If only one dislocation at a time can be present in a grain traditional work hardening mechanisms based on interactions between gliding dislocations and between gliding dislocations and immobile or forest dislocations cannot function. Work hardening in coarse grained materials can be explained by dislocation interactions, source operations and a concomitant increase in dislocation density. These mechanisms are not available in NC metals. What is available, are dislocation interactions with grain boundaries. Could change in texture facilitated by these boundary dislocation interactions to minimize the resolved shear stress alone lead to observations that might be interpreted as work hardening? Alternatively, do NC metals not work harden at all? What other mechanisms could lead to work hardening? Analyzing the dislocation grain boundary interactions might provide answers to these questions.

1.3 THE ROLE OF GRAIN BOUNDARIES

In the discussion above the increased importance of grain boundaries was already indicated. As the grain boundary content is rather enhanced in these materials it is obvious to conclude that grain boundaries should play an important role. A semi-discrete continuum elasticity based simulation study by D.H. Warner and J.F. Molinari [13] provides a useful visualization of how plasticity is mediated through grain boundaries and illustrates some aspects

of their importance for the deformation behavior. The paper by Warner and Molinari assumes that glide of dislocations is responsible for the accommodation of the externally applied strain and the genesis of slip in the polycrystalline sample. In their simulation, they compare slip in an Al single crystal with polycrystalline Al. Figure 7 shows that a dislocation, which traveled through a grain, produces stress concentrations in and across the boundaries causing successive dislocation reactions and activity in the neighboring grains.

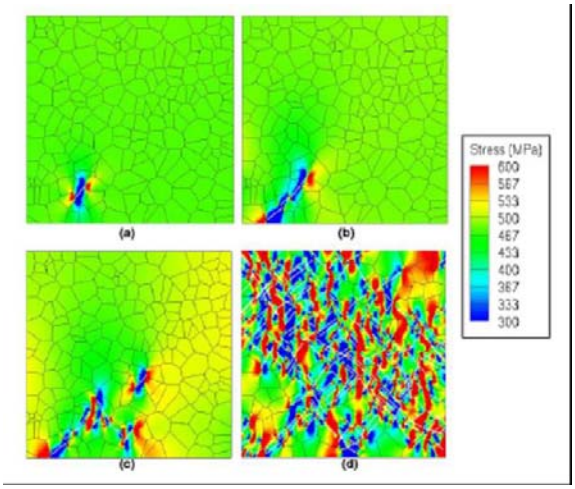

Figure 7. Snap shots showing stress in the loading direction (σyy). White lines represent dislocation traces. (a) 0.65% strain, (b) 0.66% strain, (c) 0.69% strain [13]

The internal stresses that develop as straining continues are not distributed homogeneously but rather very much concentrated in the vicinity of the grain boundaries. Also, assuming linear elasticity theory, the stress fields generated by dislocation pile-ups or the debris that they leave behind at grain boundaries due to transfer across the grain boundaries are known to decrease with increasing distance as:

$$\sigma_{dislocation} \approx \frac{1}{r} \qquad \text{Equation 4}$$

To what extend the stress will concentrate in the boundary, i.e. how easy the dislocation can pass from one grain to the next and overcome the boundary, will depend on the nature of the boundary and the orientations of the neighboring grains with respect to each other, i.e. the local texture.

This work clearly confirms that plastic deformation is a global event. Which mechanism operates locally is obviously still important but the way how the microstructure changes globally cannot be ignored. Do dislocations traveling through grains transform grain boundaries more and more into insurmountable obstacles? Is grain boundary hardening a possible work hardening mechanism in NC metals? How do grain boundary characters change upon emission and absorption of dislocations? How do grain orientations of neighboring grains change? Or do grains initially cluster together, by whatever mechanism, come closer in orientation, change grain boundary character, i.e., turn high into low angle boundaries and eventually coalesce? This behavior would rather lead to a reduction in obstacle density. Dislocations could travel more easily; at least initially the result of such microstructural changes related to the grain boundary structure or character would be expected to be mechanical softening.

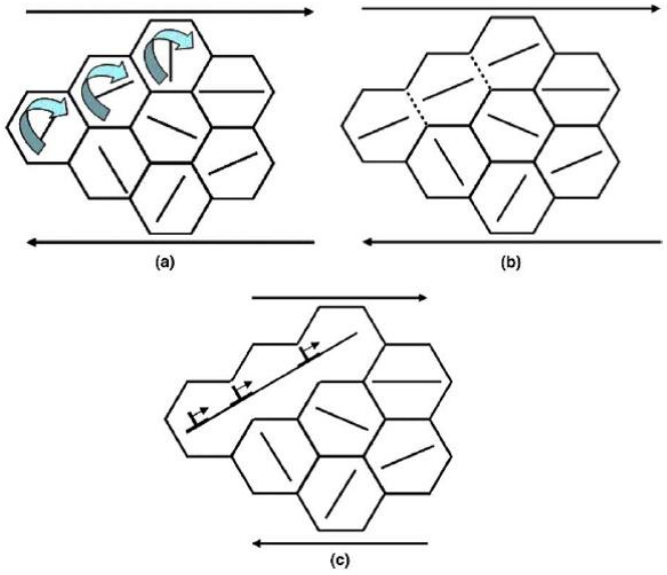

Figure 8. Schematic illustration how grains cluster together, locally change their orientation, eventually change the grain boundary character from high to low angle boundaries and subsequently coalesce [11]

Figure 8 shows a schematic illustration of a possible coalescence mechanism, driven by plastic deformation. If coalescence is truly operating during plastic deformation, which grains cluster together? Does a local correlation in orientation already exist prior to deformation? Or do different unrelated neighboring grains experience different resolved shear stresses, reorient themselves accordingly but eventually end up with similar orientations?

If a coalescence mechanism is indeed operating the average grain size should increase and also the texture has to change. Both are global rather than local events. As mentioned above, so far investigations have not paid much attention to global changes in the populations of grains comprising the NC metal aggregates. Hence, one motivation of this study is the experimental determination of global changes in the relevant microstructural parameters during deformation to high strains rather than a focus on local events typically utilized for studies of the yield stress to grain size relationships and the experimental discovery of unusual deformation mechanisms. In a

second part a correlation of the influence of these global changes of microstructure in response to deformation on micro-hardness has been studied and discussed.

1.4 ALTERNATIVE MECHANIMS NOT BASED ON GRAIN INTERIOR DISLOCATION ACTIVITY

As introduced above one major difference of NC metals as compared to coarse grained metals is that only one dislocation can exist in a grain below a certain size at the stress levels which are typically measured during deformation. This observation implies a strain rate limit above which dislocation mediated plasticity alone cannot accommodate the external applied stress and the rate at which it is applied. Molecular dynamics studies have proposed atomic rearrangement in the grain boundaries as alternative and competing mechanisms. Considering this upper rate limit a very simple approximation can be made. In analogy to coarse grained materials, based on dislocation mediated slip and to first approximation the strain rate can be approximated by the Orowan equation

$$\dot{\varepsilon}_{ext} = \rho_m b v_d \qquad \text{Equation 5}$$

($\dot{\varepsilon}_{ext}$ = the externally applied strain rate, ρ_m the density of mobile dislocations, b the magnitude of the Burgers vector and v_d the average velocity of mobile dislocations). In first approximation, the maximum dislocation velocity can be assumed to be comparable to the speed of sound (~300m/s). One dislocation per 10nm grain (assuming an average grain size ~ 10nm) yields a dislocation density ~ $10^{16}/m^2$ or ~$10^{12}/cm^2$. In comparison to coarse grained metals such a

density would correspond to a highly deformed material. In reality the density might be lower, maybe only one dislocation every hundred or thousand or ten thousand grains. The mobile dislocation density in that case would correspond to $10^{14}/m^2$ or $10^{10}/cm^2$, $10^{13}/m^2$ or $10^{9}/cm^2$, $10^{12}/m^2$ or $10^{8}/cm^2$. Further assuming the dislocations to be unit dislocations and the material to be Ni, a very crudely estimated rate of

$$\dot{\varepsilon}_{ext} \approx 10^{9} / s \qquad \text{Equation 6}$$

could still be accommodated by dislocation mediated plasticity for a mobile dislocation density of $10^{10}/cm^2$. As long as the externally applied strain rate is lower than an upper limit deformation could theoretically still be facilitated by moving one dislocation at a time. Beyond that rate other processes have to take place in order to accommodate the applied deformation. This simple argument also shows why caution has to be taken when interpreting or relating some of the molecular dynamics simulation results to experimental data. As mentioned earlier the simulations still have to use rates in the order of $10^{9}/s$ or higher in order to keep the calculation time reasonable. A suppression of alternative mechanisms could also result in adiabatic heating leading to dynamic rearrangement processes (recovery). The conditions for one versus the other to happen are still unclear, because so far classical strain rate sensitivity measurements have been proven difficult. In truly NC materials as the sample geometry is still such that localization almost always occurs in early stages of deformation. Studies on UFG metals show good correspondence between experimental results and dislocation based theoretical predictions [14]. Hence, dislocation based models can still be used for at least UFG metals even though diffusional processes might be of elevated relevance as compared to coarse-grained metals.

What are some of the alternatively proposed mechanisms? The most commonly proposed alternative plasticity mechanism to be found in the existing literature is based on atomic rearrangement in the grain boundary. In special or ordered boundaries, such as low angle or twin boundaries, which can be described in terms of a dislocation models [9], [11], rearrangements are believed to be facilitated by grain boundary dislocations. In disordered boundaries, such as high angle boundaries, a dislocation model becomes unsuitable. In those boundaries atomic rearrangement can be facilitated by directional diffusion along grain boundaries and triple junctions, i.e., locations of enhanced atomic mobility. Similar to grain interior dislocation mediated plasticity, boundary rearrangements allow the grains to rotate relative to each other to accommodate the externally imposed strain in order to minimize the acting resolved stress.

Based on atomic rearrangements in the grain boundary, one of the earlier proposed models considered the existence of an extended boundary phase at the grain perimeters.

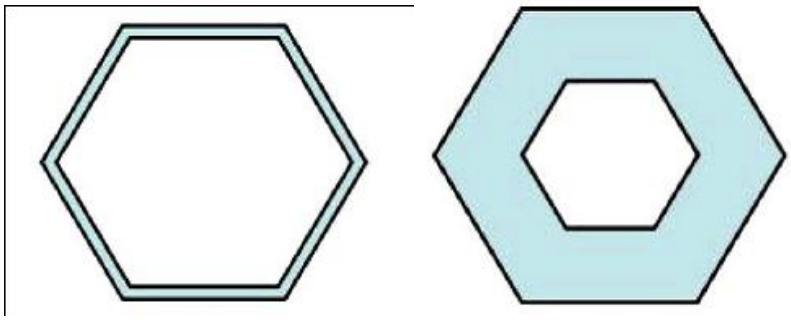

Figure 9. Schematic illustration of a core mantel model comparing relative grain boundary fractions (blue area) of a micro crystalline grain (on the left) with a nanocrystalline grain (on the right)

In this model, referred to as the Core Mantel Model [11], nanocrystalline grains are envisioned as two phase aggregates (see Figure 9). The grain interior phase and some type of randomly disordered grain boundary phase. Examples of different representations are depicted in Figure 10 [15], [16].

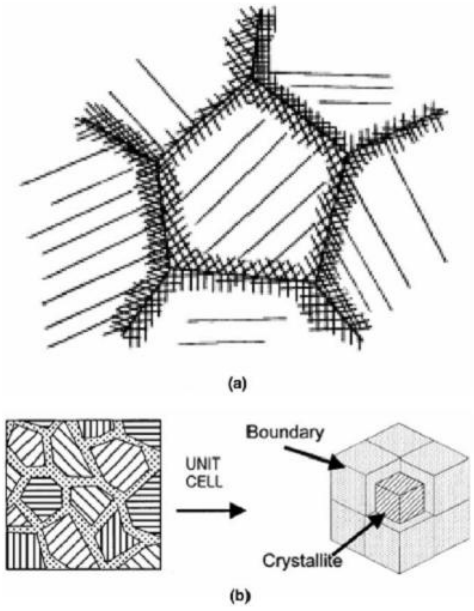

Figure 10. Schematic illustration of Core Mantel models: (a) Meyers – Ashworth model [15]; (b) Kim et al. model [16]

Like other models mentioned earlier Core Mantel models assume that the grain boundary acts as the primary source of slip. Grain boundary dislocations, grain boundary ledges are known origins for plastic deformation. As a result it is assumed that grain boundary regions harden much faster than the grain interior. There is ample experimental evidence of the development of a mantel during plastic deformation of coarse grained material [17]. Despite this applicability and successful use of such models in simulations there has been no experimental evidence of some type of amorphous phase at the grain boundaries.

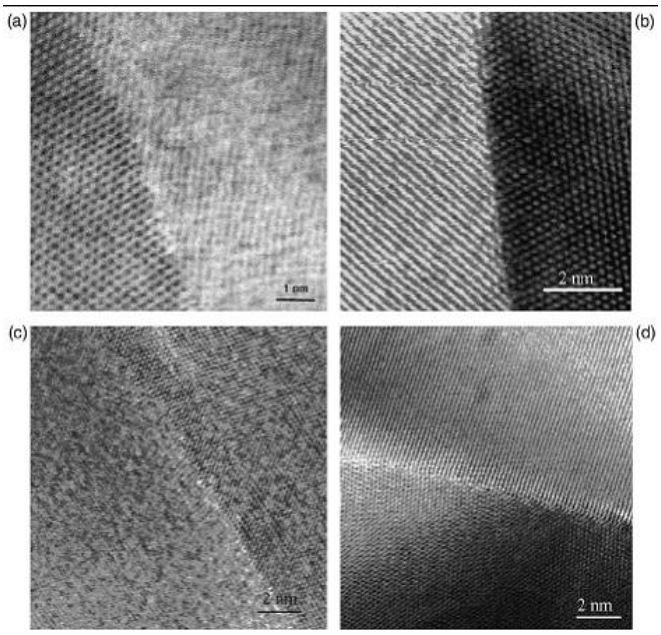

Figure 11. High resolution TEM images of grain boundaries in (a,b) electrodeposited nc-Ni, and [18] (c,d) nc-Cu produced by gas-phase condensation [19]. In all cases, crystallinity is maintained right up to the boundary and no second phase is observed.

In Figure 11 high resolution TEM images of grain boundary segments of Nc Ni [18] and Nc Cu [19] are displayed. In this two dimensional representation of grain boundaries no evidence of any disordered or non crystalline phase can be observed.

A second model is based on some type of grain sliding model. Figure 12 shows a very simplified

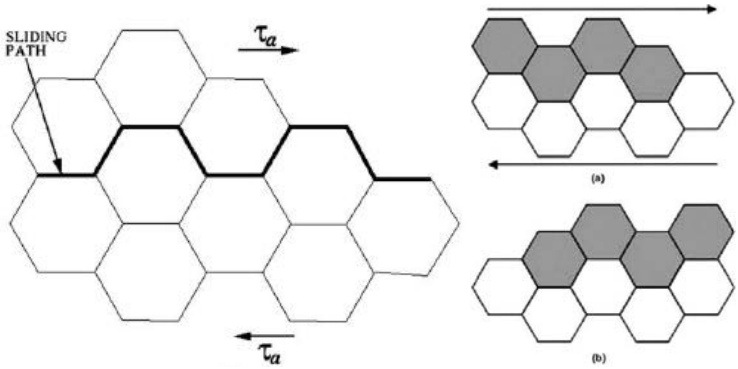

Figure 12. Schematic illustration of grain boundary sliding [11]

visualization of how grains could slide under an applied stress. Raj and Ashby assumed that plastic accommodation of adjacent grains occurred entirely by diffusive processes [19]. Simulations using the Raj - Ashby model to estimate a rate dependence on grain size [11], [20] result in sliding rates of $\dot{\gamma} \sim 10^{-4}$/s for 10nm average grain sizes in Cu. As plastic flow, not considered in this model, could also accommodate processing temperatures it was concluded that grain sliding is at least theoretically feasible for grains below 10nm. However, concerns arise when considering how coordinated such a mechanism is required to be. Several grains have to perform the same motion under an applied shear stress as depicted in Figure 12. These grains most likely start out with different orientations, if they are indeed considered individual grains. Only after large amounts of deformation, when already a considerable change in texture occurred might their orientations have become very similar. If the orientations are however significantly different, the resulting shear stresses acting on the slip systems in the grains individually can also be very different. Why than should these grains act cooperatively? However, if locally clusters of grains are already very similar in orientation, slight reorientations might be sufficient to allow grain boundary sliding.

This question can be answered if global and local texture changes are carefully analyzed.

1.5 SUMMARY OF THEORETICAL FINDINGS

Summing the previous discussion up there are two important findings of these theoretical considerations. First, only one dislocation at a time can exist in a grain interior. This raises the follow up question of how NC materials can work harden. The second important finding seems

to be the obvious conclusion that grain boundaries and the changes thereof via grain boundary dislocation interactions during plastic deformation play a decisive role. In order to investigate at least part of this important role of grain boundaries it is necessary to investigate changes in grain orientation i.e. texture, and of grain size changes. So far this evolution of deformation texture and deformation induced grain size changes have not been carefully studied. This partially motivated this study.

1.6 IMPORTANT KNOWN EXPERIMENTAL RESULTS

In the following section some example papers will be discussed that report somewhat contradictory findings. Early studies reported that no microstructural changes are observable upon plastic deformation. X. Zhang et al. deformed NC Co by cold rolling [8]. They report that upon a reduction of 24% the microstructure basically remains unchanged.

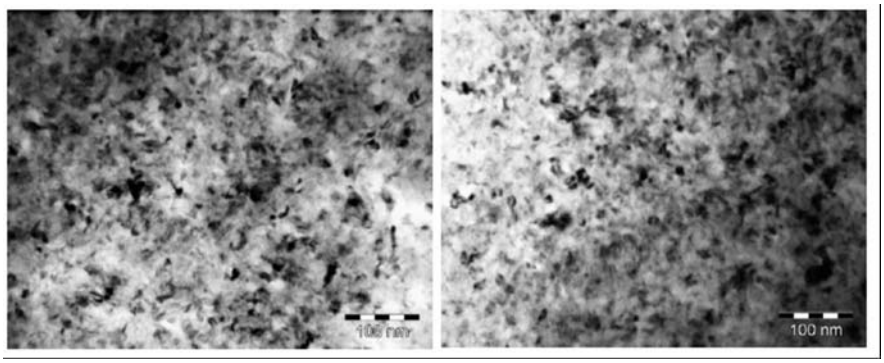

Figure 13. TEM Bright Field images of undeformed NC Co (on the left) and cold deformed NC Co after a reduction in thickness of 24% [8].

Figure 13 compares bright field images of the undeformed and cold worked NC Co. The morphologies look rather similar. However, caution has to be taken, when trying to estimate grain sizes from bright field images. Bright field imaging is rather insensitive to changes in

orientation. Very little can be said about regions of similar contrast. For bright field imaging only the un-scattered or the transmitted beam passes an aperture and is used to form an image. Areas that fulfill a diffraction condition scatter electrons at some angle rather away from the transmitted beam. All electrons of diffracted beams however are absorbed. Concomitantly these areas will appear dark [22]. Similarly equally dark areas could contain several grains that all fulfill different Bragg conditions and have hence different crystallographic orientations. Equally bright areas might contain also multiple entities of different orientation that do not fulfill any diffraction condition. Electrons that are accelerated by a 200kV have a wavelength $\lambda \sim 0.025$A. Therefore the diffraction angles are very small (in the order of 0.5°) and the range of different orientations that grains could assume and still show very similar contrast is rather large.

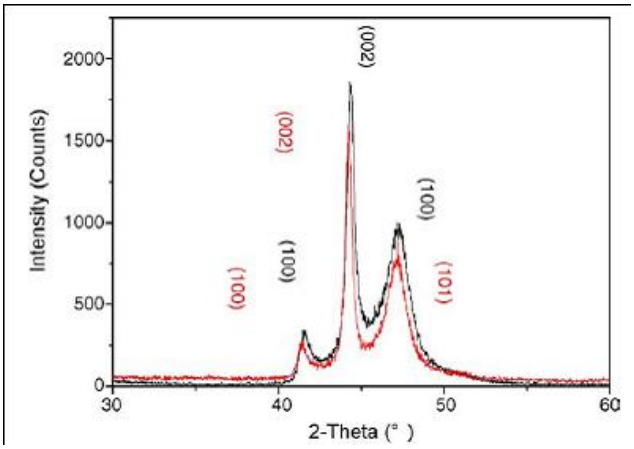

Figure 14. XRD scans of the undeformed NC Co (black) and the deformed Nc Co (red)

Aside from the TEM bright field interpretation XRD results of the same work (see Figure 14) show that the FWHM changes very little or remains essentially unchanged. An increase in average grain size would lead to a decrease in FWHM. The Bragg condition is strictly speaking derived for infinite perfect crystals. However, the smaller the diffracting volume the less defined is the diffraction condition. Therefore slightly misoriented grains can still give rise to diffraction

around the Bragg condition for the same coarse grained material leading to peak broadening [23]. Grain growth should therefore lead to a narrowing in peak broadening. However, peak broadening can also originate from storage of nonuniform strains, i.e. the presence of slightly misoriented volumes, a mosaic like structure. These volumes fulfill Bragg conditions that slightly different but still close to the Bragg condition of the defect free material adding up to a broader peak [23]. Simultaneous strain storage in the microstructure could therefore compensate the grain growth effect. As the claim that the average grain size doesn't change the only possible conclusion can be that the microstructure essentially remains unchanged upon plastic deformation. For the previously explained reason of rather poor accuracy of bright field imaging to determine grain sizes this conclusion seems rather questionable.

Another study with similar results has been conducted on NC Ni. NC Ni was plastically deformed in situ up to a strain of ~ 5% within a high energy X- ray Synchrotron source [24]. The broadness of the peaks was monitored during loading and unloading.

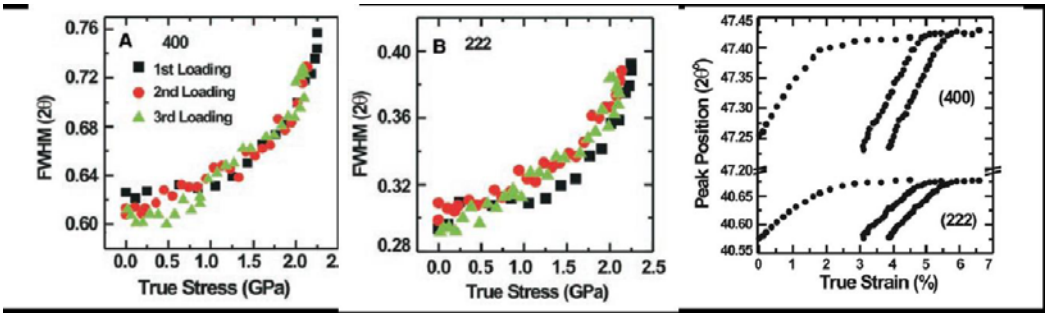

Figure 15. FWHM as a function of true stress for the 400 reflection (left) and 222 reflection in the middle (for both curves: dark squares 1st loading; red circles 2nd loading; green triangles 3rd loading); Peak position vs. true strain (right)

Figure 15 shows the main results of these measurements. As can be seen in the first to graphs the FWHM recovers to the essentially the same value after unloading even though the sample has been plastically deformed. The third graph shows that also the peak position returns to the

original value upon stress removal. A shift in peak position indicates a change in diffraction condition i.e. a change in lattice constant. Elastic strain is stored in the microstructure. The completely reversible changes in peak broadness as well as position despite permanent plastic deformation suggests, that no major changes in the microstructure occur at least up to a strain of 5%. This study is consistent with dislocation mediated plasticity. Dislocations emitted from the grain boundary traversing through grains and getting absorbed on the opposite side might not lead to some work hardening i.e. storage of measurable strain in the microstructure. However local changes such as grain rotations might take place. For these low amounts of strain the changes might be small to be detected by this method. However there might be changes. It seems to also confirm the lack of work hardening at least for these rather low amounts of deformation.

There are other studies, especially more recent works that seem to contradict the above described works and report changes in the microstructure upon plastic deformation. Z. Shan et al. performed in situ TEM straining experiments of NC Ni thin films [12]. The as deposited films exhibited for metals rather narrow grain size distribution (see Figure 16). No texture seems to have been present. The presence of a uniform rings in the diffraction pattern rather indicates a random distribution of grain orientations [25]. However to exclude the presence of fiber textures tilting experiments are required [25].

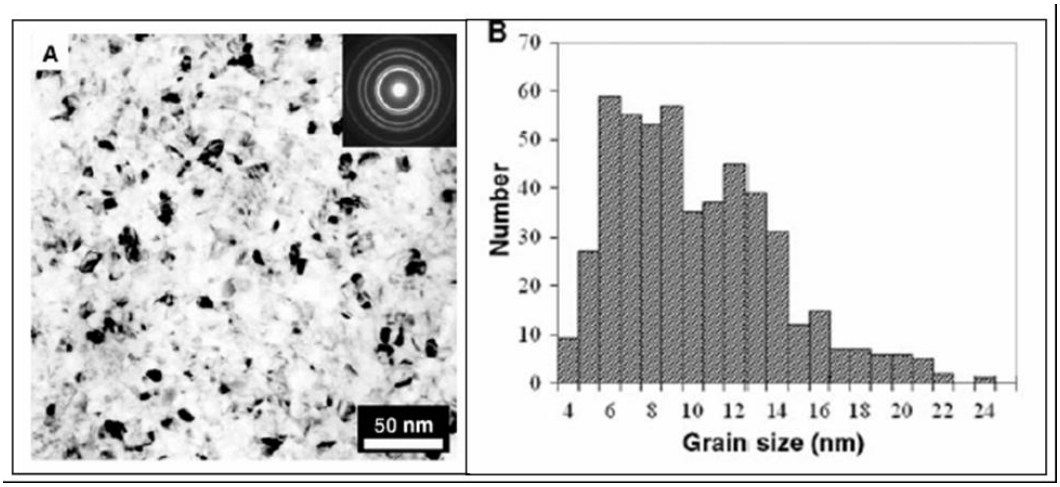

Figure 16. TEM Bright Field with inset diffraction pattern (left) and grain size population of the undeformed NC Ni (right)

A crack was introduced before the straining experiment. The plastic zone ahead of the crack tip progressing upon straining was investigated in situ.

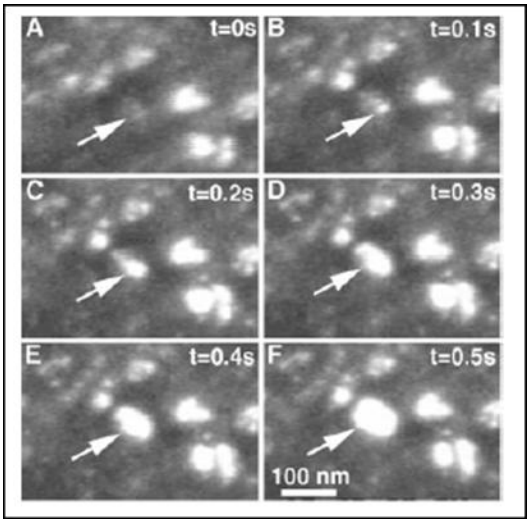

Figure 17. Series of Dark Field images taken at different times

Figure 17 shows a series of dark field images taken at different times. Dark field imaging is very suitable to monitor grain orientation changes. In difference to bright field images dark field

imaging is very sensitive to changes in crystallographic orientation. As mentioned before the diffraction angle for 200kV energy electrons is on the order of 0.5°. Minor deviations have the result that the Bragg condition is no longer fulfilled. In dark field imaging only one diffracted beam is allowed to pass an aperture whereas all other electron beams are absorbed. Hence only volumes that fulfill that particular diffraction condition will appear bright. All other regions appear dark. If the orientation of those regions only changes by a degree and Bragg's law is no longer fulfilled, and the regions turn dark. Similarly if regions rotate accordingly so that their orientation becomes such that they fulfill the diffraction condition they will start to turn bright. Such a sequence can be seen in Figure 18. It can be clearly seen that in the centre of the image a feature that is originally dark turns bright. A grain or a cluster of grains changed their orientation accordingly to fulfill the required diffraction condition. Bending of the foil can be excluded as in that case larger areas should change contrast, as the entire foil would start to rotate into Bragg condition. This important finding shows that grain rearrangement, grain reorientation takes place during plastic deformation. This behavior is very similar to what is observed in coarse grained metals.

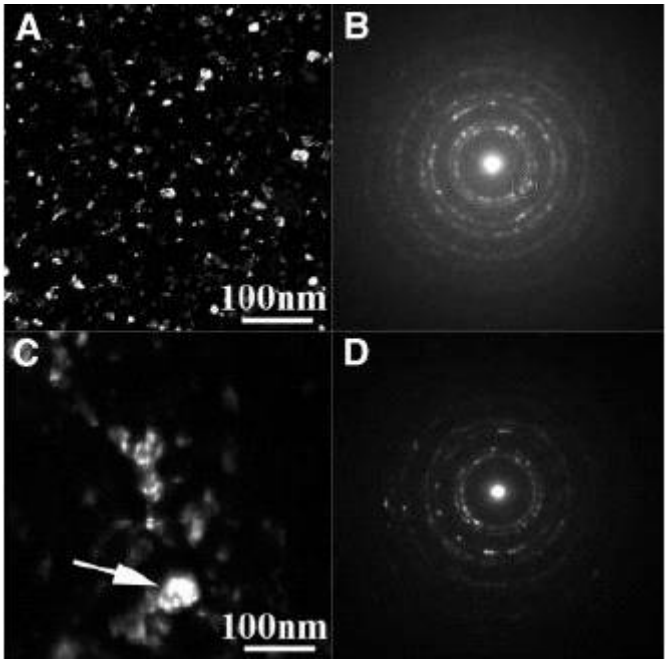

Figure 18. Dark field images and corresponding diffraction patterns of the undeformed sample (A,B) and of a sample post deformation (C,D)

As for grains that satisfy the diffraction condition appear bright, its neighbors have to appear dark if their orientations differ by a degree from that stringent Bragg condition for diffraction into the objective lens aperture. This sensitivity makes this technique very suitable to measure grain size. The dark field image (A) of the undeformed film in Figure 16 shows grains that have grain diameters below 100nm. The dark field of the deformed sample (C) shows features that are almost an order of magnitude larger. Grain growth seems to have occurred during plastic deformation. The decrease in number of diffraction spots in the diffraction patterns before (B) and after (D) the straining experiment also seems to indicate that the number of grains in the field of view decreased upon straining. This finding is consistent with a change in texture, reducing the number of grains of differing orientations. The background intensity also changed from being larger before (B) then after (D) straining. The observed change in the background intensity was considered to be consistent with shearing of the sample area by plastic deformation

in response to the displacement pulses. Another important finding was that after plastic deformation dislocations could be observed in the microstructure (Figure 19).

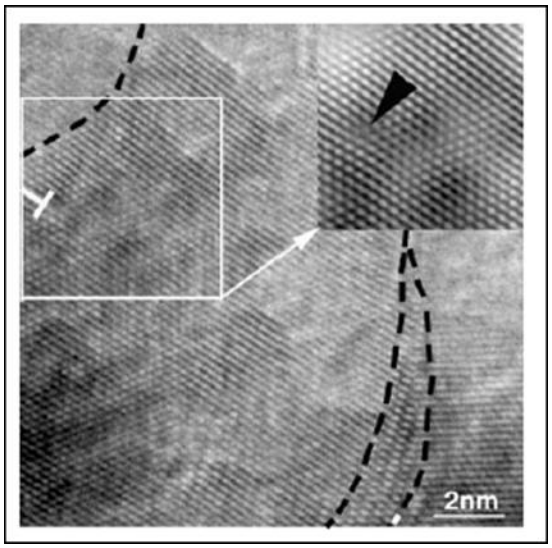

Figure 19. High resolution TEM image of the deformed NC Ni showing the presence of a dislocation near the grain boundary

Summing up the study clearly shows microstructure changes upon plastic deformation. Other more recent studies also reported changes in the microstructure upon plastic deformation. D.S Gianola et al. performed tensile tests on NC Al [26]. The Al was deformed up to a strain of 23% before failure. They report stress induced grain growth and storage of dislocations. Figure 20 shows TEM micrographs of the undeformed and deformed samples. The size of the observable features in bright field is clearly increasing. More convincing however is for reasons mentioned above the outline visible in dark field imaging

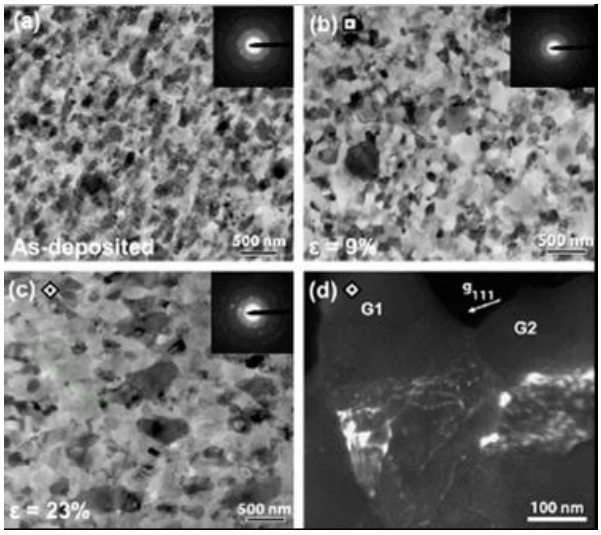

Figure 20. Bright field TEM images of undeformed NC Al (a), 9% (b) and 23% deformed NC Al and weak beam dark field image of the 23% deformed sample [26]

. The dark field image also clearly shows dislocation tangles, indicating more than one active slip system and considerable dislocation interactions similar to plasticity in coarse grained materials.

1.7 SUMMARY

The discussed papers show some of the controversy that can be found in the literature. In addition many studies focus on certain aspects of plastic deformation, like cyclic behavior [27] or creep [28]. As has been shown in the first part various different mechanisms have been proposed to operate on a local level, nicely reviewed by M.A. Meyers et al. [11], triggering lots of interest [29]. Many studies only deform to low or intermediate strains (see the studies above: [8], [24], [25], [26]).

This study does not focus on discovery or observation of the locally acting mechanism or mechanisms of deformation. It is hypothesized or proposed that NC metals have access to all the same deformation mechanisms as their coarse grained counterparts but that the deformation

conditions, T, strain rate and stress, for which a given mechanism is dominant, differ. NC Ni with a grain size larger than that corresponding to the yield or flow stress peak was investigated. The main mechanisms of deformation expected to accommodate externally imposed plastic deformation involve dislocations, even though grain boundary mediated rearrangements might also occur. One of the main differences between deformation dynamics of NC and coarse grained metals is that grains in NC metals can only support one single dislocation at a time. Different to coarse grained metals, interactions of dislocations with grain boundaries rather than other dislocations become more important. Those mechanisms are usually negligible in coarse grained metals. The implications on possible work hardening in NC metals have already been pointed out. Differences in deformation behavior up to large strains of NC Ni as compared to deformation of coarse grained Ni resulting from this finding will be discussed. Cold rolling of NC Ni has been chosen as a model system because plastic deformation of coarse grained Ni via cold rolling has been studied extensively. Comparison of the results found with behavior in coarse grained Ni was readily made. As has been explained in the previous section plastic deformation is not only a local event but even more so a global event. In difference to most studies, this work will therefore focus more on how not only the morphology of the microstructure changes but also how the local and global texture change. These microstructural changes will be linked to property changes such as changes in hardness. Another original contribution will be made by deforming to large strains via cold rolling. So far no systematic study of morphology, global and local texture changes upon deforming to small, intermediate and large strains has been conducted.

Summing up, the main goal of this study is to discuss the differences that develop upon plastic deformation in NC vs. coarse grained Ni due to the special nature of dislocation

interactions. In small grains dislocation interact mostly with grain boundaries rather than other dislocations. This behavior is different to the dominant behavior in coarse grained metal where dislocation interactions with the grain boundaries can be neglected but dislocation – dislocation interactions matter most. In short summary from the whole discussion the following objectives can be deduced:

1. Comparison of global texture studies during the cold rolling process with coarse grained Ni to reveal differences and similarities in behavior. Texture evolution in coarse grained Ni can be rationalized via dislocation interaction mediated work hardening [30]. Dislocations interacting with grain boundaries rather than other dislocations might have an effect on the resulting texture.
2. Statistical grain size analysis via systematic TEM dark field imaging analysis to show that grain coarsening is taking place.
3. Local grain orientation analysis to show indirectly the effect of dislocation interactions with grain boundaries on coarsening and subsequent work hardening mechanisms.
4. Simple estimates derived from hardness and XRD analysis will show that grain growth and concomitant storage of strain are feasible

Combining these results the study will show how dislocation grain boundary interactions lead to grain coarsening and sequentially dislocation – dislocation interactions in the larger grains to work hardening.

2.0 EXPERIMENTAL

Commercially available nanocrystalline Nickel has been used for this study. Electrodeposited NC Ni sheets 1" x 1" x 0.3mm in dimension with a nominal grain size of 20-30nm have been acquired from Goodfellow. An attempt to make NC Au by Pulsed Laser deposition (PLD) did not yield fully dense NC Au. The findings of the attempt of preparing NC Au by PLD and associated investigations are shown for convenience and completeness in Appendix A. The NC Ni has been plastically deformed by cold rolling at room temperature. The NC Ni sheets were cold rolled in subsequent passes in identical orientation to the final reduction in thickness with approximately 5-10 % reduction in thickness per pass. X-ray diffraction (XRD) and texture measurements were performed in symmetric Bragg Brentano setup using a Philips PW 1830 diffractometer with Cu-K_α radiation. For the texture measurements a two angle goniometer was used. TEM samples were prepared by electro polishing using a 5% Perchloricacid in 95% Methanol solution. The samples were polished at a temperature of -60˚C to -70˚C. A JEOL JEM2000FX operating at 200kV has been used for the TEM work. Vickers Hardness measurements were carried out using loads of 50g and 100g and a dwell time of 10s.

3.0 RESULTS

3.1 XRD / TEXTURE RESULTS

The compilation of θ/2θ scans of the undeformed and deformed NC Ni (Figure 21) show that the intensity of the 200 peaks is enhanced in the undeformed or as-received state (top scan in Figure 21). The presence of a cube fiber texture would be consistent with such an enhanced intensity in the 200 relative to the 111 peak. The plot of normalized peak intensities vs. percentage reduction (Figure 22) further assists in visualizing this texture related observation more clearly. Upon plastic deformation by cold rolling reduction the intensities of the 200 peaks decrease considerably with increasing amount of deformation, while the intensity of the 220 peak increases (Figure 21 and Figure 22). This observation is consistent with a change in texture during cold deformation relative to the starting texture. The normalized peak intensity of the 002 reflection seems to change more rapidly for about 40% reduction after a more or less slight and steady rate of decline for the smaller reductions in thickness (<40%). Concomitantly the normalized intensities of 220 reflections show a steady and slight increase and then a marked increase after about 40% reduction. A major change in texture of the microstructure took place during cold rolling reduction and becomes most significant after about 40% reduction in thickness.

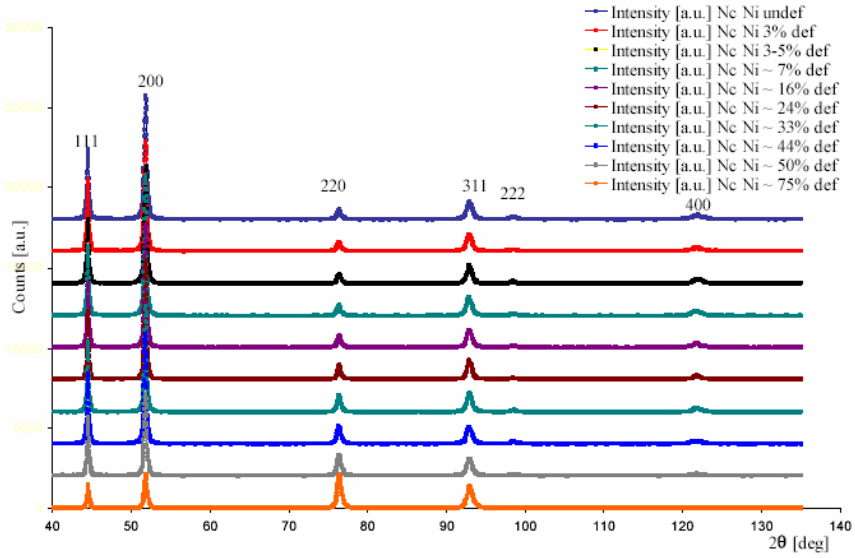

Figure 21. Collection of θ/2θ scans of undeformed and deformed NC Ni

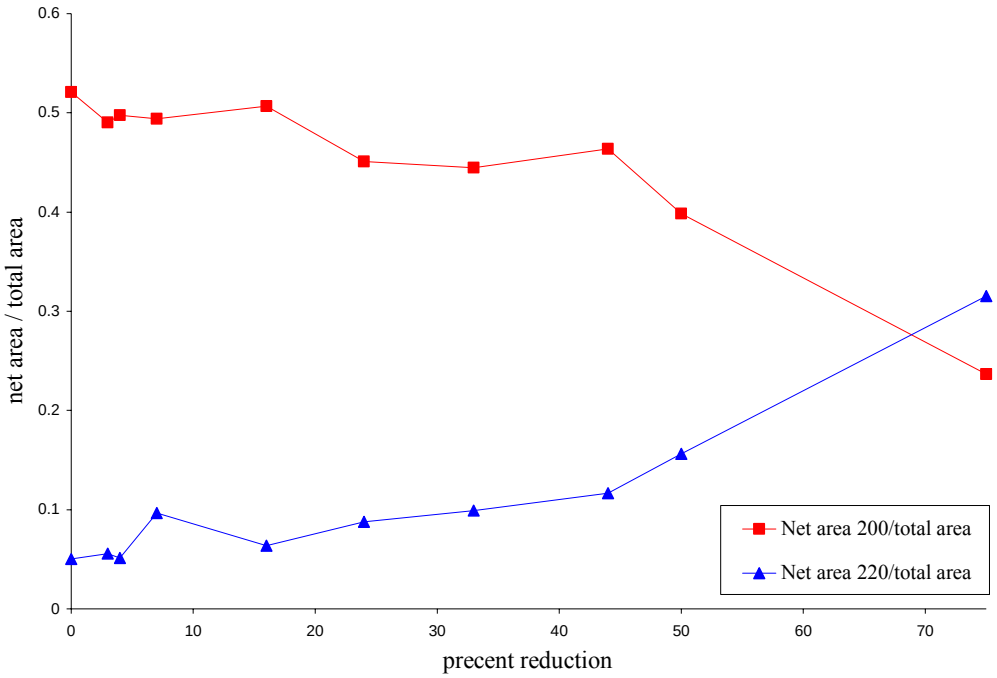

Figure 22. Peak intensities normalized by the total intensity vs. percent reduction

Figure 23 shows the change in peak broadness or more accurately the FWHM vs. cold rolling thickness reduction for different peaks. Within the error bars no change in broadness is observable. The error bars were determined by repeating the same measurement several times, including un-mounting and remounting the sample. This lack of change might be interpreted as an absence in work hardening. As discussed in the introduction, here care has to be taken when interpreting such results. Grain growth and storage of strain have opposite effects on the FWHM. Grain growth leads to a reduction of broadening, strain to an increase. Only knowledge of concomitant changes in the microstructure allows us to draw clear conclusions.

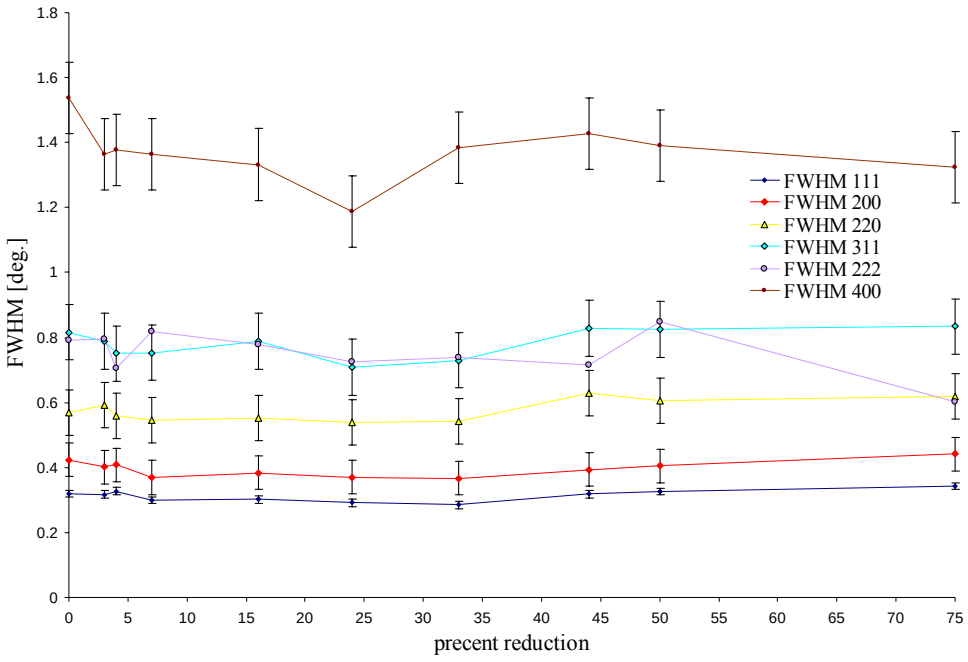

Figure 23. FWHM of different peaks vs. percent reduction

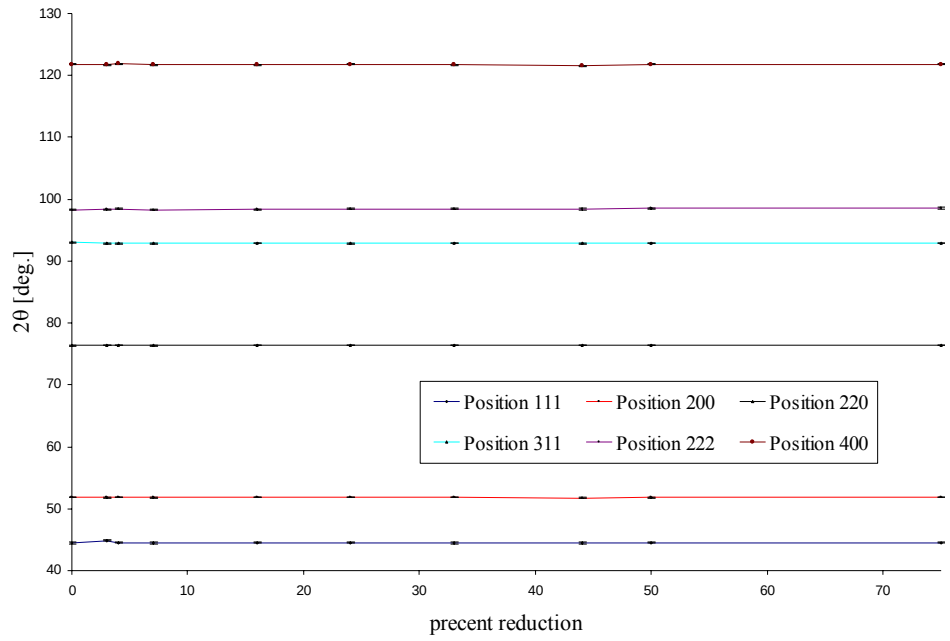

Figure 24. Peak position vs. percent reduction

Figure 24 shows the change of peak position of different peaks with increasing reduction in thickness. The error bars in the graph are too small to resolve. No change in any peak position is observable. Simple analysis of Bragg's law shows that a change in peak position corresponds to a change in lattice constant. Hence, it can be attributed to storage of uniform directional strain in the microstructure. The lack of change of the peak position implies that elastic strains that permanently distort the unit cell on average, such as hydrostatic strains, are not present in the microstructure.

In Figure 25 and Figure 26 200 and 111 pole figure measurements of the undeformed and differently deformed samples are shown. The sheets used for the measurements were squares roughly 1" x 1" in size. The pole figures are background corrected. The 200 pole figure shows a very strong intensity in the center indicating that a large fraction of the sample volume, a large number of grains assume orientations with 200 planes parallel to the foil surface. As indicated in

figures 23 and 24 the strongest intensities (red) are about 4-5 times random (black). The 111 pole figure shows an evenly distributed ring centered about a tilt angle of ~ 55° relative to the foil normal in the center of the pole figure, which is consistent with the angle between 111 and 200 type planes. The random rotational distribution of 111 orientations at 55° confirms the presence of a 200 fiber texture [31]. The cube plane normal is consistent with the fiber axis. The 111 plane normals are equally distributed around that fiber axis. Both the 200 and the 111 pole figures indicate an onset of change in texture at about 16% reduction. After 44% deformation another major change in texture is observable, consistent with observation made upon analyzing the change in normalized peak intensities vs. percent reduction (Figure 22).

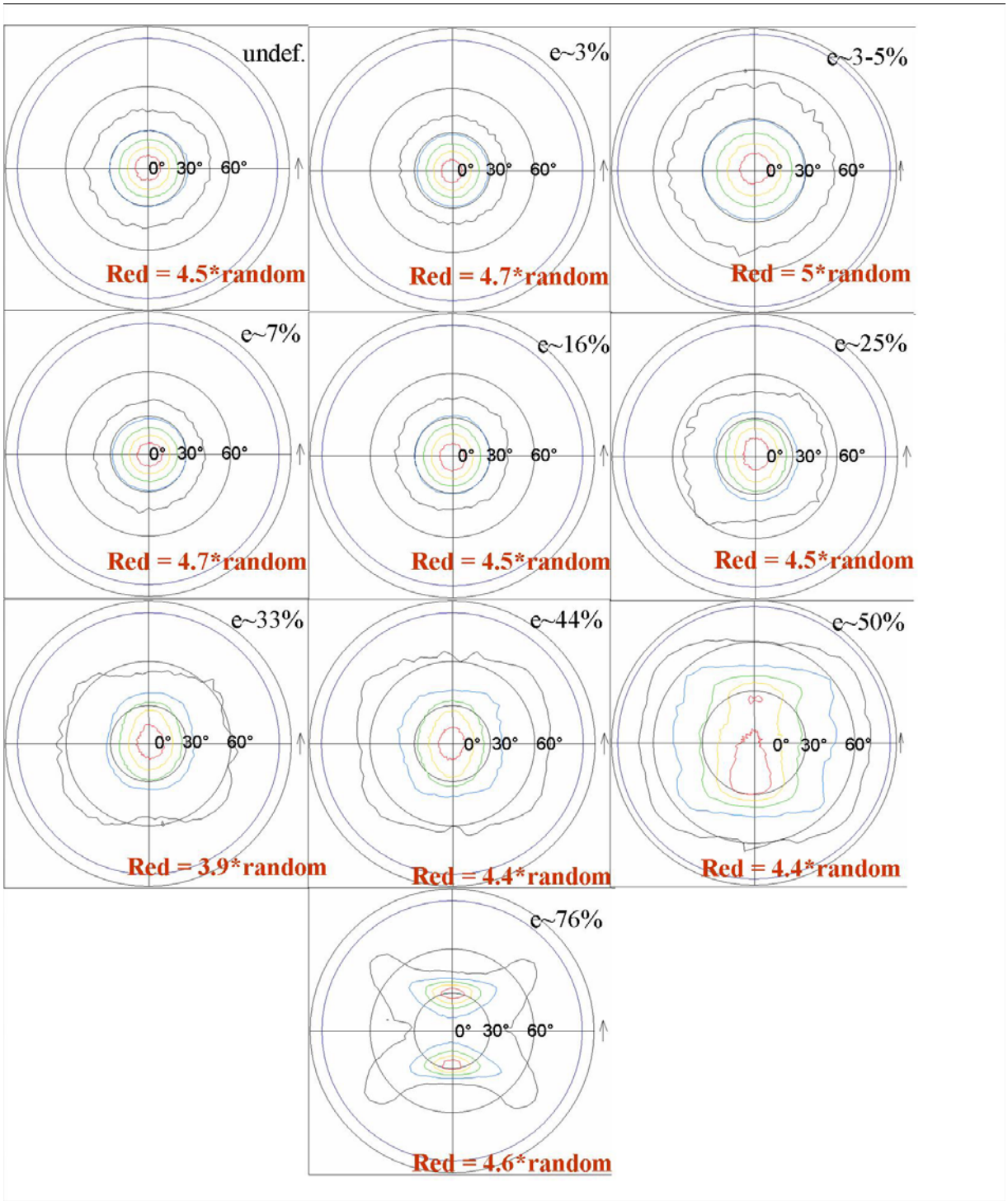

Figure 25. 002 pole figures of undeformed and deformed NC Ni

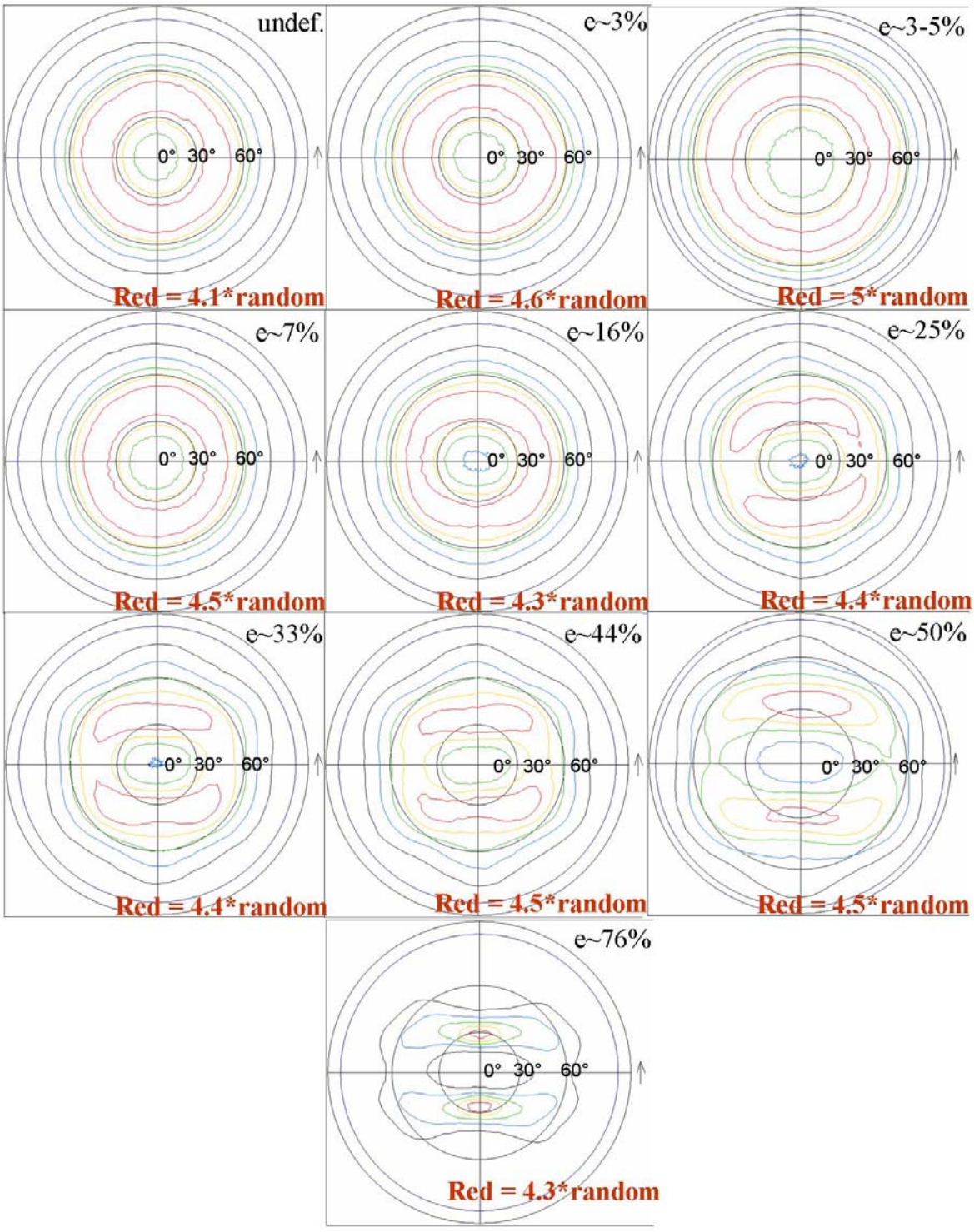

Figure 26. 111 pole figures of undeformed and deformed NC Ni

3.2 UNDEFORMED NC NICKEL

The morphology of the microstructure of the NC Ni has been investigated by transmission electron microscopy.

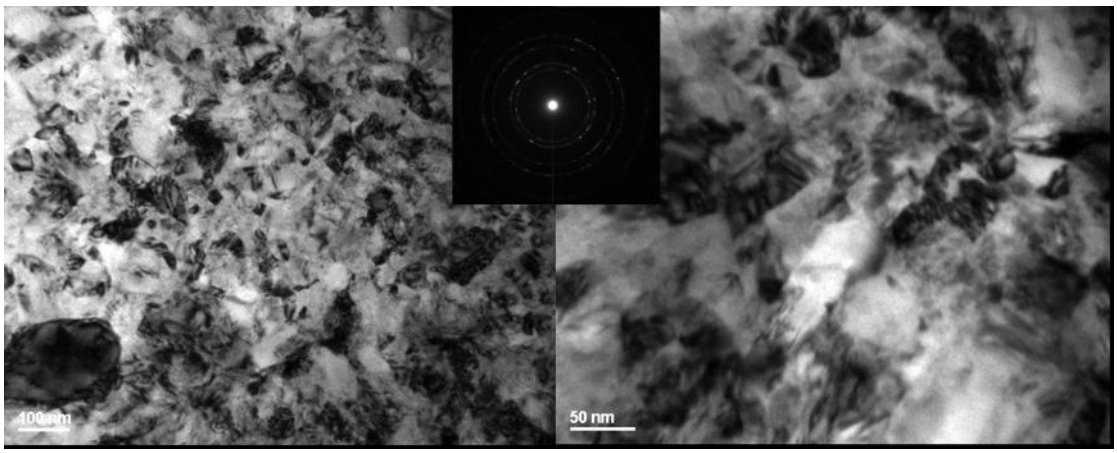

Figure 27. Plan view TEM bright field images and corresponding diffraction pattern of the undeformed sample

Figure 27 shows plan view bright field images and an inset corresponding diffraction pattern. The bright field images show small features but also larger features of uniform contrast. As previously discussed in the introduction, bright field imaging is not very sensitive to orientational changes. Regions of uniform contrast might contain several grains of different orientation. Hence, the dark field imaging technique, which is much more sensitive to orientation changes, was used to determine the grain sizes to evaluate the average grain size in the grain populations.

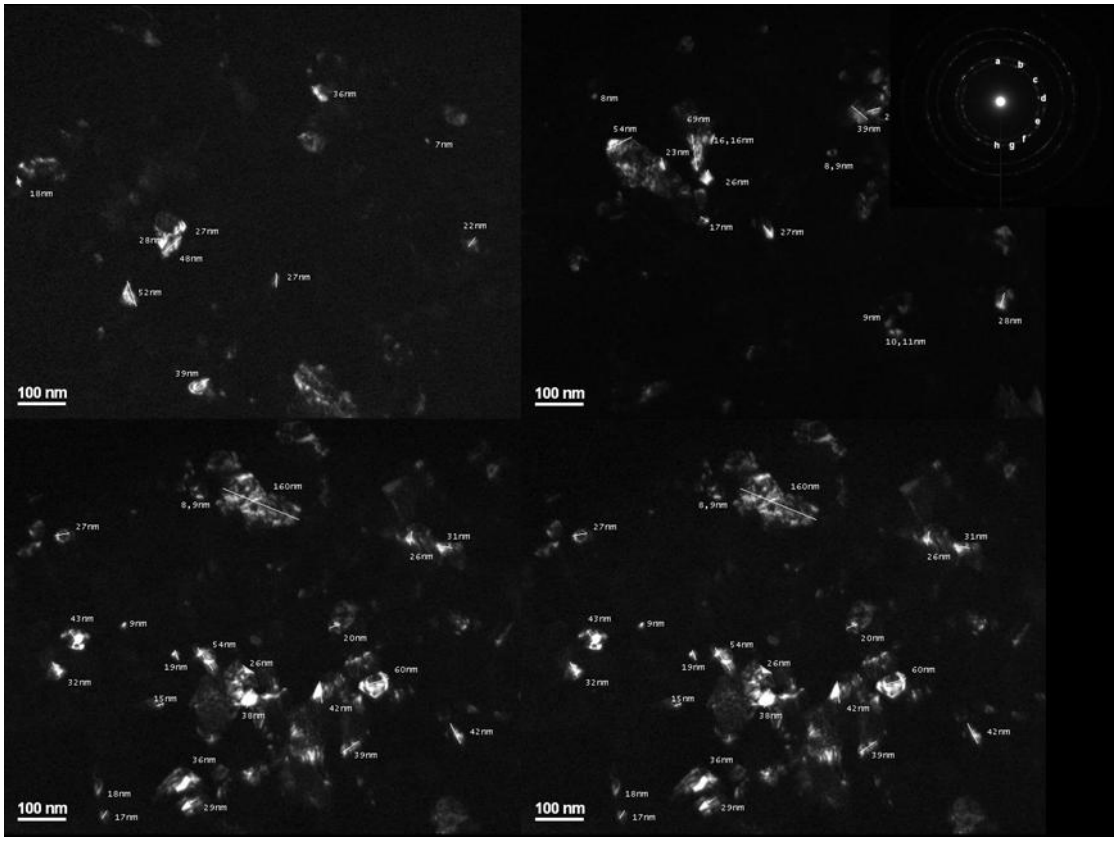

Figure 28. Plan view dark field images and corresponding diffraction (the numbers indicate where dark field images were taken from) pattern of undeformed NC Ni

Figure 28 shows an example of type of plan view dark field TEM micrographs used for this purpose. Most features that appear bright correspond to grains or at least parts of grains that are in a diffracting condition. Most of these features, interpreted here as grains seem to be around 40nm in size and fairly equiaxed in morphology. For all samples the grain sizes were measured from plan view images like the ones depicted in Figure 28. Hence, while systematic errors intrinsic to this choice of grain size measurement method exist, they are the same for each of the measurements for each of the deformation processing conditions. Hence, these data sets enable access to the evolution of the grain sizes and specifically an average grain size taking here as in most of the literature and other studies as an experimental microstructural observable or metric representative of the material. Grain size measurements are affected with error. Thiele et al.

showed that using the various measuring techniques to determine the grain size of the same sample can yield results that are an order of magnitude different [27]. Determining the grain size via dark field imaging is also associated with uncertainties. The brightness in these images can be enhanced making areas that are maybe close to Bragg condition but do not quite fulfill it appear that would have been dark otherwise. These areas might belong to the same grain and may be only misoriented by 1° due to dislocation content within the grain. They might also belong to a grain with a different orientation. As the size of the aperture always includes more than one diffraction spot for the formation of the dark field images used here, areas that appear bright might contain multiple grains that are misoriented by the angular spread or size of the objective lens aperture. Moreover, dark field images were also taken from not only one diffraction ring but from the 111 and the 200 ring. Neighboring grains that have 111 and 200 orientations could appear as one. Another major downside is that all the presented TEM data in this work are plan view images. In order to determine grain sizes in three dimensions additional side view images are necessary, as an area projection doesn't allow definitive conclusion on the dimension of the grains through thickness. Some grains also might have inclined boundaries, which might make their actual size hard to determine. Cross sectional TEM images are required. Plans for future work include investigations of cross sectional TEM samples as well. Being aware of these issues all grain size measurements were carried out in a consistent way for all the different stages of deformation in the hope that the systematic error can be taken to be the same for all measurements. The focus of this study is not the determination of absolute grain sizes but rather to monitor the change of the grain size in the population of grains as function of cold rolling deformation strain. The detailed results of the grain size measurements will be discussed in the section on grain size trends. The average grain size was determined to be D_{ave} = 37±6nm,

the median D_m = 26±6nm. The error is not associated with the standard deviation of the distribution.

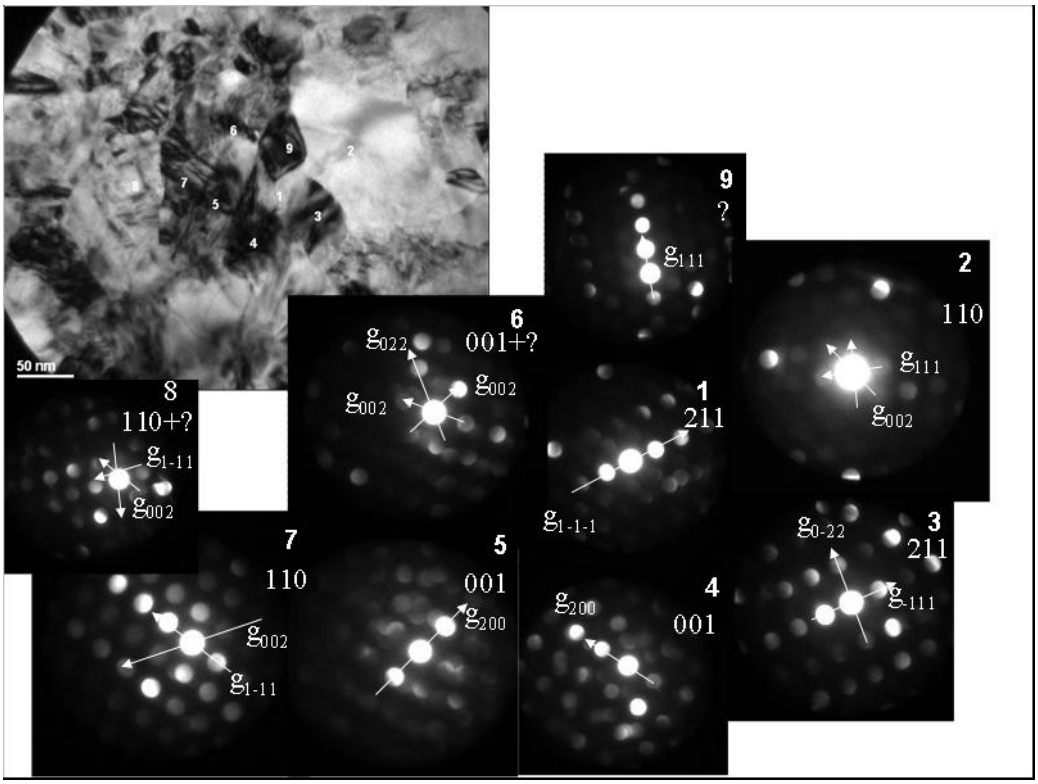

Figure 29. Local orientation change analysis of an area of the undeformed NC Ni: Plan view bright field TEM of several grains with nano diffraction patterns taken from the labeled grains.

The error used here is associated with the measurement itself. A number of grains were measured several times and the statistical error of the measurements was determined. This is the reported error. No distribution function was fitted to any of the results. Some results have rather irregular shape proving curve fitting to be rather difficult. The average value of grain size reported here is the geometric average. This study is primarily trying to monitor and to interpret the changes in grain size population. Figure 29 shows a bright field region of the undeformed sample with multiple grains discernible. “Nano-diffraction patterns” with an electron beam probe size at the sample of about 20nm in diameter were taken from the indicated labeled grains in order to

determine local differences in crystallographic orientation. Some regions show multiple diffraction patterns. In that case more than one grain is sampled. The probe size could have been larger than the measured grain, multiple grains through thickness could have been present or the beam was focused onto a boundary region rather than the grain interior. The indicated zone axis directions in the diffraction patterns do not represent actual grain orientations. They rather refer to low index zone axis that the grain orientation seems to be closest to. Exact determination of orientations proves rather difficult from this type of diffraction pattern. Some of the diffraction maxima could belong to multiple zone axes. For example the 111 diffraction is contained in a 220 and the 211 zone axis orientations. Therefore if only 111 reflections are visible the grain could be either close to a 111 or a 211 zone axis. At least two different diffraction maxima have to be present to index an experimental pattern. However, some of the present diffraction spots prove also difficult to index as they might stem from higher order Laue zones. If strains are present in the microstructure, the angles between directions in reciprocal space might be distorted, length of diffraction vectors altered. Thus, there is an uncertainty associated with the indexing of these singular nano-beam diffraction patterns. Tilting the sample and with certainty obtaining additional diffraction patterns from the same grain is essentially impossible on a regular basis due to the nanocrystalline microstructures tendency for self-similarity in the TEM images. Hence, some patterns could not be indexed. As the only purpose of this set of diffraction experiment was the determination of whether neighboring grains are of similar or very different orientation, exact indexing is not required for such qualitative conclusions. Dark field imaging was added as a second technique to identify separate grains. The outlines seen in the dark field were matched with regions in the bright field.

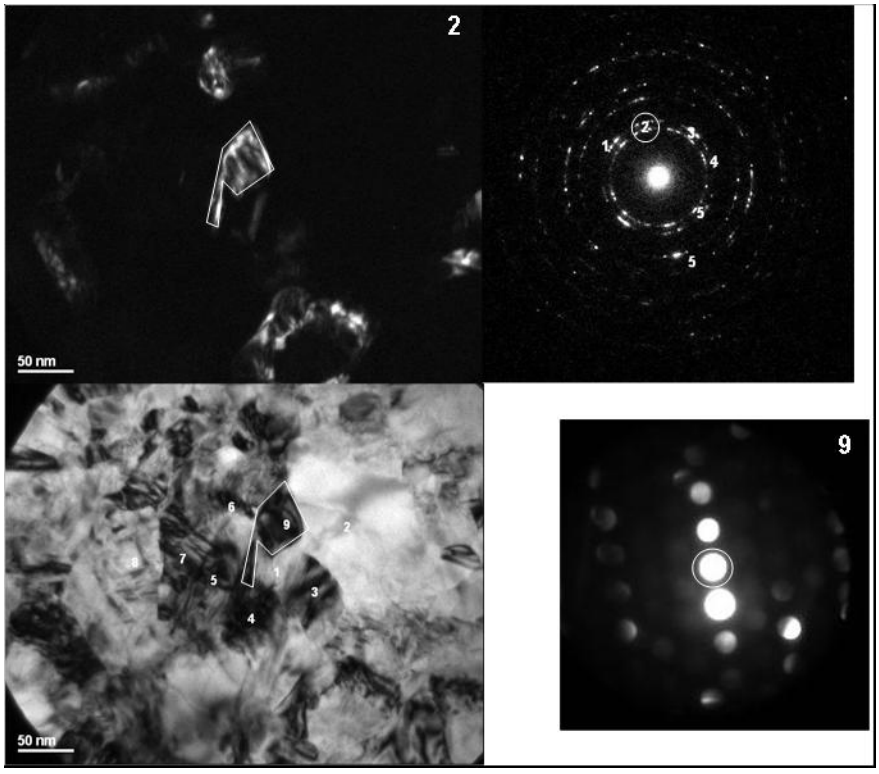

Figure 30. Dark field image (upper left) taken with the diffraction spot shown in the diffraction pattern (upper right); the bright grain identified and outlined in the upper left dark field image is marked in the corresponding bright field image (lower left); the nano-diffraction (lower right) pattern of the region identified by the dark field imaging (upper left an right) is shown and corresponds to a 111 systematic row being excited, which is consistent with the spot used for dark field imaging indicated in the upper right panel

For consistency in identifying grains, the nano-diffraction pattern or patterns of this region were compared with the diffraction spots used for dark field imaging and the corresponding images. The grain orientation determined from the nano-diffraction pattern was compared with those of the neighboring grains. Figure 30 shows an example. In the following sections only one example (sometimes none) of a number of dark field images analyzed in the described way will be shown at a time, unless certain interesting features require the presentation of additional images to support a finding. Combining the results from nano-diffraction pattern analysis along with dark field imaging the grain outlines were determined (e.g. Figure 31). Neighboring grains with similar orientations were also identified. For neighboring grains with similar orientations the same color has been used in the approximate outlines.

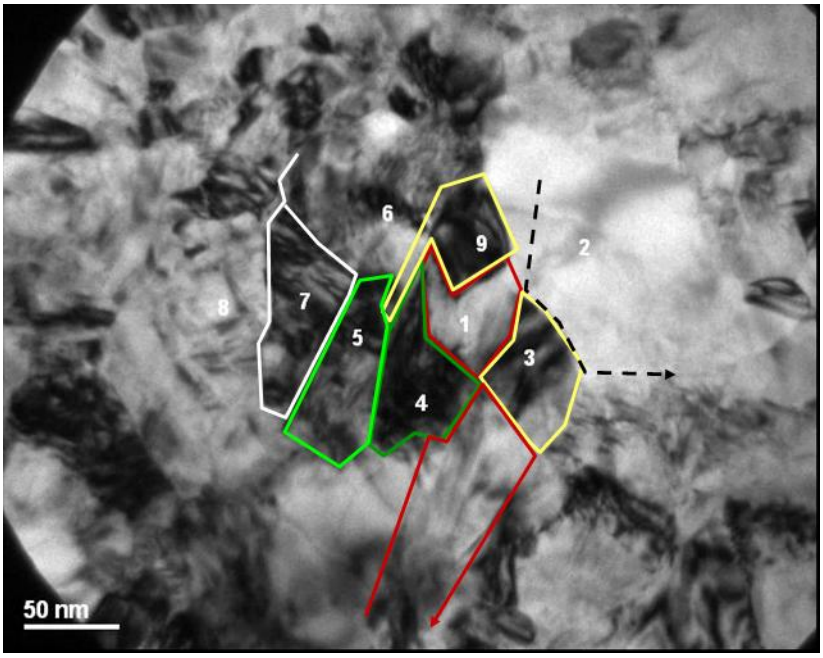

Figure 31. Bright field image with grain outlines. Neighboring grains with same or similar colors indicate similar orientation

Hence, aside from approximate grain boundary locations separating the grains also a qualitative measure of the local grain orientation relationships are indicated. The important finding from the qualitative analysis of this region of the undeformed NC Ni is that most of the measured grains are still separated by high angle grain boundaries (HAGBs). The size of the grains seems to be in the order of 50nm or larger. The grains seem to be fairly equiaxed. The nano-diffraction pattern analysis shows that a considerable fraction of grains is close to a cube orientation. This observation is confirmed by the diffraction pattern in the upper right in figure 30 which is statistically more relevant. This observation is consistent with the XRD and XRD texture results described in the previous section. In order to render quantitative statements on local orientation distribution of the grains in the NC Ni a larger number of grains and different locations in the samples would need to be analyzed to provide representative and statistically relevant data.

Given the difficulty in extracting with confidence exact grain orientations from nano-bema diffraction patterns, which have to be used to identify individual grain orientations, and the correspondence between dark field and bright field images this has not been possible here. However, the analyses performed here, allows qualitative comparison of the undeformed state of the NC Ni with similar results for the deformed samples shown later.

3.3 NC NICKEL 7% DEFORMED

Figure 32 shows a bright field image, a selected area diffraction pattern and two example dark field images of the 7% deformed sample, which were used for grain size determination. Both the bright field as well as the dark field image show mostly equiaxed morphology grains. The dark field images show still very small features on the order of 10nm but also a few features that are larger than 100nm.

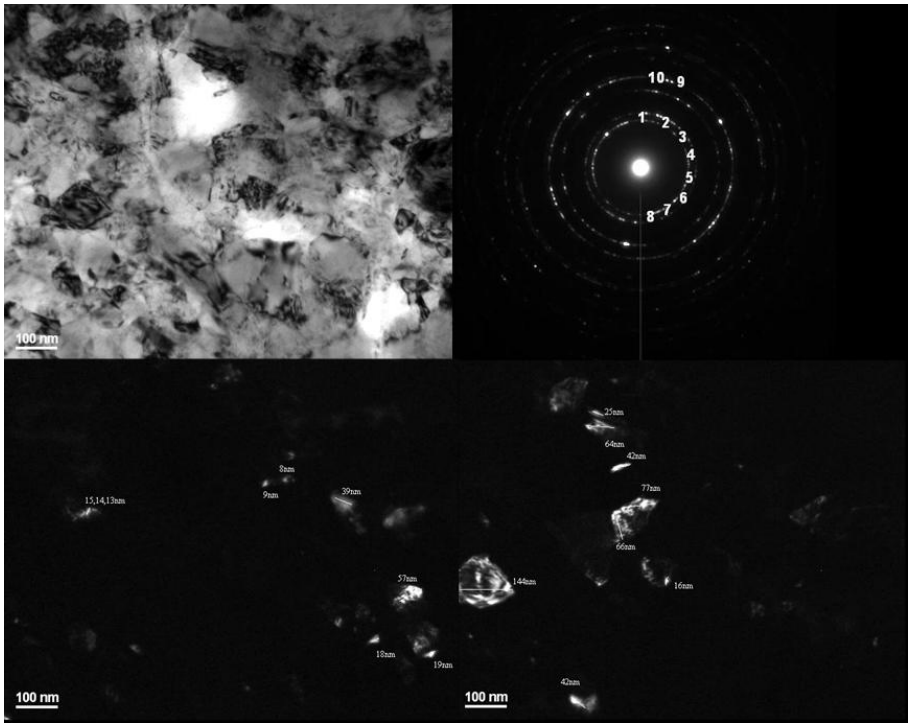

Figure 32. Plan view bright field (upper left), corresponding diffraction pattern (upper right), two dark field images (lower left and right)

The measurement of grain size and grain size population determination has been carried out as described for the undeformed NC Ni. The results discussed in much greater detail in a separate section yielded an average grain size of D_{ave} = 42±6nm and a median D_m = 33±6nm. Within the error the grain size did not differ from that of the undeformed NC Ni of D_{ave} = 37±6nm, the median D_m = 26±6nm.

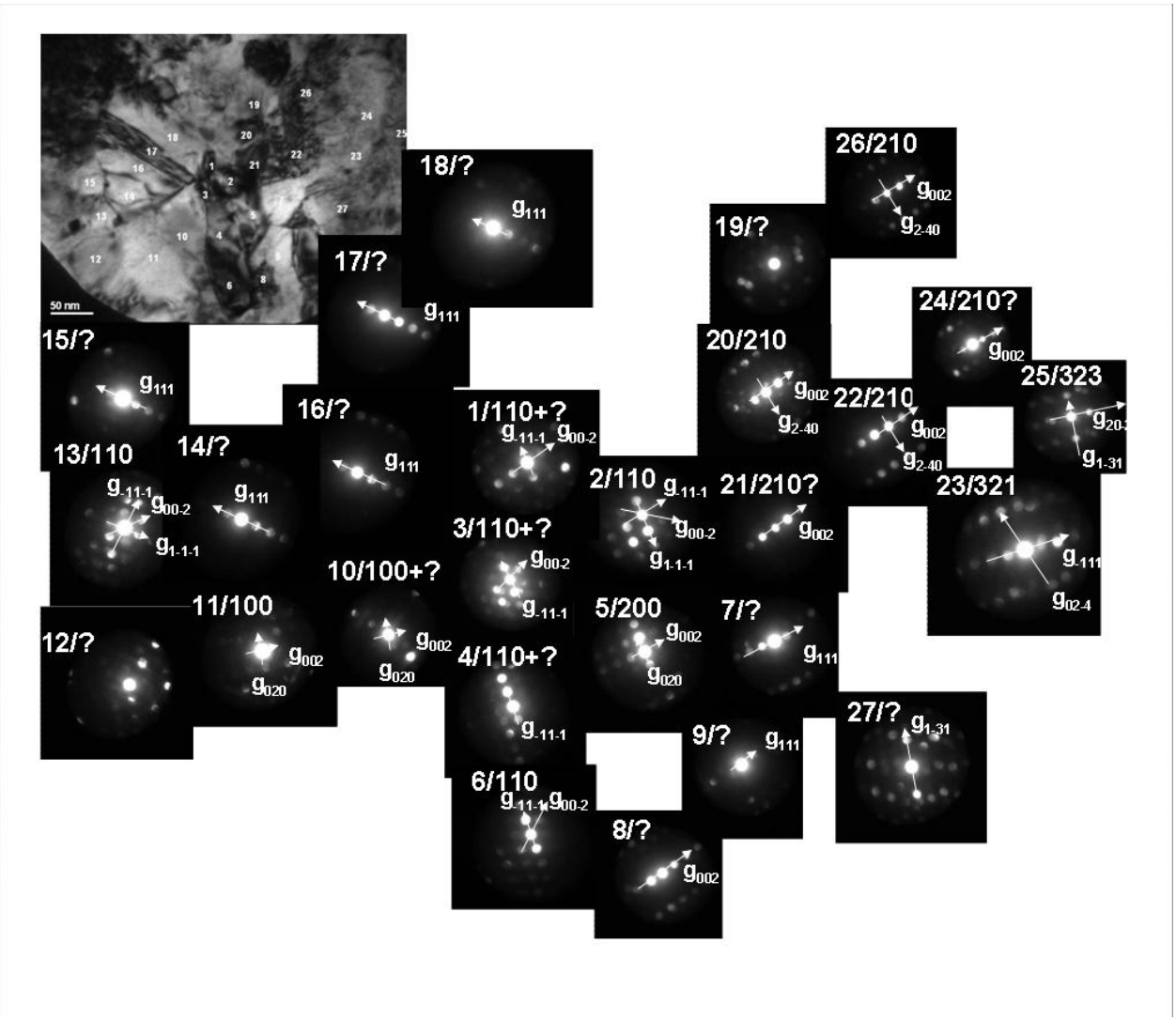

Figure 33. Local orientation distribution measurement: Bright field image including nano-diffraction patterns form the indicated area

Figure 33 shows an example analysis of local orientation distribution of grains, investigated as described in the previous section.

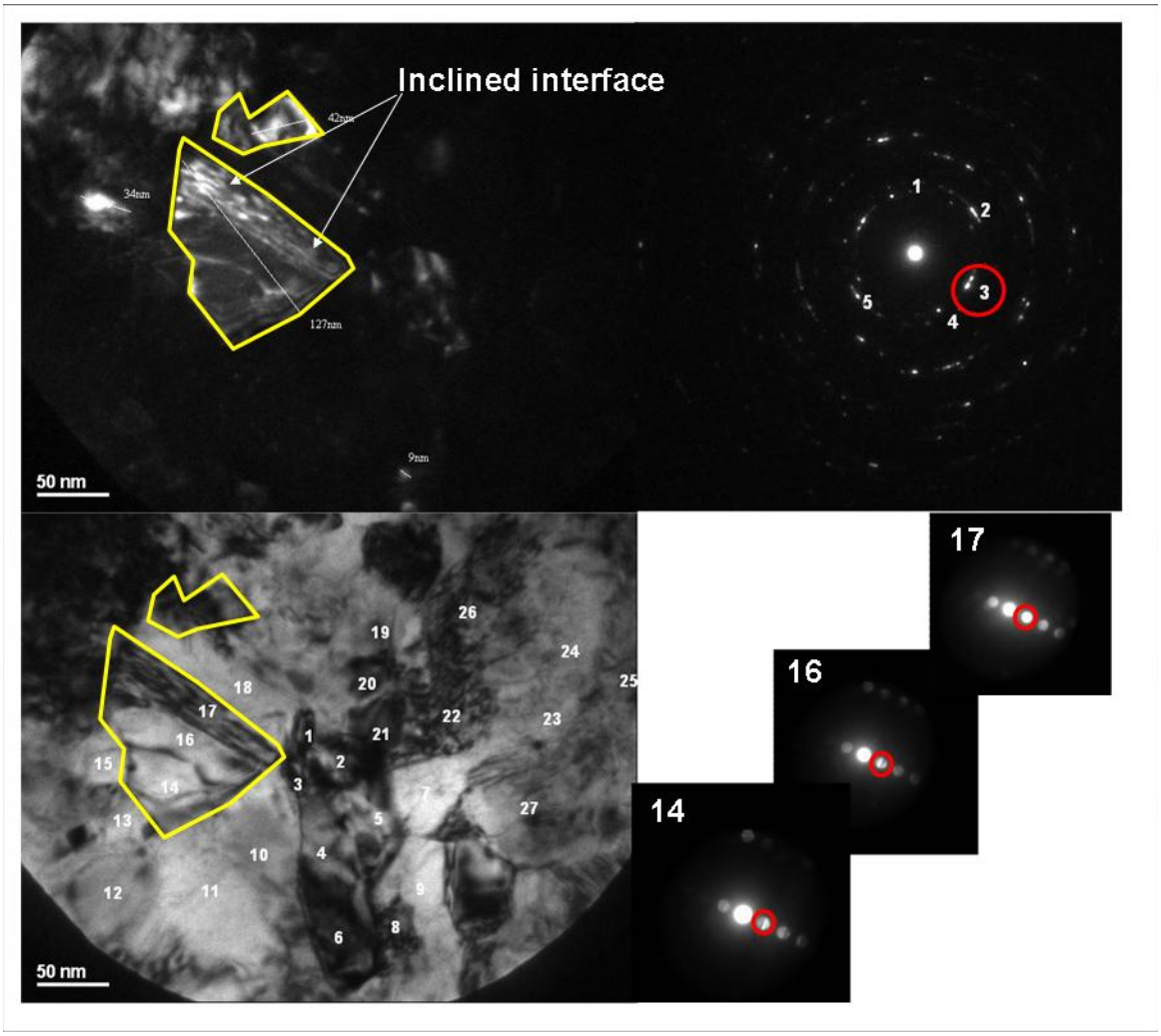

Figure 34. Dark field image (upper left) taken with the indicated diffraction vector (diffraction pattern on the upper right); bright field image (lower left) with matched region and nano-diffraction patterns of the locations labeled in the bright field image.

Figure 34 shows a dark field image taken in addition to the nano-diffraction pattern analysis as described in the previous section. Inclined boundaries can be seen as indicated in Figure 34. The nano-diffraction patterns show that the regions 14, 16 and 17 have essentially the same orientation.

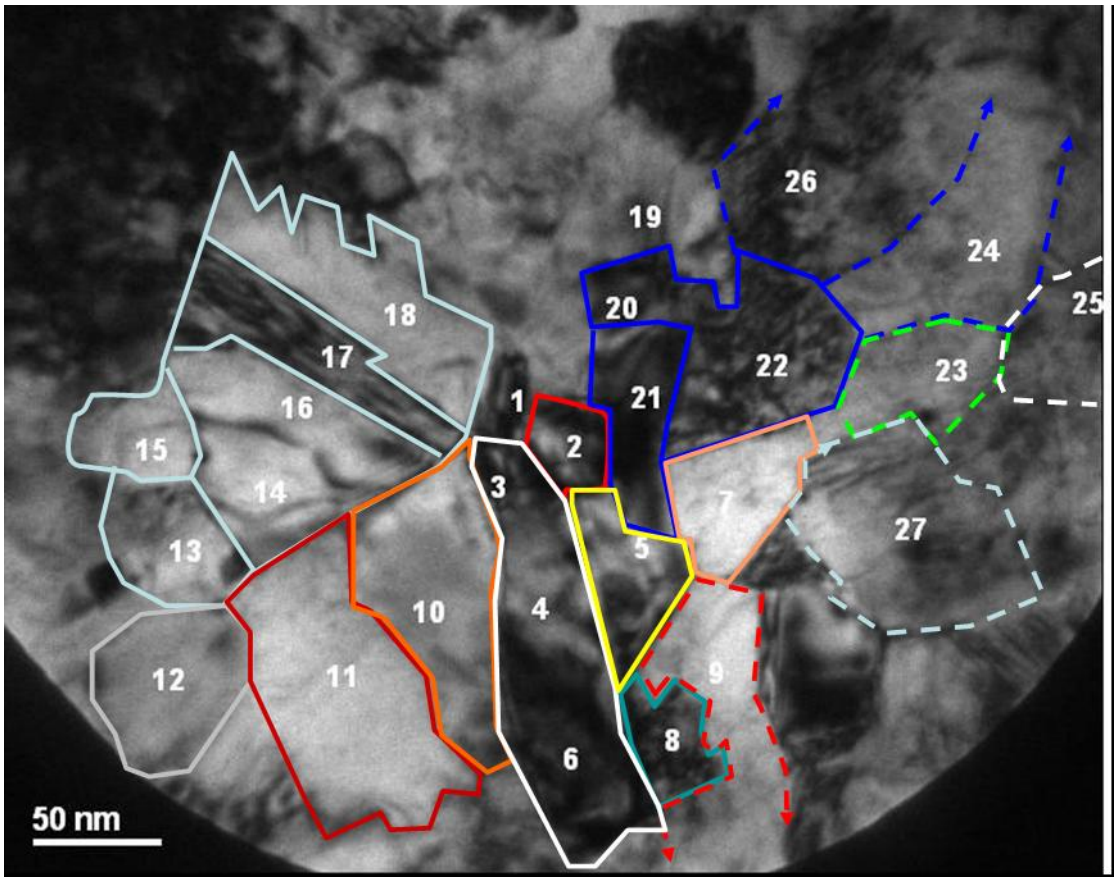

Figure 35. Combined nano-diffraction and dark field imaging results: Bright field image with outlined grains

Figure 35 shows the combined result of the dark field and nano-diffraction pattern analysis. Small grains are still observable. However there are also clusters of grains observable that are of similar or close orientation (neighboring grains outlined with the same color, e.g. grains 13 – 18 and 20-22). The surrounding grains outlined in differing colors have very different orientations. There are still grains observable that are in orientations near to a cube orientation. However, a considerable fraction of grains show different orientation after the small amount of reduction in thickness of 7%.

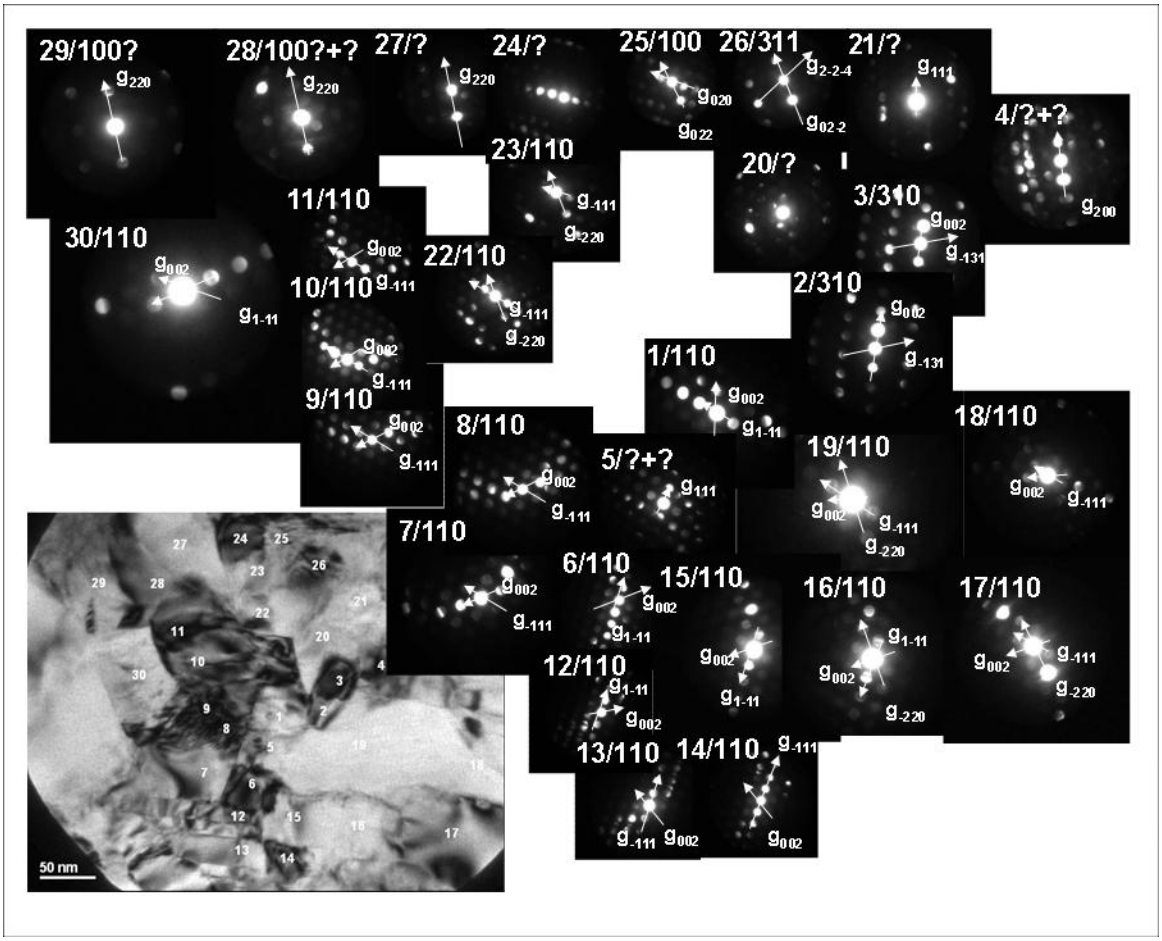

Figure 36. Local orientation distribution measurement: Bright field image including nano-diffraction patterns form the indicated area

Figure 36 and Figure 37 show another analysis of local orientation changes. Similar to previous analyses, dark field images (not shown here) were taken to aide the nano-diffraction pattern analysis. The diffraction pattern of this area (Figure 34) shows an elevated amount of grains that are close in orientation to a 110 type zone axis. This is consistent with the findings of the nano-diffraction pattern analysis. The bright field image in Figure 34 also indicates that larger areas are of very similar orientation (neighboring grains with the same color outlines). However, it also shows that areas of similar contrast can contain smaller units that are close in orientation but still different, confirming the invalidity of the use of bright field imaging for grain

size determination. Most grains seem fairly equiaxed in morphology. Some of the grains that cluster together and have similar orientation, however, assume an elongated shape (grains at bottom right in Figure 37).

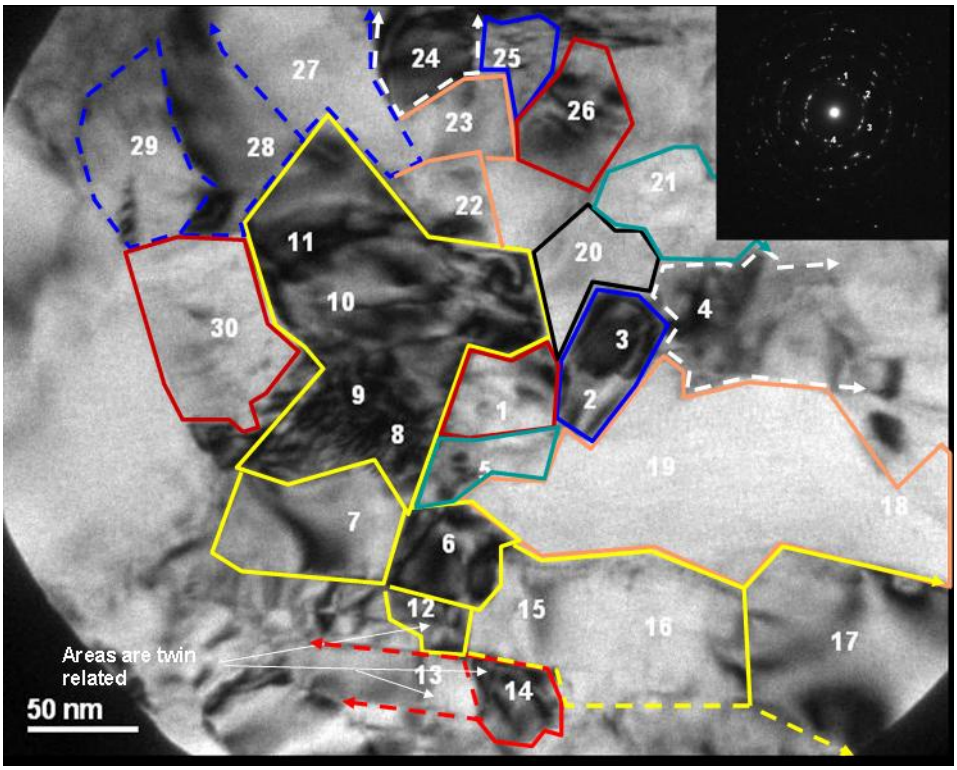

Figure 37. Combined nano-diffraction and dark field imaging results: Bright field image with outlined grains

Summing up, the grain size analysis of the 7% deformed sample yields very similar results as for the undeformed sample (discussed in greater detail in a later section). Most grains still seem to be fairly equiaxed and the morphology does not change dramatically after 7% reduction in thickness. However, local orientation analysis shows that unlike in the undeformed sample, after 7% deformation areas can be seen where grains seem to come closer in orientation seem to cluster. No clear evidence of massive dislocation activity has been observed, however, it cannot be excluded, since for the grains of average grain size below 40nm it is still postulated

that only individual gliding dislocations are supported by a given grain and that the glide dislocations are deposited or even absorbed into the grain boundaries. Hence, dislocation content from interacting glide dislocations being deposited into the grain interiors is not expected for the 7% cold rolling thickness reduced NC Ni.

3.4 NC NICKEL 16% DEFORMED

Figure 38 shows a plan view bright field image, a diffraction pattern and two example dark field images used for grain size analysis.

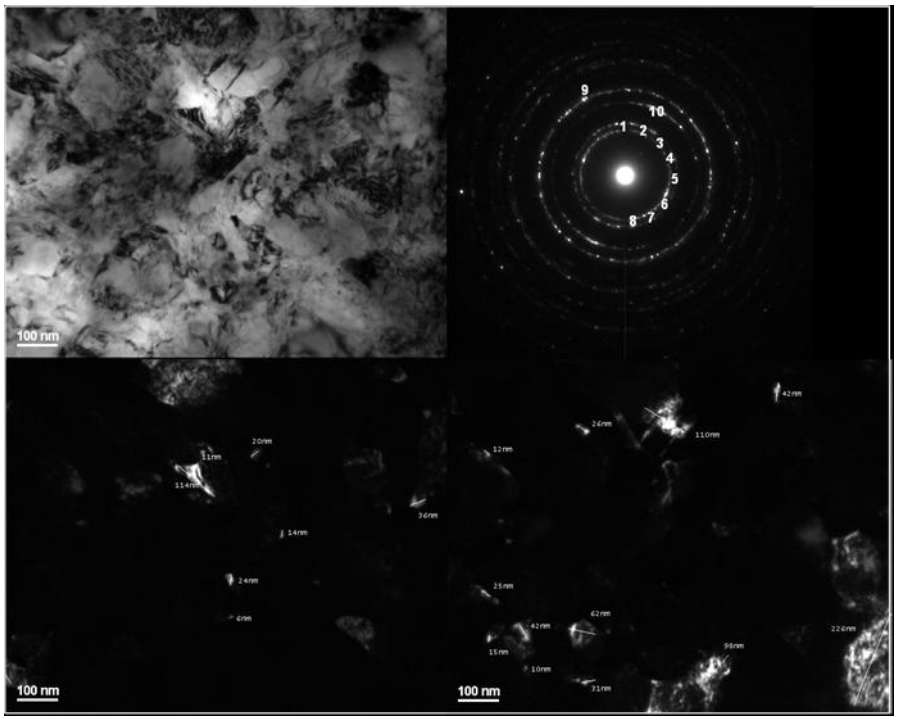

Figure 38. Plan view bright field (upper left), corresponding diffraction pattern (upper right) and two plan view example dark field images (lower left and right)

The bright field shows large areas of uniform contrast. Dark field image analysis determines an average grain diameter of D_{ave} = 63±8nm and a median grain diameter of D_m = 39±6nm. The increase in grain size is significant as the changes exceed the error margins. An example of a local orientation analysis is depicted in Figure 39.

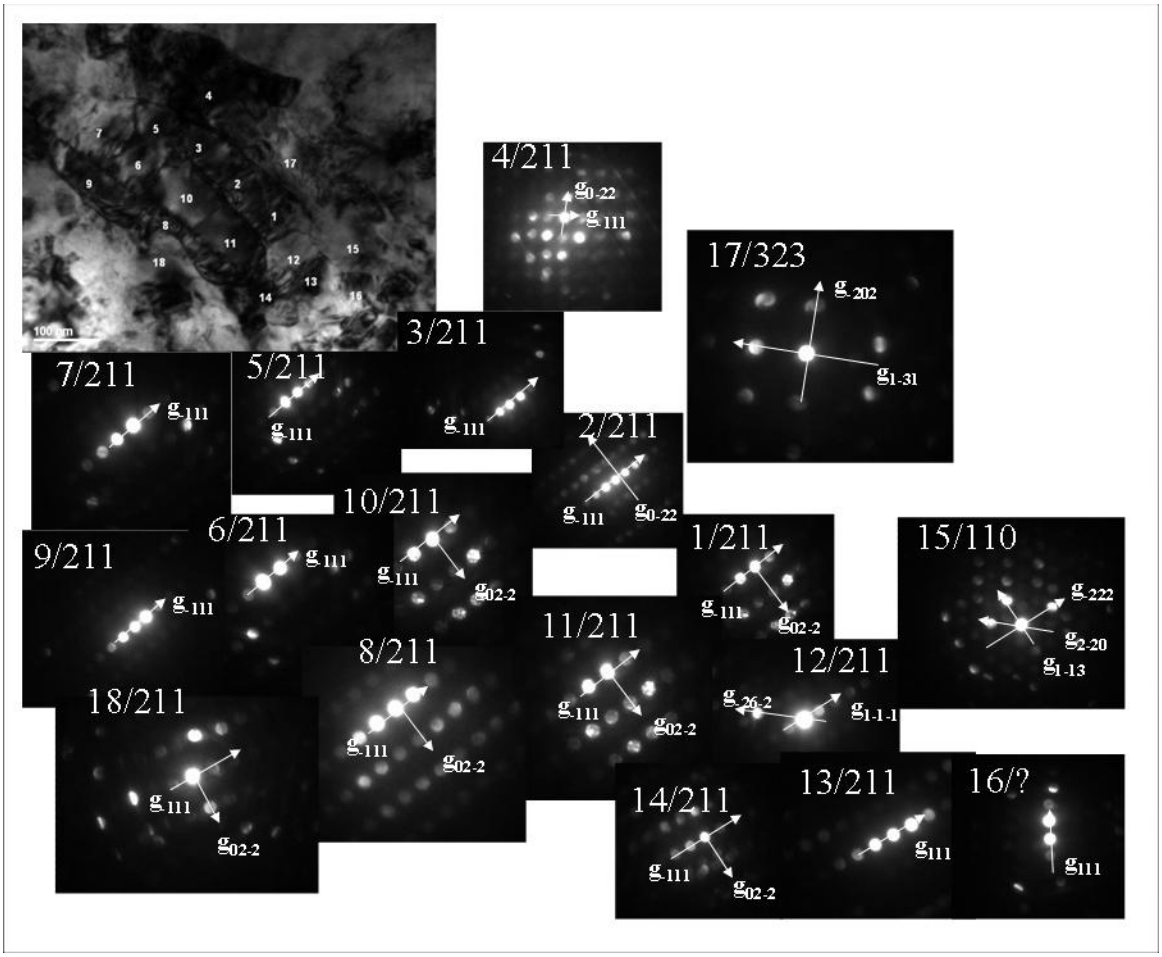

Figure 39. Local orientation distribution measurement: Bright field image including nano-diffraction patterns form the indicated area

Most orientations of the analyzed areas were close to a <112> orientation. Figure 40 shows an example of a dark field image analysis as described in the previous sections. The bright areas observed in the dark field correspond to a number of different regions analyzed by nano-

diffraction. The nano-diffraction patterns show that large areas analyzed are close in orientation but still slightly misoriented. This area contains more grains that are separated by low angle grain boundaries (which would be expected for LAGB´s but is not necessarily sufficient to identify these GB's as LAGB´s). Most grains neighboring these grain clusters of similar orientation are of rather different orientation, i.e. separated from them by larger angles of misorientation, which would not be inconsistent with the expectation for high angle GB´s (HAGB´s). The selected area diffraction pattern in figure 40 shows that an increased fraction of the grains is close to a <211> orientation, consistent with the nano-diffraction pattern analysis. Figure 38 shows the combined result of the nano-diffraction pattern and dark field imaging analysis and corresponding bright field image with outlined grains. Dashed lines in Figure 38 indicate suggested boundaries with position that cannot clearly be identified.

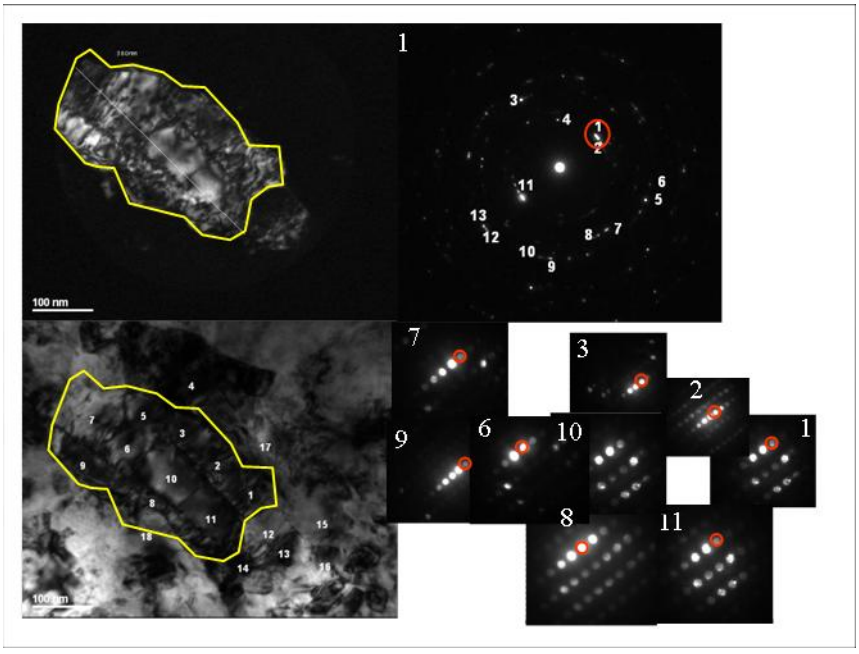

Figure 40. Dark field image (upper left), diffraction pattern (upper right), bright field image(lower left) and corresponding nano-diffraction patterns

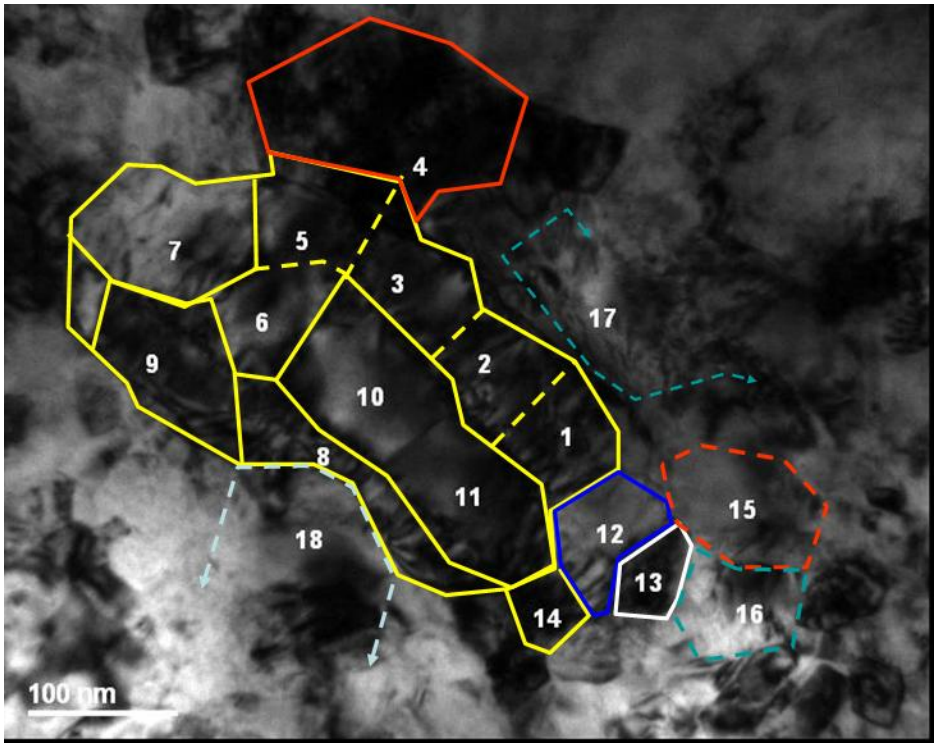

Figure 41. Combined nano-diffraction and dark field imaging results: Bright field image with outlined grains

After deformation by 16% of cold rolling thickness reduction a measurable change in grain size is observable. The trend of grains in neighboring groups coming closer in orientation and to form grain clusters of similar orientation already first indicated after 7% deformation seems to continue and is more enhanced. In the regions analyzed for local misorientation (Figure 39 and Figure 41) most orientations are consistent with the small orientation differences expected for LAGB´s.

3.5 NC NICKEL 34% DEFORMED

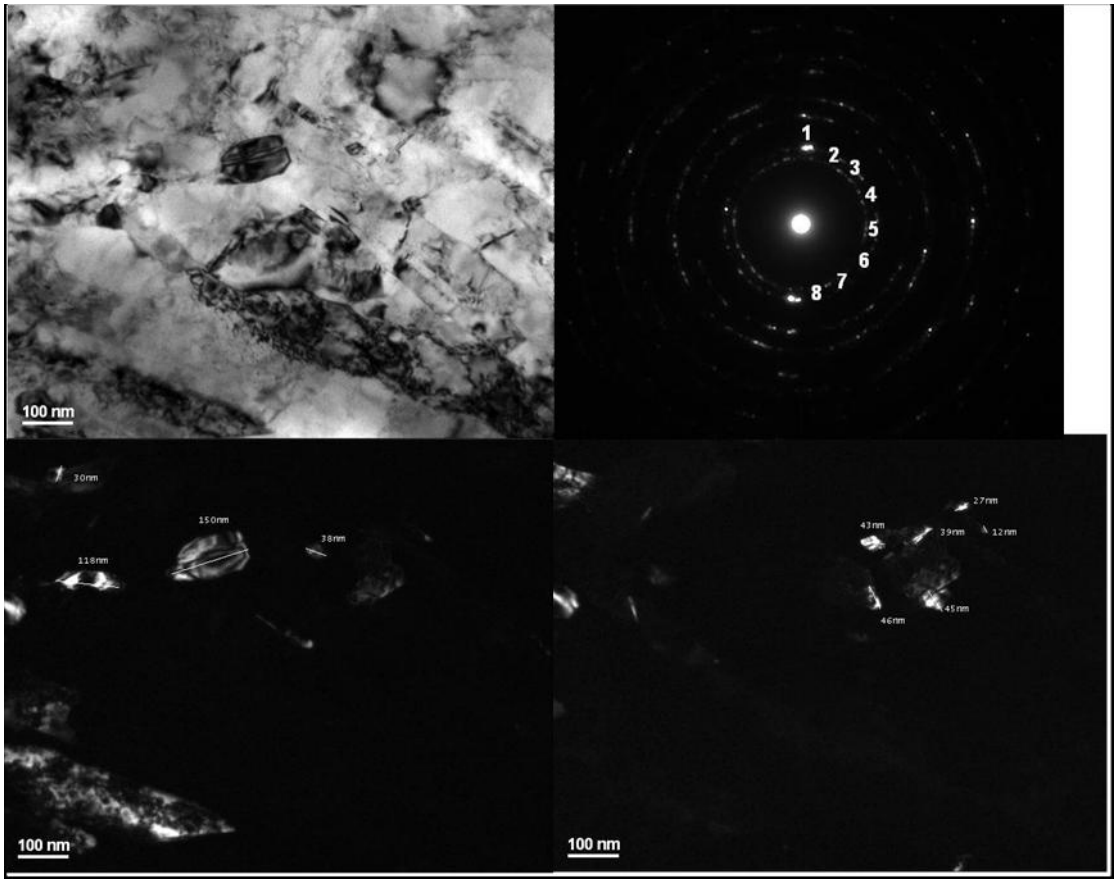

Figure 42. Plan view bright field image (upper left) corresponding diffraction pattern (upper right) and two plan view dark field images (lower left and right)

The bright field image displayed in Figure 42shows elongated areas of uniform contrast. The dark field image in the lower left panel of Figure 42 confirms the presence of elongated grains aside from equiaxed grains (Figure 42: lower left corner in the bottom left dark field image). Grain size analysis results in an average grain size of D_{ave} = 78±8nm and a median grain size of D_m = 46±8nm. Relative to the 16% reduction in thickness NC Ni this change in grain sizes is insignificant, while they clearly indicate a significant increase in grain size over the undeformed and the 7% thickness reduction cold rolled states.

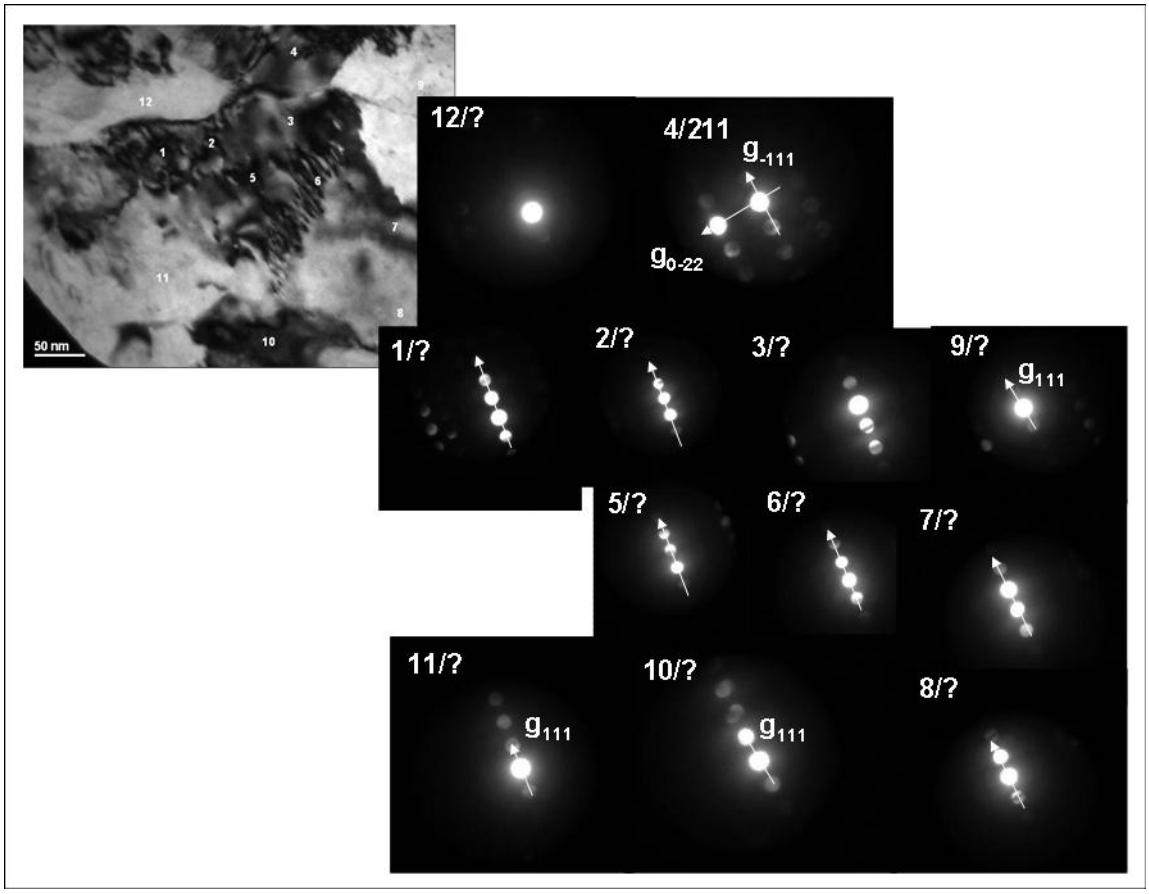

Figure 43. Local orientation distribution measurement: Bright field image including nano-diffraction patterns form the indicated area

In the area displayed in the bright field image of Figure 43 large fractions of the field of view appear to exhibit very similar orientations relative to the imaging electron beam. Dark field imaging confirms the results from the nano-diffraction pattern analysis. The nano-diffraction patterns indicate a small misorientation of largely tilt character about an axis perpendicular to the excited systematic row of diffraction intensities. (If in a diffraction pattern only one row of reflections fulfill Bragg condition it is referred to as an excited systematic row, e.g. here 000, ±111, ±222, ±333 etc, i.e. the 111 systematic row, Figure 43). In figure 44 a nano-diffraction pattern including this approximate axis of tilt character misorientation is displayed.

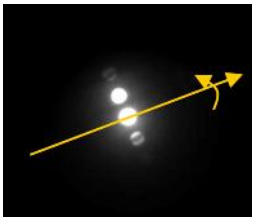

Figure 44. Nano-diffraction pattern including the rotation axis over which regions in the area are misoriented

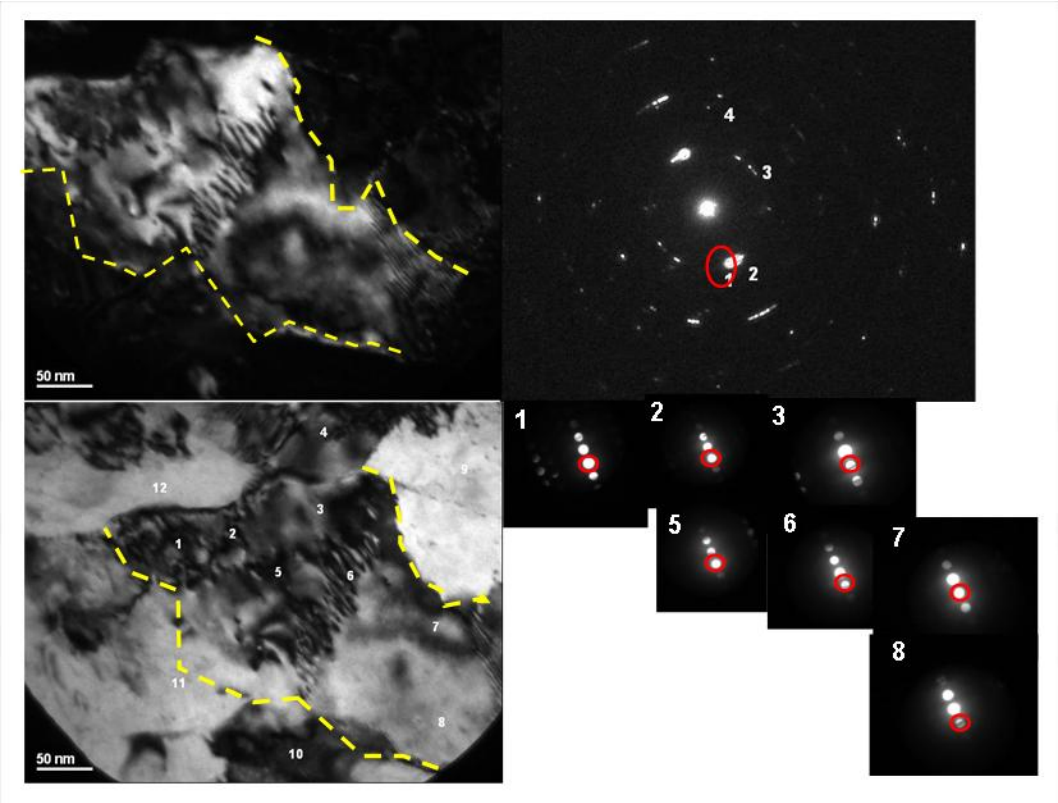

Figure 45. Dark field image (upper left corner), corresponding diffraction pattern (upper right), bright field image (lower left corner) and nano-diffraction patterns of the corresponding area

It should be noted that there might be more than one rotation axis present over which grains are misoriented. Figure 45 shows a dark field image analysis consistent with the nano-diffraction analysis. The combination of results from both the dark field imaging and the nano-diffraction are summarized in the bright field image of Figure 46. The main area of the field of view seems

to belong to one elongated grain. Importantly, misorientation of some of the neighboring grains is also rather small, indicating that an even larger area could be related closely in crystallographic orientation and that some grain coalescence might already have and more is about to occur if suitable driving forces became available.

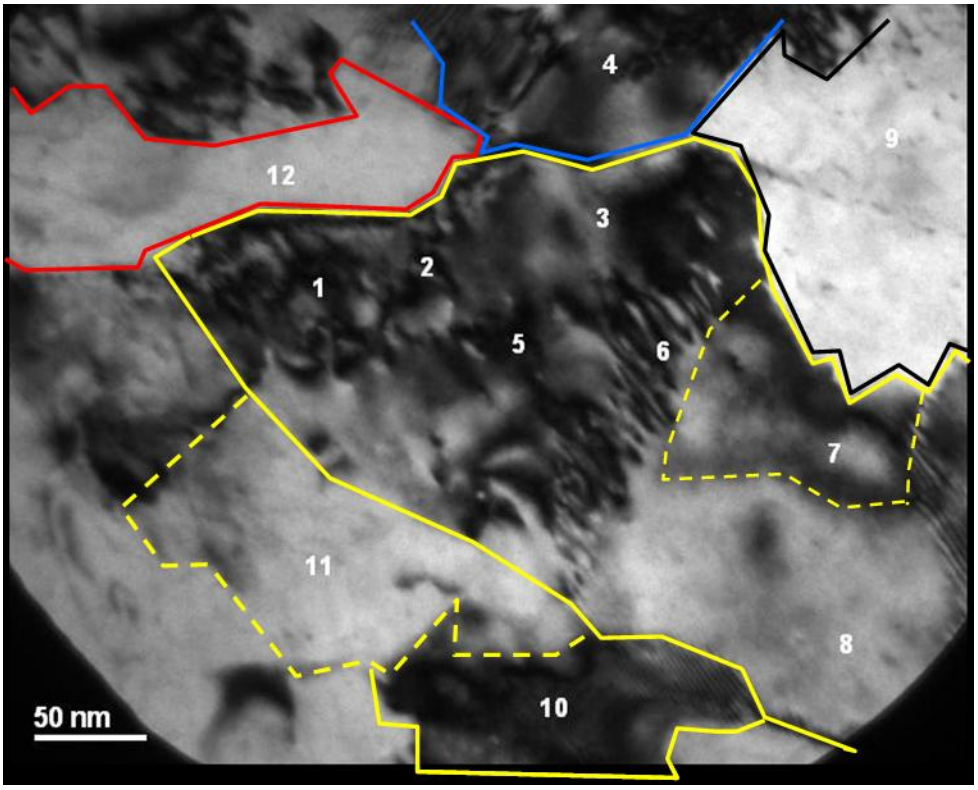

Figure 46. Combined nano-diffraction and dark field imaging results: Bright field image with outlined grains

In Figure 46 also fringe contrast can be seen. These fringes are moiré fringes. Moiré fringes are produced when two crystals overlap, that either differ in lattice parameter or orientation [32].

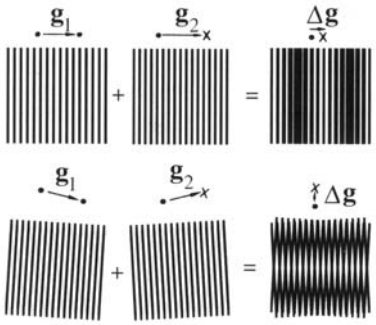

Figure 47. Schematic representation of the origin of moiré fringes.

The fringe spacing can be measured from the image. If in addition the crystallographic orientation of the two overlapping grains is known the misorientation angle can be estimated [32]. The general expression that relates moiré spacing is given

$$D = \frac{d_1 d_2}{\left(d_1^2 + d_2^2 - 2d_1 d_2 \cos\phi\right)^{1/2}} \qquad \text{Equation 7}$$

(D = moiré fringe spacing, d_1,d_2 are lattice spacings, ϕ = misorientation angle). In the case that $d_1 = d_2$, the special case of pure rotational misorientation (rotational moiré fringes) the expression simplifies to

$$D = \frac{d}{\phi} \qquad \text{Equation 8}$$

In case that $\phi = 0$ (parallel moiré) the expression above becomes

$$D = \frac{d_1 d_2}{d_1 - d_2}$$ Equation 9

From the nano-diffraction pattern analysis (Figure 43) it can be deducted that both grains have same type of diffraction vectors excited, i.e. the spacing is the same for the grains (rotated 111 set of planes), that are rotated. Using this routine misorientations were determined. The results can be seen in Figure 48.

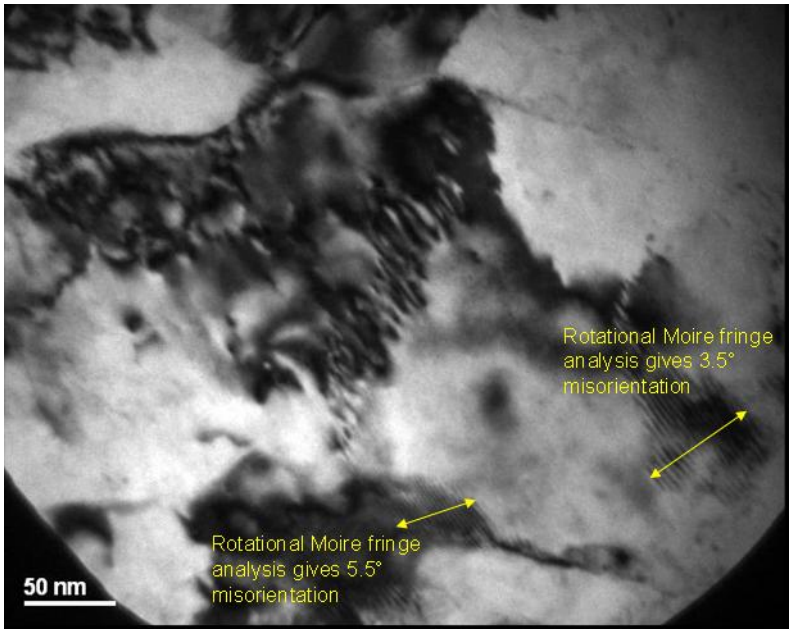

Figure 48. Moiré fringe analysis: Bright field image including misorientation

Figure 49 shows another area that has been analyzed for grain outlines and local orientations

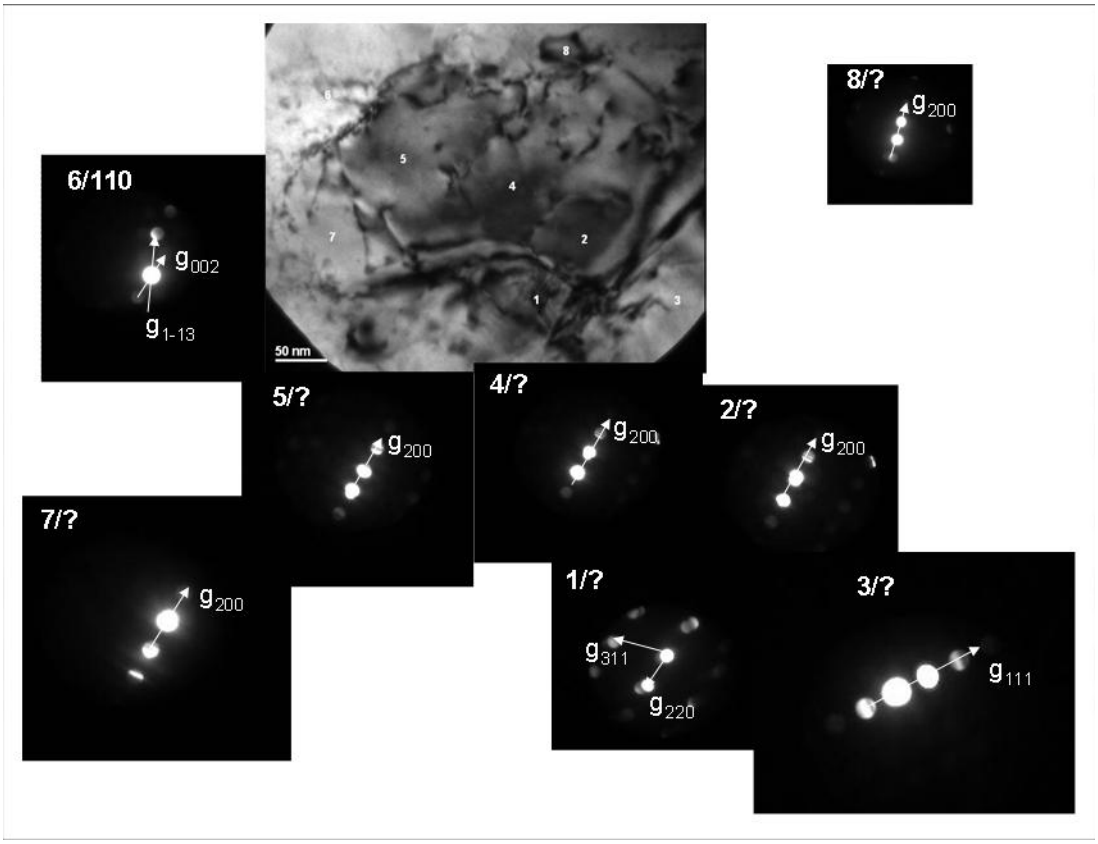

Figure 49. Local orientation distribution measurement: Bright field image including nano-diffraction patterns form the indicated area

Dark field analysis is depicted in Figure 50:

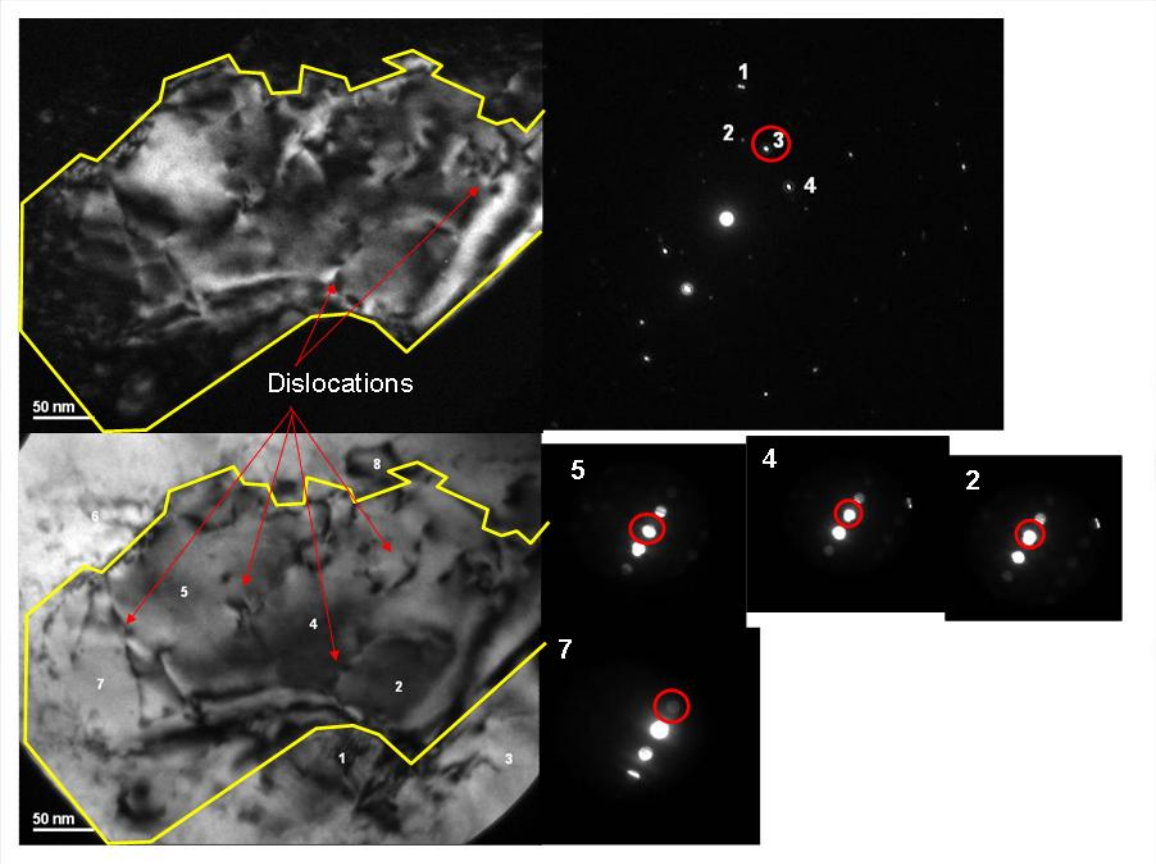

Figure 50. Dark field image (upper left) corresponding diffraction pattern (upper right); bright field image (lower left) and nano-diffraction patterns

The nano-diffraction patterns are very similar to the ones analyzed in the previously analyzed area (Figure 43). They also show an excited systematic row. Similarly, slight misorientations over a tilt axis perpendicular to the excited row as depicted in Figure 41 are observable. Dislocation tangles can be seen in both the dark and the corresponding bright field images of Figure 50. The shape and form of the dislocation tangles indicates dislocation interactions. The dislocation lines are not of equilibrium shape, i.e. straight or smoothly bowed or elliptical in shape. The dislocation lines exhibit sharp changes in direction and apparent pinning points between longer straight segments. This is consistent with the presence of jogs or other possible pinning points, such as precipitates. Here we investigate a single phase Ni crystal and

precipitation is not expected. Hence, it is reasonable to conclude that the pinning points visible along the dislocation lines are jogs. Jogs and the presence of the dislocation interior would be consistent with simultaneous glide activity on multiple slip system in a given grain. As explained in the introduction, from a stress consideration point of view below a certain average grain size only one dislocation can be present in a single grain at a given time. As the starting grain size of this material was such that only one dislocation at a time could be present, the grain containing the evidence for multiple slip system activity (Figure 50) was either larger than the average grain size to start with or it coarsened as a result of the cold rolling deformation.

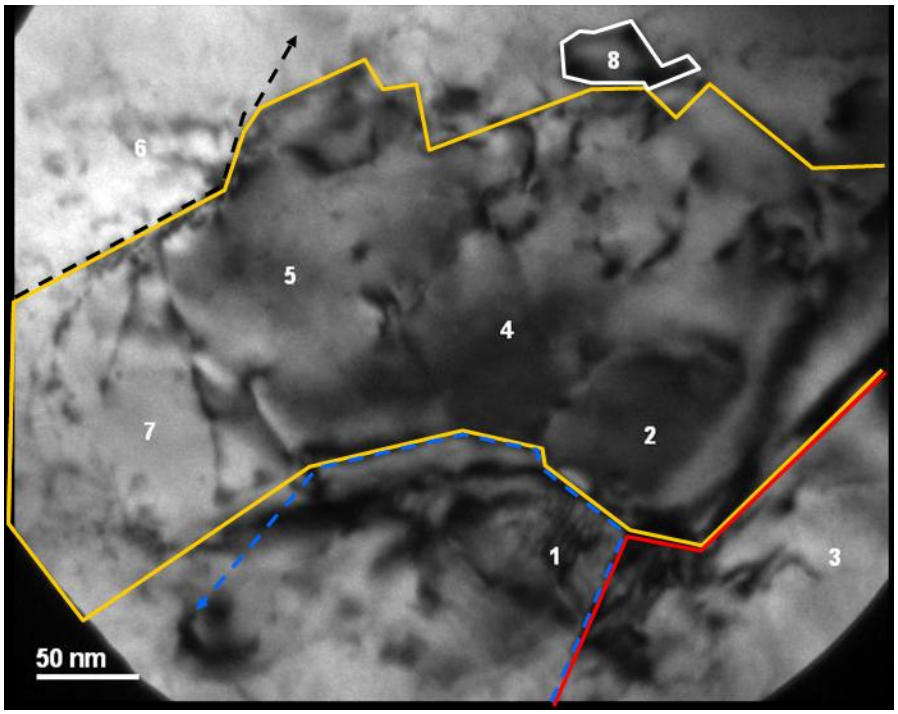

Figure 51. Combined nano-diffraction and dark field imaging results: Bright field image with outlined grains

Figure 51 shows the result of the combined nano-diffraction and dark field analysis. Very similar to the previously analyzed area a very large elongated grain is observable. The previously

analyzed areas showed examples of rather large grains. However, in the microstructure of this deformation state there are also areas present where considerably smaller grains can be seen.

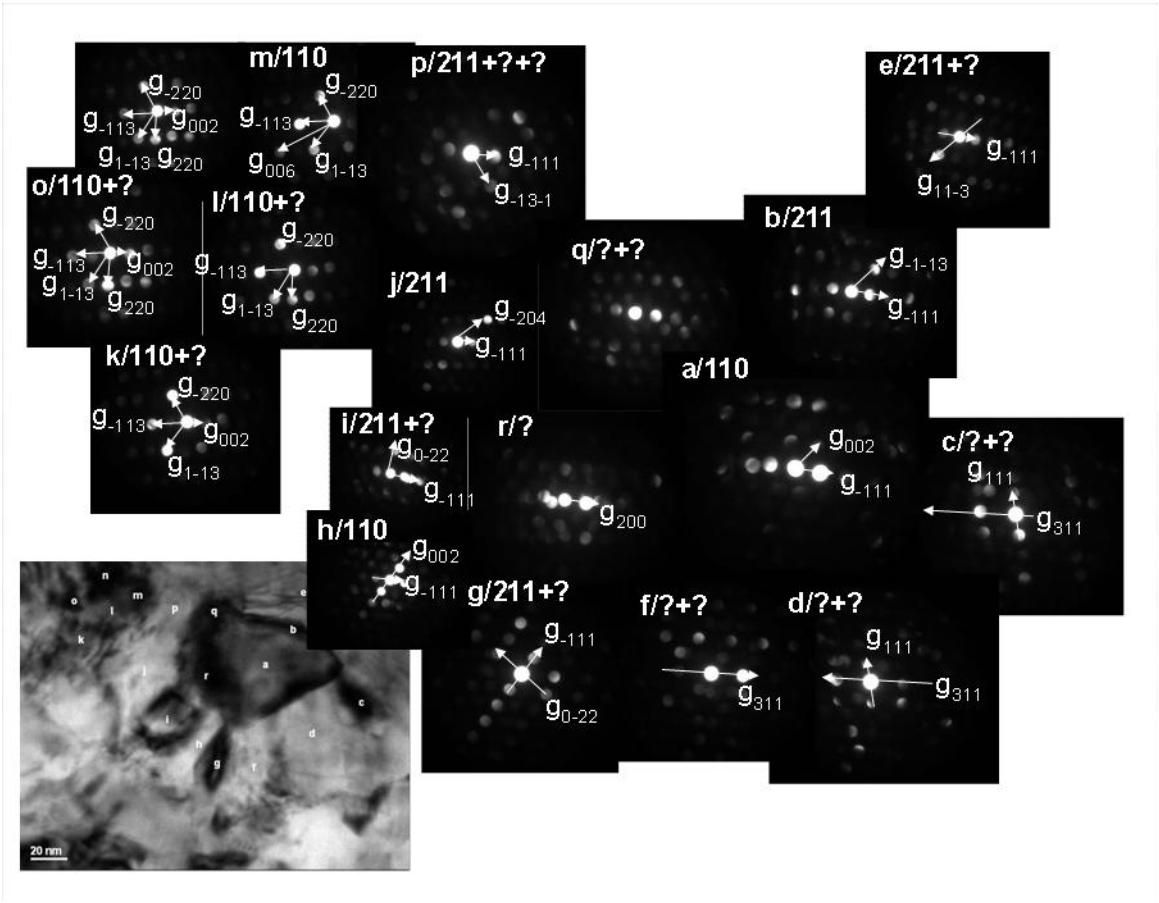

Figure 52. Local orientation distribution measurement: Bright field image including nano-diffraction patterns form the indicated area

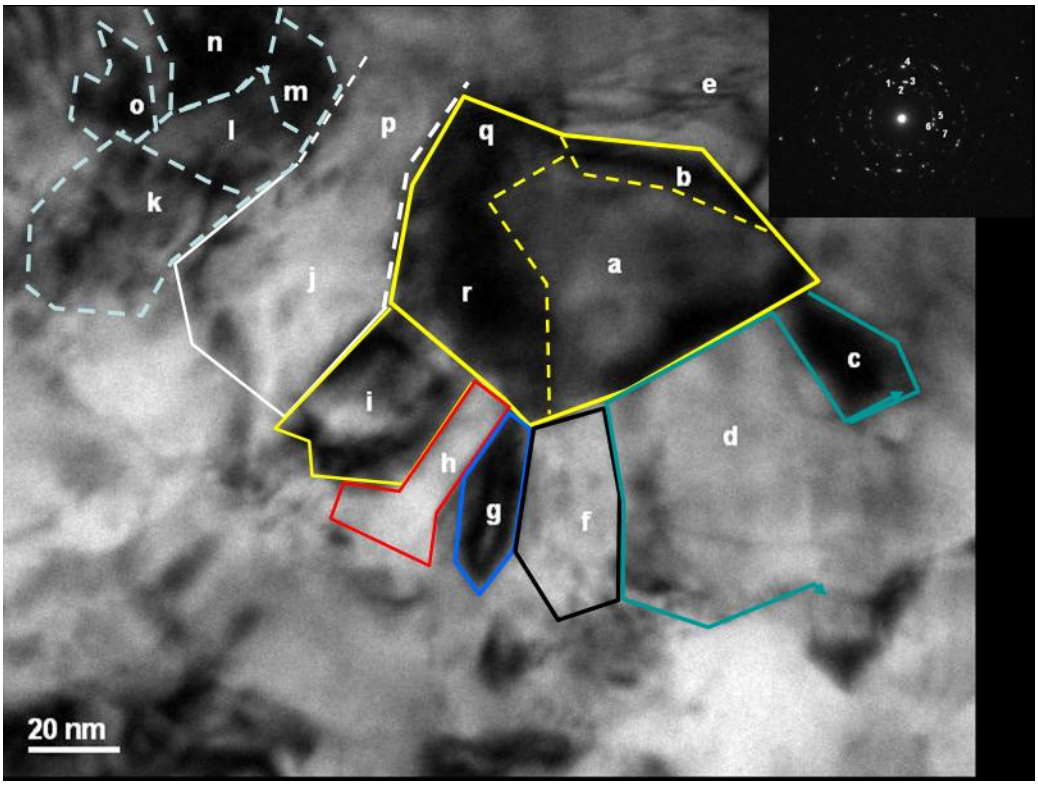

Figure 53. Combined nano-diffraction and dark field imaging results: Bright field image with outlined grains

In Figure 53 a number of grains that are well below 50nm in size are shown. Similar to the 7% and the 16% deformed sample some grains are very similar in orientation, forming grain clusters.

In conclusion, for the 34% reduction in thickness cold rolled NC Ni larger elongated grains could be observed and were analyzed. Aside from larger grains areas with considerable smaller grains are also observable, which could indicate the onset of a more bimodal population of grains with grain sizes clustering about two significantly different values. This result is also reflected in the more statistical grain size analysis (see later section). Evidence of dislocation activity and interactions between gliding dislocation slip system has been found. The activity of more than one slip system at a time is very likely. Different from the 7% and 16% deformed samples these large areas no longer seem to contain grain clusters but rather seem to be single grained.

3.6 NC NICKEL 53% DEFORMED

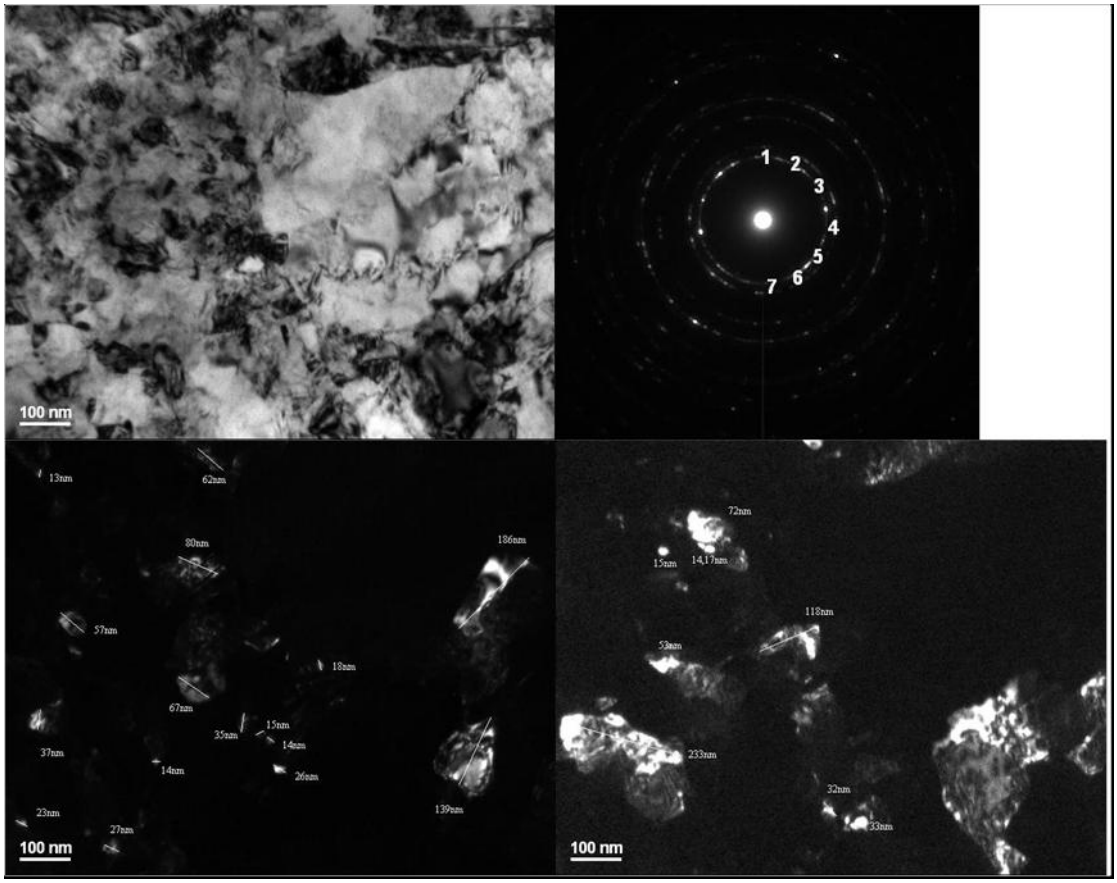

Figure 54. Bright field image (upper left), corresponding diffraction pattern (upper right) and two example dark field images

Following the same procedures as for the other deformation states the average grain size D_{ave} = 74±8nm and the median grain size D_m = 51±8nm have been determined for the 53% reduction in thickness cold rolled NC Ni. This grain size is essentially the same as in the 34% deformed sample of the NC Ni. The dark field image on the lower left (Figure 54) shows some very small grains. However, in the dark field image on the lower right grains considerably larger than 100nm are discernable. Furthermore, in these larger grains the defect concentration seems to be elevated.

Figure 55 shows another dark field image that clearly shows enhanced defect content. The bright field image in Figure 56 depicts an area used for local orientation measurements. Considerable grain overlap is observable for the zero-tilt geometry used for the bright field TEM imaging, which in some cases results in moiré fringe contrast.

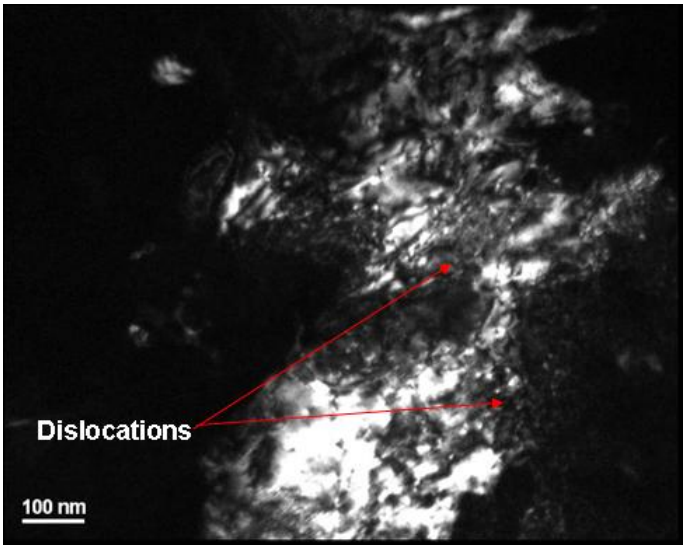

Figure 55. Dark field of a heavily defected area

Moiré fringe analysis has been carried out in areas were the fringe spacing could be determined with confidence (shown in Figure 56). Similar to the cases observed in the 34% deformed sample, here in the 53% deformed sample of NC Ni the large area depicted in center of the bright field overview of Figure 56 seems to be a single grain rather than an agglomerate of many smaller grains. This was observed for a number of other cases and seems to more generally the case for the 53% deformed NC Ni.

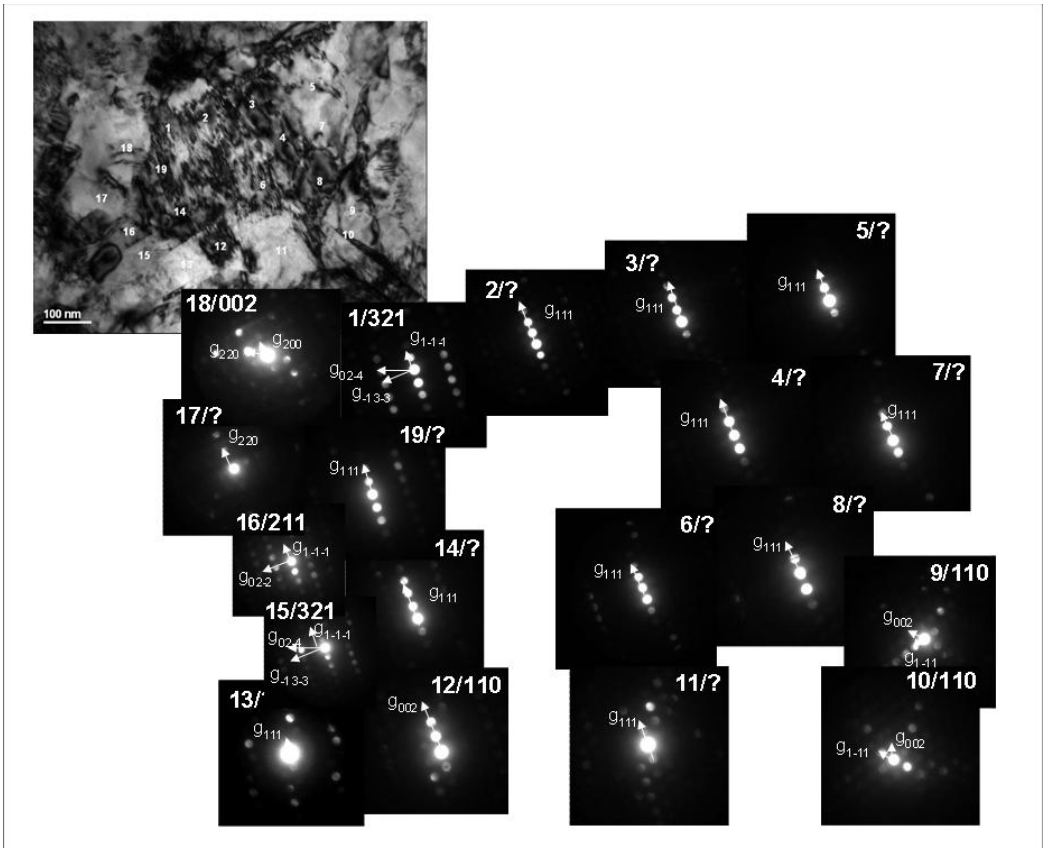

Figure 56. Local orientation distribution measurement: Bright field image including nano-diffraction patterns form the indicated area

The dimension of this large grain in Figure 56 and Figure 57 exceeds the frame of the image at the top right. The grain is at least several 100nm large. Dark field image analysis (not shown here) has been carried out as well.

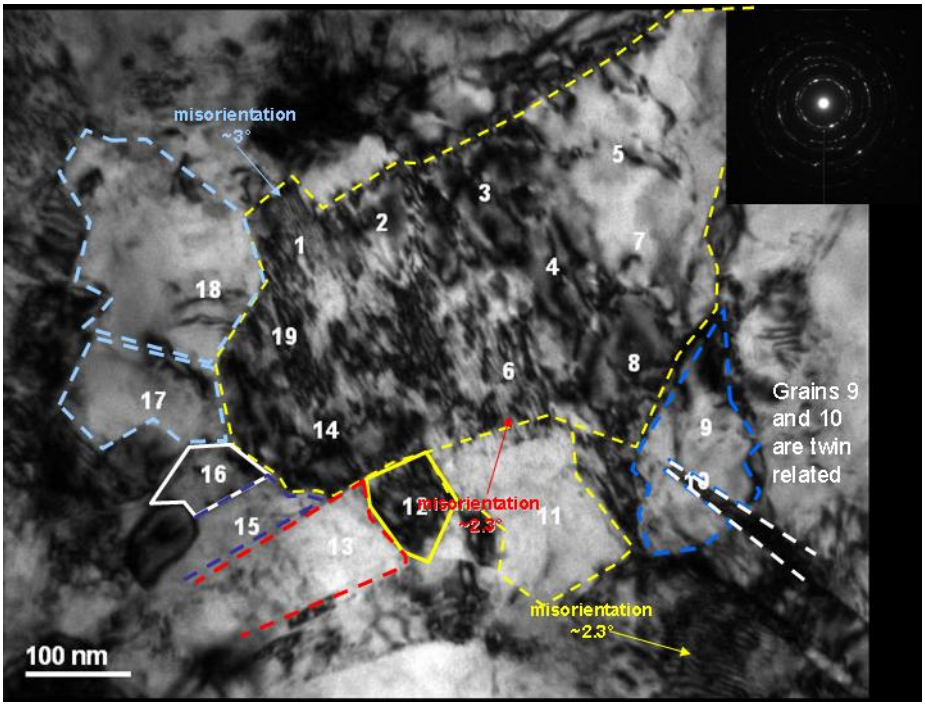

Figure 57. Combined nano-diffraction and dark field imaging results: Bright field image with outlined grains

The grains neighboring this larger grain seem to be of different orientation. Figure 58 shows the bright field image and nano-diffraction pattern analysis of another area that includes a grain that is about 500-600nm in diameter. The selected area diffraction pattern in Figure 59 (inset in the upper right corner) indicates that most grains are close to a <110> type zone axis orientation. This observation is consistent with the nano-diffraction pattern analysis, as an excited row of 111 diffractions is contained in a <110> type zone axis

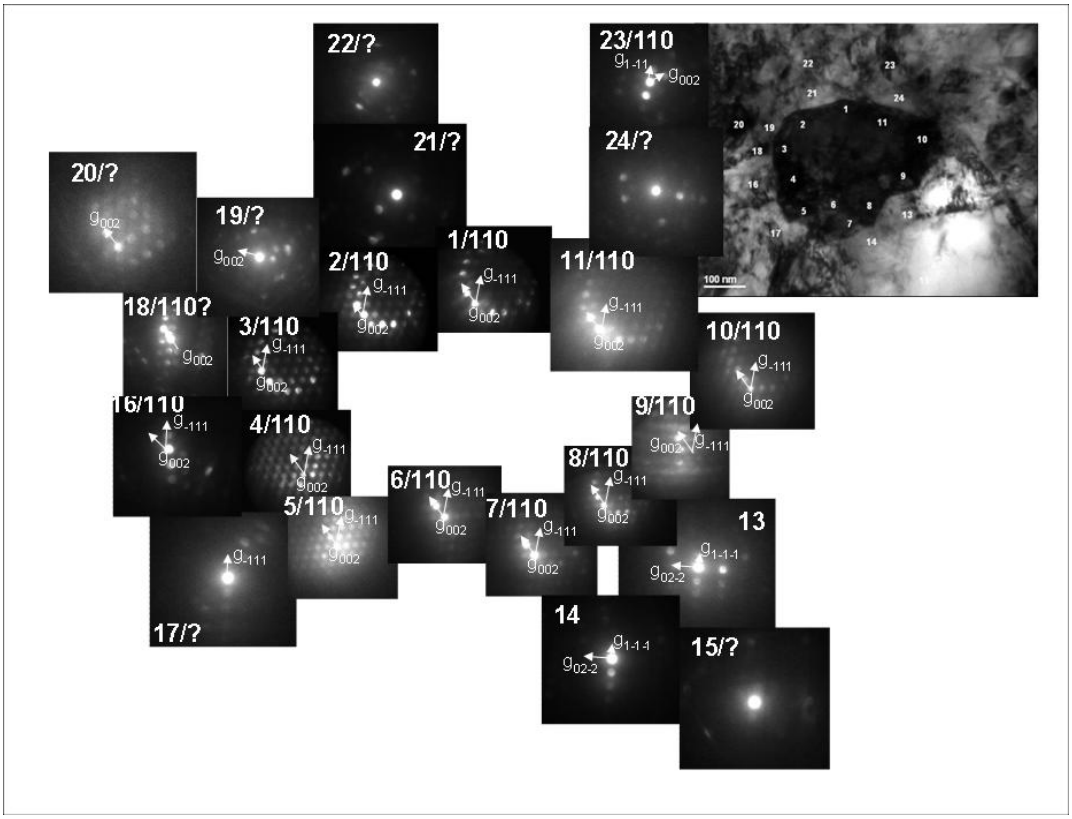

Figure 58. Local orientation distribution measurement: Bright field image including nano-diffraction patterns form the indicated area

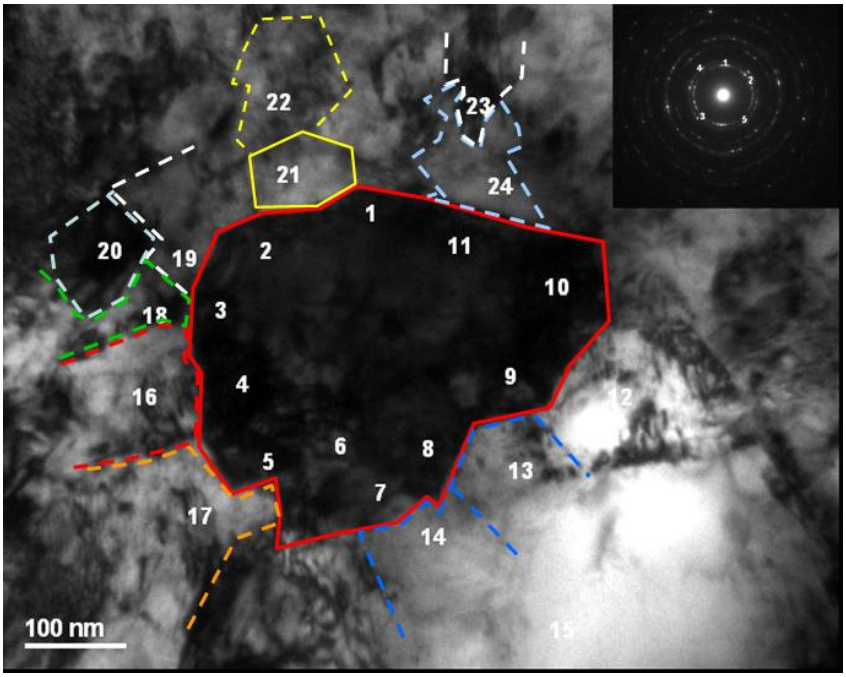

Figure 59. Combined nano-diffraction and dark field imaging results: Bright field image with outlined grains

Dark field image analysis (not shown here) has been carried out as well. The grains surrounding the large grain are of significantly different orientation. It seems reasonable to hypothesize that the large grains observed with regularity in the 53% deformed NC Ni could have originated from the grain clusters seen in the 7% and 16% deformed NC Ni samples by some mechanisms of coalescence resulting in these bigger grains.

In conclusion, as compared to the 16% and 34% deformed NC Ni samples no further increase in grain size has been observed in the 53% deformed sample. Similar to the 34% deformed sample the analyzed areas studied by TEM contained larger grains (diameters of 500nm and larger) rather than just larger agglomerates of smaller grains. Furthermore, similar to the case of the 34% deformed sample the defect or dislocation content in the enlarged grains in the 53% deformed NC Ni is enhanced.

3.7 NC NICKEL 75% DEFORMED

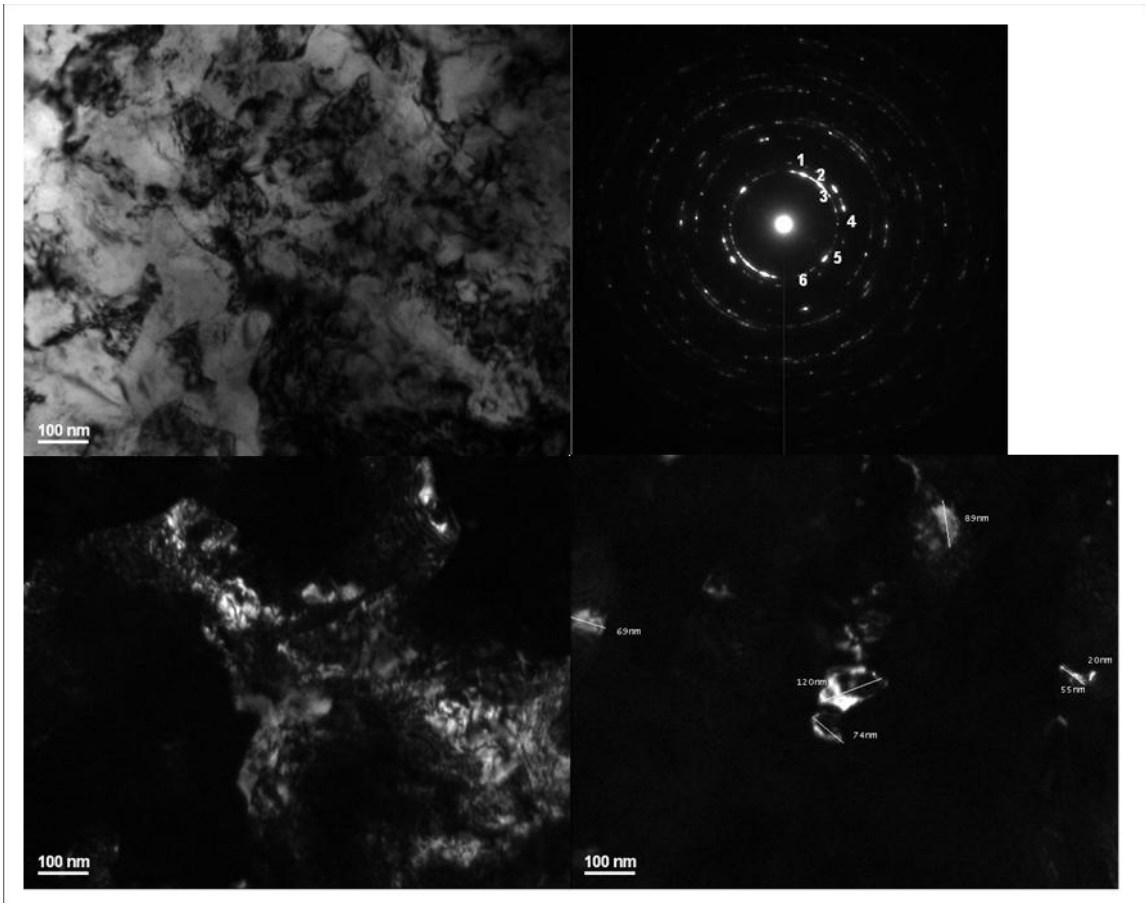

Figure 60. Plane view bright field (upper left), corresponding diffraction pattern (upper right) and two dark field images

The grain size analysis of the 75% deformed NC Ni sample yielded an average grain size of D_{ave} = 111±11nm and a median grain size of D_m = 69±8nm. The grain size increased relative to the 53% deformed state. From the dark field images in figure 60 it can be seen that some regions show grains that seem to be close to 1μm in diameter. The grain size population seems to become bimodal, resulting in an increasing difference between the average and the median grain size. The geometric average might no longer be an appropriate quantity to describe the average grain size. The grain size analysis results will be discussed in greater detail in the next section.

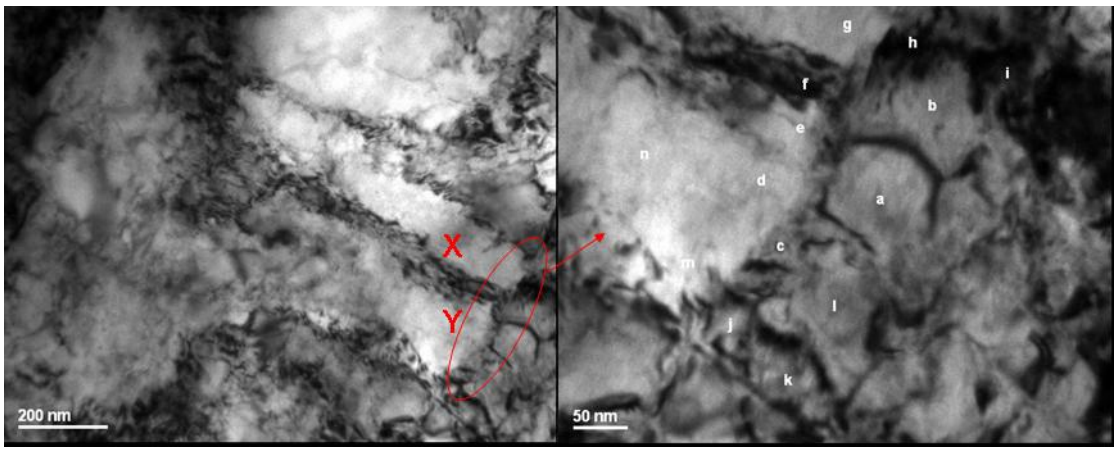

Figure 61. Bright field image showing large elongated regions the indicated region was investigated for local orientation differences.

In the bright field image in Figure 61large elongated regions can be seen, marked as X, Y for instance. This morphological change of grains is very similar to observations typical of coarse grained materials where 'pancaked' and elongated grains are characteristic for heavily cold rolled microstructures. Thus, in coarse grained Ni also elongated grains form upon cold rolling to large strains [33]. The area to the right of the elongated grain marked Y in the left panel of Figure 61 has been investigated for local orientation differences. If these grains are of similar orientation to each other and/or the elongated grain marked Y, it seems reasonable to propose that a coalescence mechanism is responsible for the stress induced grain growth. If, however, the grains are of very different orientation it may imply that the migration of mobile high angle grain boundaries (HAGBs) similar to the phenomena characteristic of recrystallization related grain growth might be associated with the strain induced grain growth. Figure 59 shows the results of the local misorientation analysis of the relevant area indicated in Figure 61. Figure 62 and Figure 63 show that the grains, to the right of the elongated areas marked in Figure 61, are of similar orientation. This would be consistent with a coalescence

mechanism of some sort being responsible for the observed cold rolling induced grain growth. The inset diffraction pattern (Figure 63) confirms the results from the combined nano diffraction pattern and dark field (not shown here) analysis. Most of the analyzed area is close to a <112> orientation. This observation is consistent with the XRD texture findings (see discussion part).

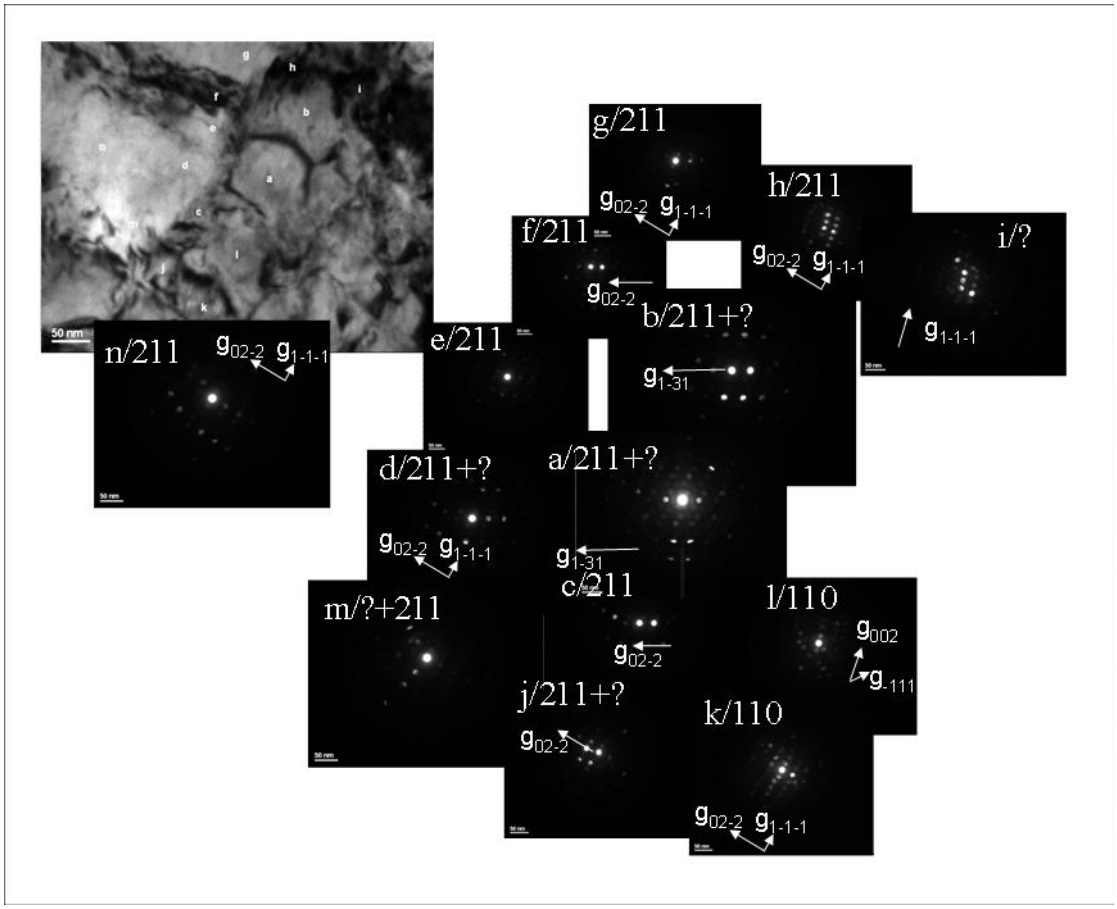

Figure 62. Local orientation distribution measurement: Bright field image including nano-diffraction patterns form the indicated area

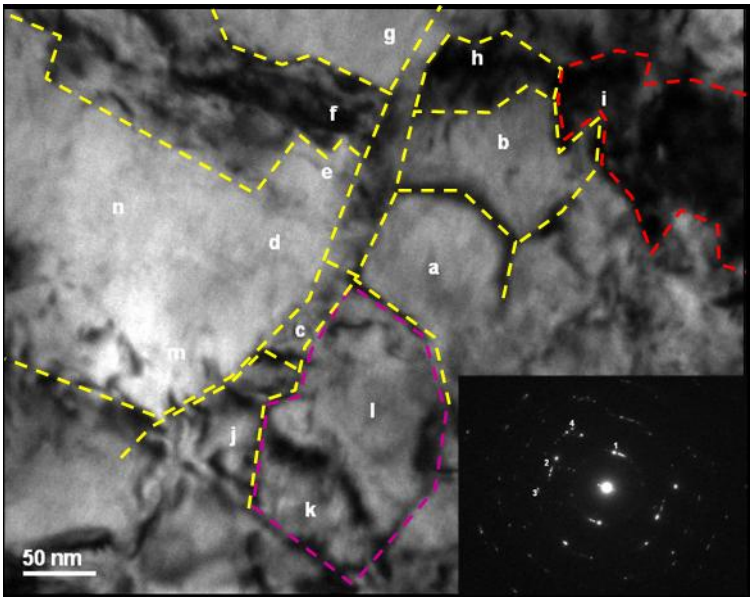

Figure 63. Combined nano-diffraction and dark field imaging results: Bright field image with outlined grains

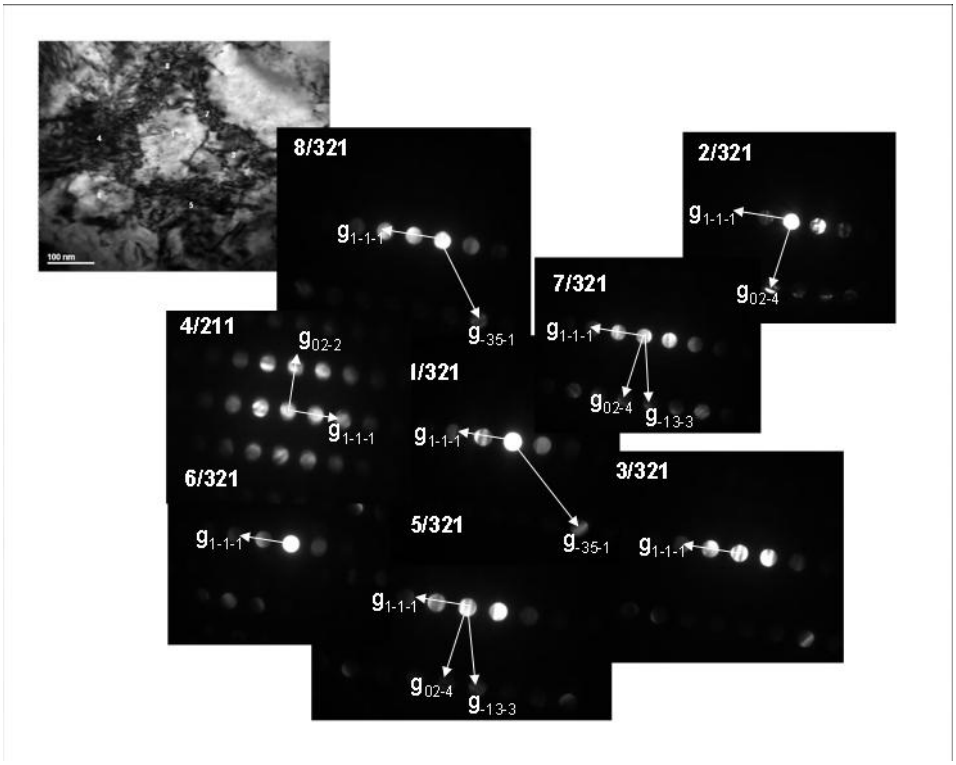

Figure 64. Local orientation distribution measurement: Bright field image including nano-diffraction patterns form the indicated area

Figure 64 and Figure 65 show another area, which has been analyzed for local misorientations. The bright field image in Figure 65 shows that essentially the whole field of view is of very similar in orientation. The inset diffraction pattern also indicates a high concentration of <112> orientations, similar to the first analyzed area.

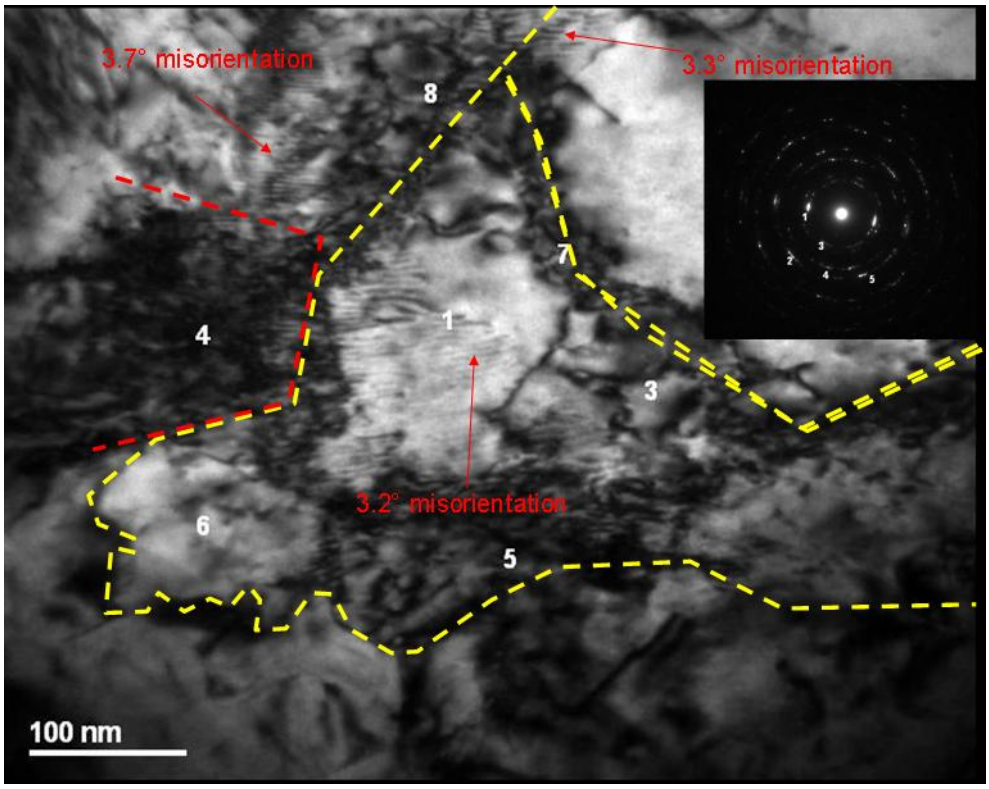

Figure 65. Combined nano-diffraction and dark field imaging results: Bright field image with outlined grains

The small misorientations are accommodated by the dislocation content. Careful tilting experiments were carried out to improve resolution of the diffraction contrast of the defects in the bright field TEM images [34]. The results are shown in Figure 66.

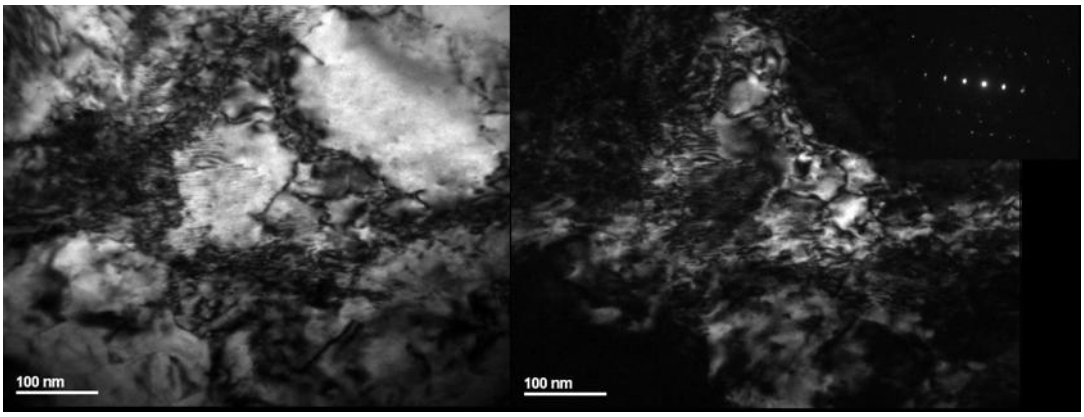

Figure 66. Bright field image, dark field image and corresponding diffraction pattern.

Dislocation tangles can be seen, as well as crossing and intersecting dislocation line segments. Multiple different dislocation glide systems have to be active simultaneously to produce such intersecting dislocation arrangements.

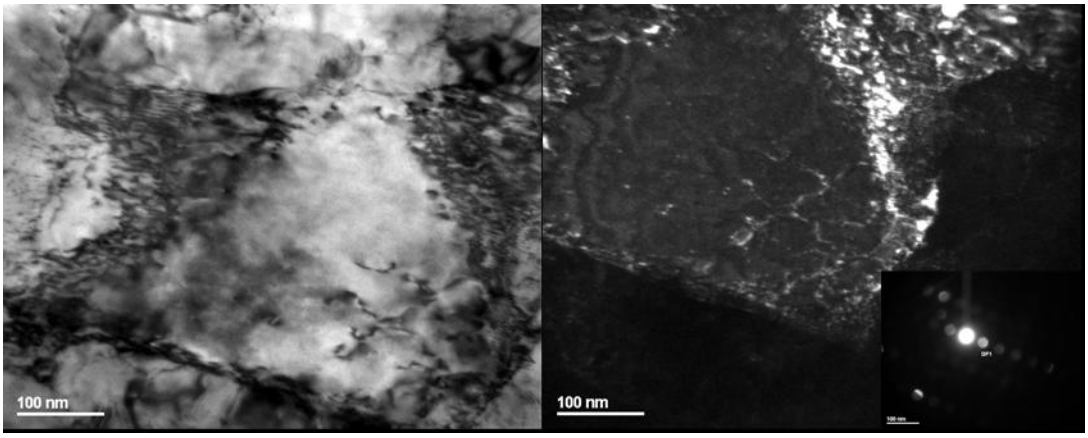

Figure 67. Bright and dark field image and corresponding nano-diffraction pattern

Figure 67 shows another example of dislocation interaction within a large grain. In the bottom right corner of the grain in Figure 67 intersecting dislocations forming tangles are discernible.

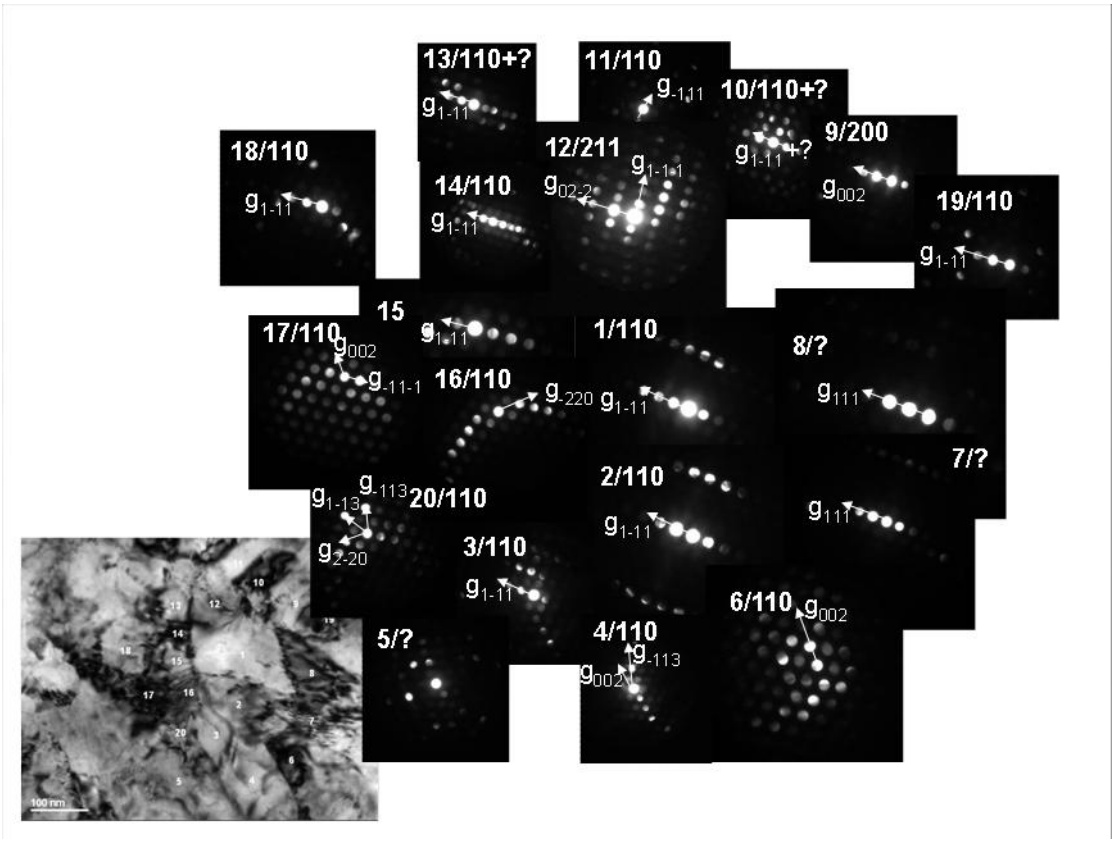

Figure 68. Local orientation distribution measurement: Bright field image including nano-diffraction patterns form the indicated area

The area shown in Figure 68 and Figure 69 shows an example of a region that still contains a number of grains that is considerably smaller than 100nm. The result of the combined nano-diffraction pattern and dark field (not shown here) analysis is shown in Figure 69. Similar to the observations made for the 7% and 16% deformed samples several individual grains are of very similar orientation, forming grain clusters.

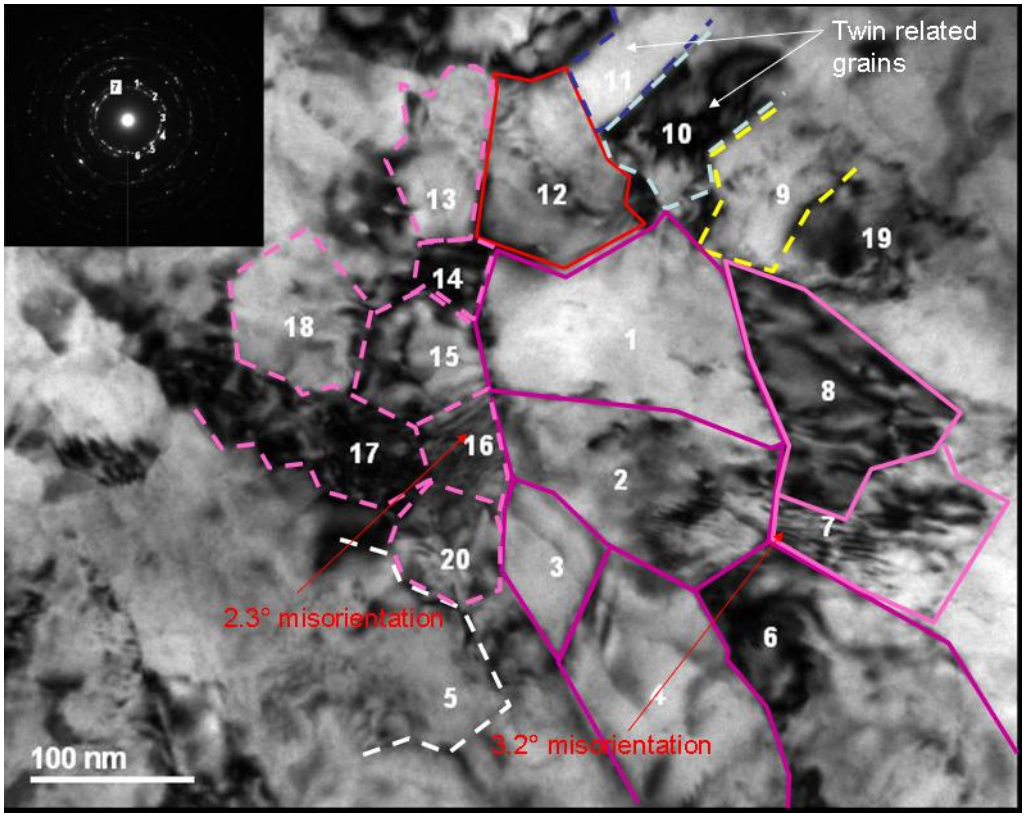

Figure 69. Combined nano-diffraction and dark field imaging results: Bright field image with outlined grains

Summing up, for the 75% deformed NC Ni regions of elongated and large grains have been observed, which is similar to grain morphologies observed typically in heavily cold rolled coarse grained material. The grain size increased further for this highest deformation state studied here. Grains with diameters in the µm range are observable. Furthermore, the difference between the geometric average and the median grain size has become very large, indicating that the population of grains may have become multimodal and can no longer be described by a typical distribution function, such as log-normal distribution. This will be addressed separately in the next section. Local misorientation measurements indicate that grains in front of elongated features are of similar orientation, indicating that stress induced grain growth might be facilitated by grain coalescence. Dark field imaging clearly shows the presence of dislocations. The

dislocation line morphologies exhibit jogs and tangles and clearly indicate dislocation interactions. This would be consistent with more than one slip system being simultaneously active in these larger grains, which are frequently observed in the microstructure of the 75% deformed NC Ni.

3.8 GRAIN SIZE TRENDS

Grain size measurements were carried out by dark field TEM imaging. The limitations in accuracy were pointed out in the previous sections. Grain sizes were measured using the Digital Micrograph software package from Gatan, Inc.. The number of grains in different size regimes was counted. The bin size was chosen as 10nm initially. Here we display the grain size measurement data for bin size of 40nm, which still captures the main features of the changes in the grain sizes for the different cold worked states of the NC Ni. The number of grains analyzed was 419 in case of the undeformed NC Ni, 321 for the 7%, 136 for the 16%, 114 for the 34%, 267 for the 53% and 196 for the 75% deformed sample. The variation of number of grains analyzed for different states is related to a combination of effects from the size of the grains present in the materials and the TEM thin foil sample quality. These results are the basis for all following graphs.

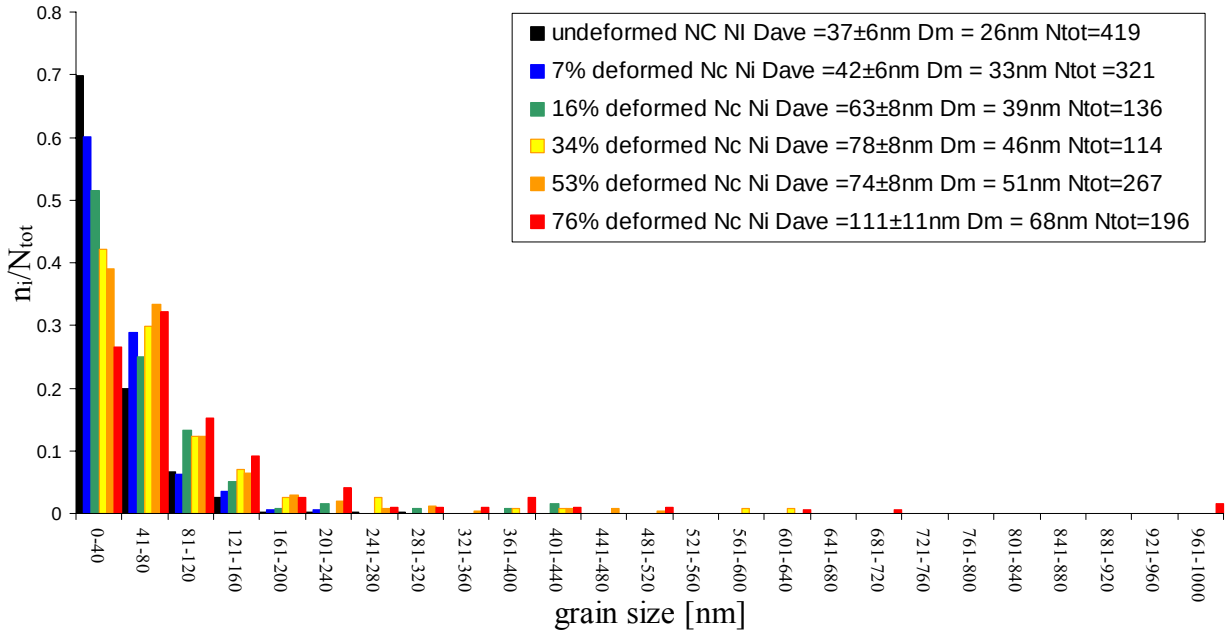

Figure 70. Number fraction versus grain size to represent the change in grain size population with strain vs. size bins

As no distribution functions will be fitted to the observed results, the measurements will be referred to as grain size populations rather than grain size distributions. In Figure 70 the change in grain size population with strain is depicted. The number of grains in a bin was normalized by the total number of all measured grains belonging to one deformation state. All the different states are compared in Figure 70. A very large fraction of grains (70%) of the undeformed NC Ni are in the first size bin, i.e. up to 40nm in diameter. With increasing amount of cold rolling reduction the fraction of smaller grains decreases and increasingly larger grains appear. The population assumes bimodal character with increasing strain. This behavior is confirmed when the relative change with respect to the undeformed sample is plotted with strain (Figure 71)

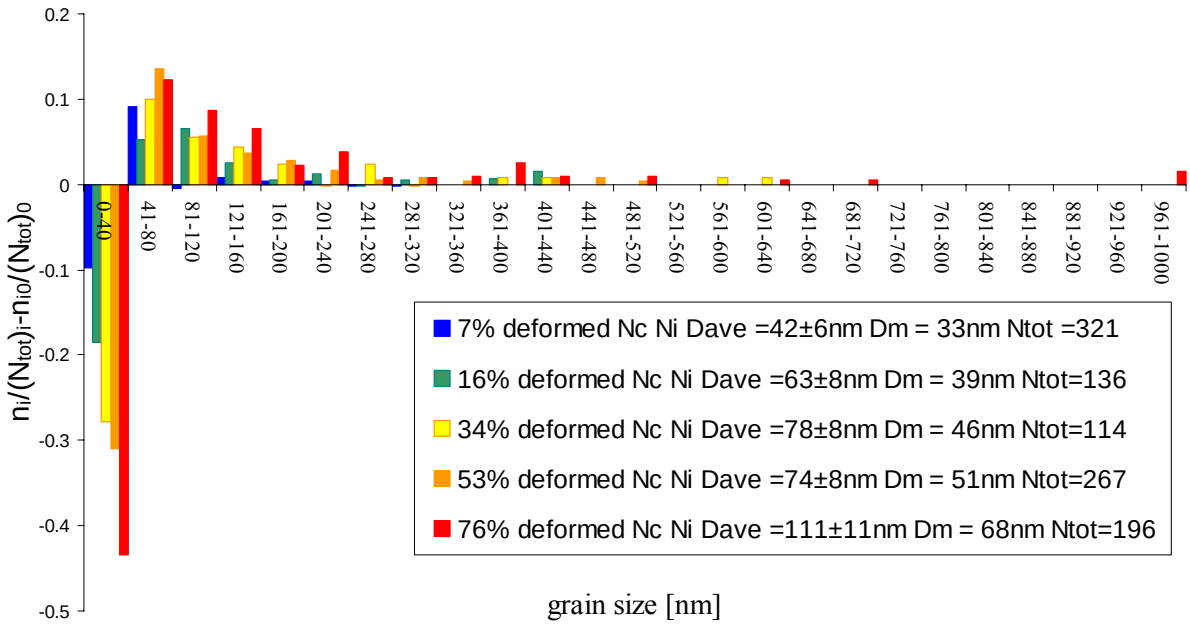

Figure 71. Relative change in grain size population with strain vs. size bins

In the plot in Figure 71, we subtracted the normalized number of grains in the undeformed sample in the same size from the normalized number of grains in every bin for the different deformed states. Negative numbers mean fewer grains as compared to the undeformed sample were counted in that size regime and vice versa for positive numbers. This plot confirms the trend that the grains in the smaller size bins disappear and the appearance of larger grains with increasing amounts of deformation. Considering just the number fraction of grains, the contribution of the larger grains to the overall populations that represent the NC Ni microstructures seems to be rather small. However this result might be deceiving. Figure 72 shows the change in area fraction vs. size bins with increasing amount of strain. The area fraction has been chosen over the volume fraction to show the significance of large grains as two problems arise when measuring grains via TEM. One problem arises from sampling. Usually measurements tend to be biased naturally. The bigger grains get the larger the probability

becomes that some parts of the grain are not contained in the field of view. As a result they cannot be evaluated. This leads to an overestimation of smaller grains [35]. Another difficulty arises when trying to unfold the distribution.

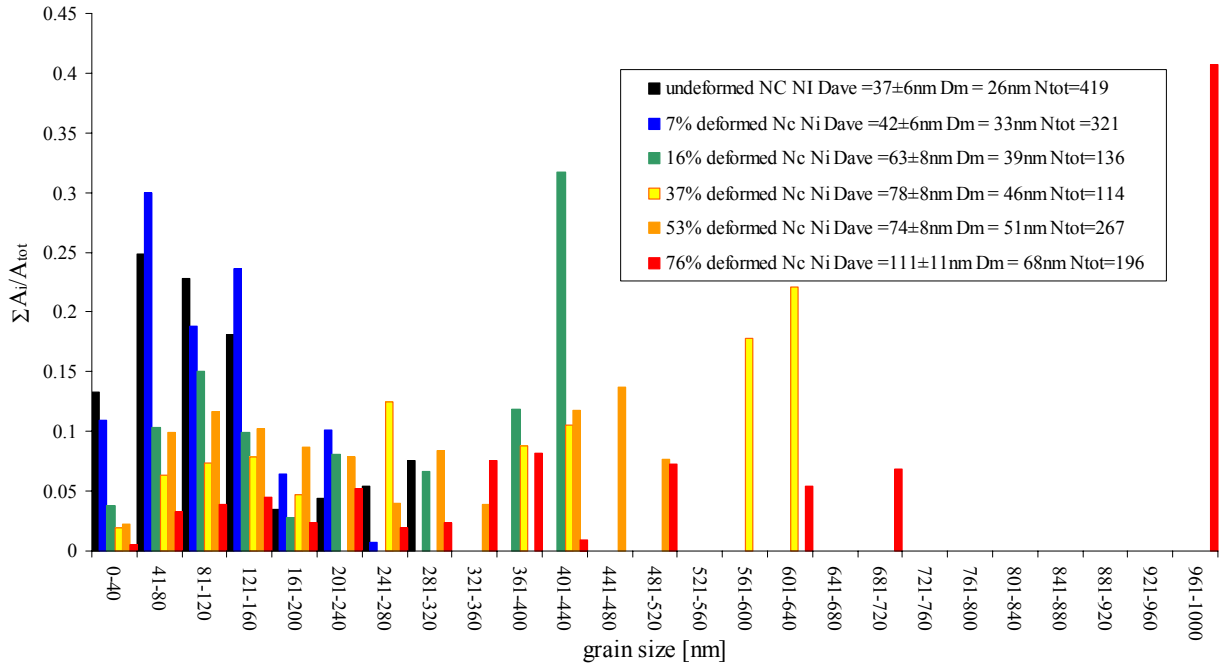

Figure 72. Change in area fraction with strain vs. size bins

As shown in the graph in Figure 72 displays a plot of the sum of grain areas in a certain bin size normalized by the total area of the grains analyzed vs. size bins. The area of a grain was computed from the grain diameter assuming spherical grains. The problem arises from the assumption that all the measured grains in the plan view TEM image cut through the center of the grain. However, the larger the grains are, the larger becomes the probability not to cut through the center of the grain. If the grains are not cut through the center large grains will appear smaller. Smaller grains tend to be overestimated. As no cross sectional information is available at this point two mathematical techniques are available to correct for this problem [36]

assuming spherical grains. Due to the irregularity of the measured population both the inverse method [37] and the forward method [38] will pose considerable mathematical effort and in addition introduce fitting approximation errors. Whether the assumption of spherical grains would be applicable is also questionable, as grains likely change their shape during the deformation process. Considerable deviations from a spherical shape are to be expected. The main point of showing the change in area fraction as a function of strain is to qualitatively outline the importance of the appearance of larger grains. For these reasons the population has not been unfolded. Of course, this is a first approximation. But, it serves the purposes of our study and clearly suffices to clarify how dramatic the impact of the largest diameter grains is on the material area and concomitantly on the volume relative to that associated with the smaller grains. The graph in figure 72 shows that grains larger than 300nm make up a large fraction of the total volume for the NC Ni samples of at least 16% of deformation. Even though the number of large grains might be rather small, they make up a large percentage of the total volume and can therefore no longer be ignored. This trend becomes even more obvious when the change in cumulative area fraction with strain is plotted vs. size bins.

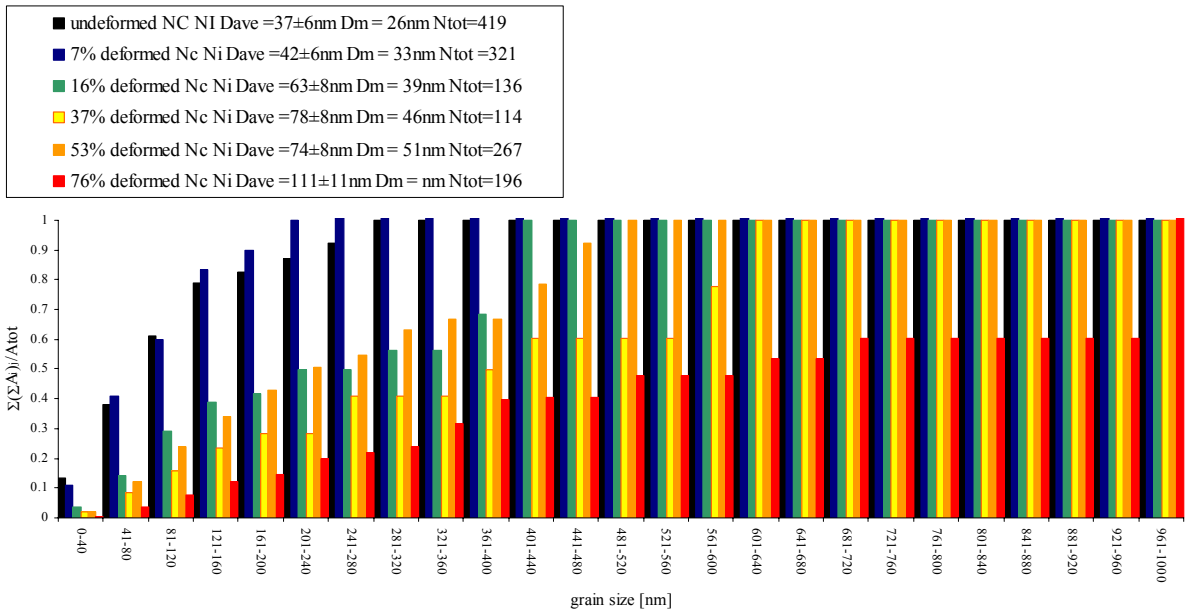

Figure 73. Change in cumulative area fraction with strain vs. size bins

Here the sum of the previous normalized area fractions up to and including the normalized area fraction of the size bin are plotted vs. size bins. It can be seen that for the undeformed and 7% deformed sample 50% of the total volume is made up by grains that are smaller than ~100nm. To reach to 50% area fraction mark grains up to a size of ~360nm, ~500nm, ~400nm and up to 1μm have to be included for the 16%, 34%, 53% and 75% deformed sample respectively. In the 75% deformed sample 40% of the total area is made up by the few grains that are ~1μm in size. As explained above, due to the irregular shape and the uncertainty of the measurements no attempts to fit distribution functions to these grain size populations and volume fractions will be made. If the error or the uncertainty is roughly the same for all the measurements, the error should cancel if the change is considered. Therefore, a qualitative discussion of the change in grain size population was the main goal of this study. However, some conclusions on the shape of the grain size population can be drawn form the previous graphs. The undeformed, 7% and to some degree

the 16% and 34% deformed sample show a steady increase until they reach a plateau value. This behavior is observed when log normal or Gaussian peak functions are plotted cumulatively. However the 53% and 75% deformed samples show a steady increase reach a plateau value before a second increase to a final plateau value can be seen. Such a behavior is associated with some type of non-monomodal, e.g. bimodal, distribution. It should also be mentioned that this change in behavior coincides with the marked change in texture after about 40% deformation and the observations made by the TEM analyses that larger entities seem to contain single grains rather than grain agglomerates for these about 40% or larger rolling reductions in thickness. This indicates that not all grains just become bigger.

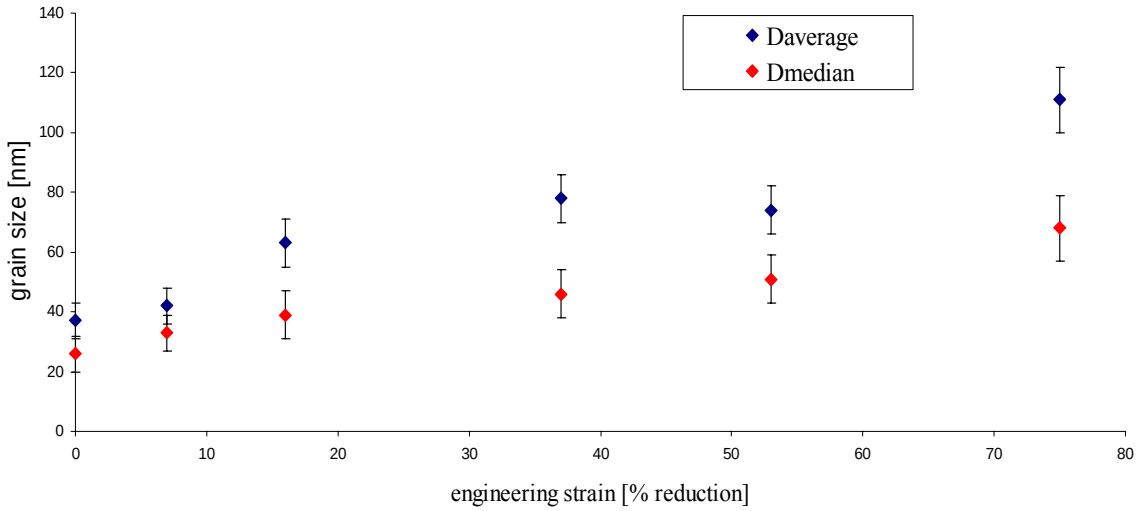

Figure 74. D_{ave} and D_m vs. percent reduction

Such a behavior would simply shift the entire population to larger grain size bins. The number of smaller grains decreases and much larger grains appear. This corresponds to a decrease in the

smaller size bins and an increase in large size bins as observed in Figure 70 and Figure 72. Figure 74 shows how the average and the median grain (= grain size, where half the number of grains are smaller and the other half is larger than the median size) size changes with percent reduction by cold rolling. For both the average and the median of the grain size a change can be observed that is larger than the error from the measurement for increasing deformation amount. The change in D_{ave} is always larger than the change of the median. However, from the discussion above it becomes clear that with increasing amounts of deformation the grain size population assumes more and more the character of a bimodal distribution. Hence, if a geometric average is used the grain size will be affected more significantly by the few grains with large diameters. The median grain size may offer a better but still not fully accurate estimate. The important conclusion, however, is that the grain size truly increases, which is not significantly affected by the choice of average versus median grain size as the representative of the microstructure.

In summary, changes in grain size population with amount reduction are observed. The number of smaller grains decreases, larger grains form. Large grains become more important as the material is deformed to larger strains. The grain size populations of the 53% and 75% deformed samples have multimodal or bimodal character. Significant changes in grain size population coincide with significant changes in texture (XRD) and grain morphology and dislocation content in the large grains (TEM observations). The average grain size increases and grain growth occurs during cold rolling of the NC Ni.

3.9 HARDNESS RESULTS

Vickers hardness measurements were performed using a dwell time of 10s and loads of 50g and 100g. The change in Vickers hardness with percent thickness reduction by cold rolling is plotted in Figure 75.

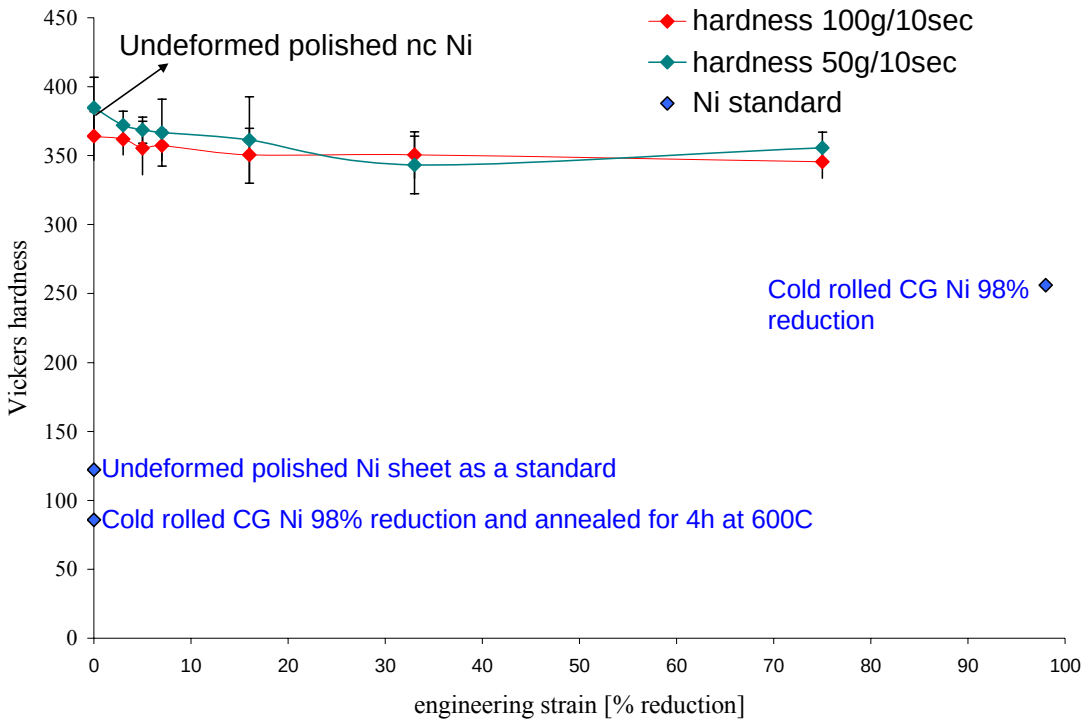

Figure 75. Vickers micro hardness vs. percent reduction as compared to undeformed and deformed coarse grained Ni

For comparison to the electrodeposited NC Ni hardness measurements for coarse grained (CG) electrodeposited Ni in the heavily cold rolled and the fully recrystallized states are included in Figure 72. Furthermore, the hardness for commercially available polished Ni sheet (Alfa Aesar) is included in Figure 72 also. An increase in hardness due to a grain size effect can be seen when comparing the undeformed (0% reduction in thickness, Figure 72) states for the CG Ni, about 80

to 120 H_v, with the NC Ni, 360 to 380 Hv. Within the error bar no change in hardness is observable for the 50g as well as the 100g load measurement for the NC Ni as a function of cold rolling reduction in thickness or engineering strain (Figure 72). Both measurements yield very similar results. The hardness does not change with increasing amount of plastic deformation. This behavior is very different form the behavior of coarse grained Ni. A clear increase in hardness is observable after plastic deformation to large strains for the CG Ni, namely about 80 Hv at 0% and about 250Hv at 98% reduction by cold rolling (Figure 72).

4.0 DISCUSSION

4.1 TEXTURE CHANGES

The undeformed NC Ni shows a strong cube fiber texture (Figure 21, Figure 25 and Figure 26). This is consistent with a typical growth texture for electrodeposited Ni [39]. More recent studies show that the growth texture depends on the deposition conditions [40]. In the future it might be possible to investigate NC Ni with a different starting texture.

The texture that develops during cold rolling of NC Ni is very similar to textures that develop during rolling of coarse grained Ni. The preferred slip systems in FCC metals are {111} <110>, which are typically associated with the lowest critical resolved shear stress. There are 12 crystallographically equivalent slip systems of the type {111} <110>. The large number of possible active slip systems makes it easy to achieve compatible deformation and large ductility in polycrystalline aggregates. If multiple slip systems are active and hardening of individual systems is allowed the cold rolling texture typically observed in FCC metals can be rationalized according to a Taylor model [30]. What kind of texture develops during cold rolling in FCC metals also depends on the stacking fault energy. Intermediate to high stacking fault energy materials, where mainly compact core unit dislocations of the type $\frac{a}{2}\langle 110\rangle$ are active by glide, contain mainly the <111> {112} Copper (high stacking fault energy) and the <634> {123} S fiber components in their cold-rolling textures. A characteristic cold-rolling texture develops,

which is associated with characteristic pole figures, such as those shown in the top row of figure 73. In low stacking fault energy FCC materials unit dislocations dissociate into pairs of partial dislocations $\frac{a}{6}\langle 112\rangle$ bounding stacking faults and during glide of these extended core dislocations on the {111} planes cross-slip is rendered difficult. Furthermore, massive glide activity of these stacking fault bounding extended core dislocations on parallel glide planes eventually leads to mechanical or deformation twinning plays, which plays a major rule during deformation and cold-rolling texture development. The resulting deformation texture in low stacking fault energy FCC materials contains mainly the brass component <112> {110} and hence, is very different (Figure 76 middle row) from that in high stacking fault energy FCC materials. Thus texture development during cold rolling in FCC metals depends on the details of the operative deformation mechanism.

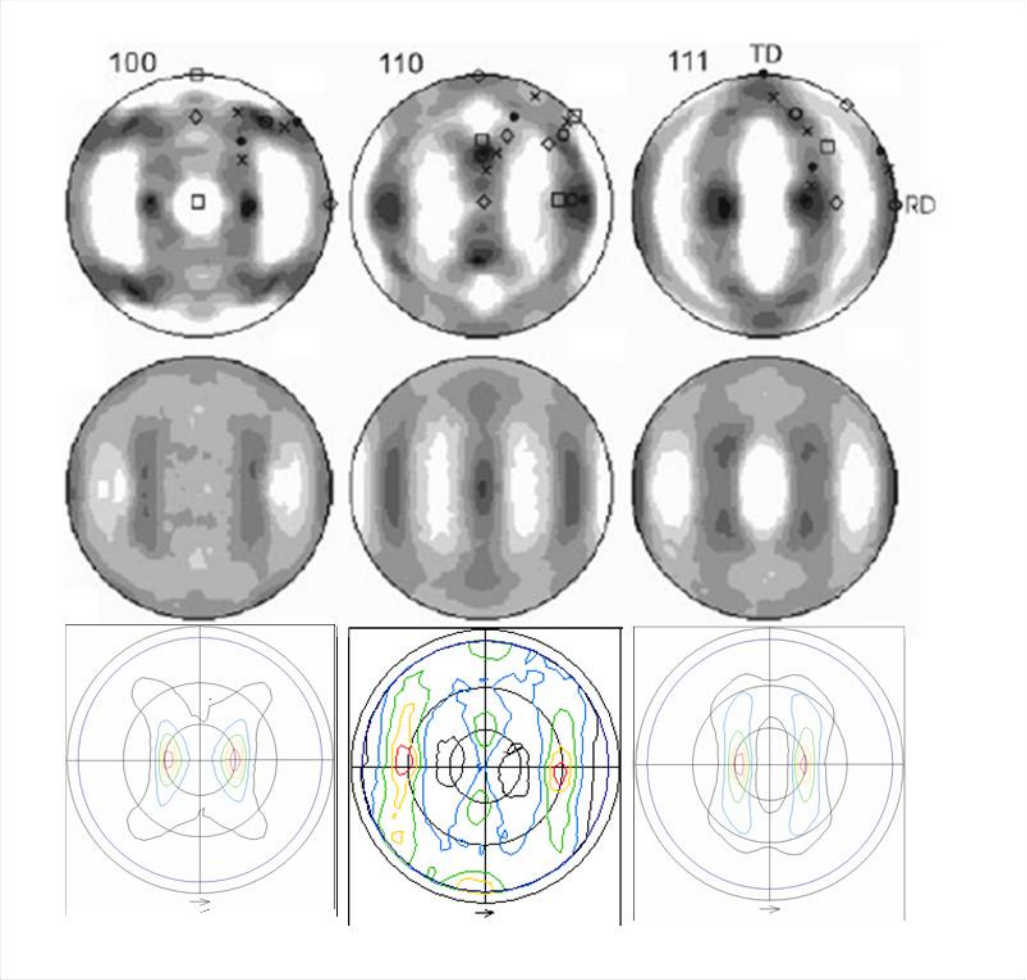

Figure 76. 100, 110, and 111 pole figures of cold rolled high stacking fault Cu (top row) of cold rolled low stacking fault brass (middle row) measured by synchrotron radiation [41] and the 100, 110 and 111 pole figures of the deformed NC Ni (bottom row)

Figure 76 shows a comparison of 100, 110 and 111 pole figures of cold rolled NC Ni (Fig. 76 bottom row) and measured cold rolled Cu (Figure 76 top) [41]. Good matching of the strong intensities is observed. The 100 pole figure might be ambiguous, but the 110 pole figure shows displaced center intensities matching with the Cu pole figure in the top row. The 111 pole figure of the cold rolled NC Ni (bottom row, Figure 76) shows two maxima displaced away from the center of the pole figure rather than four intensities as is characteristic in the brass pole figure (middle row, Figure 76). As previously pointed out, the average grain size of the NC Ni studied here is larger than the critical grain size for which the peak in yield stress and hardness is

predicted. That is, the NC Ni materials investigated here have average grain sizes residing in the regime where a Hall-Petch type relationship between grain size and hardness is expected. Not ruling out grain boundary rearrangement processes, dislocation mediated plasticity is expected to be mainly responsible for facilitation of plastic deformation. The main texture components associated with the cold rolling textures represented in the pole figures of Figure 76 can be explained using the Taylor model. The Taylor model, however, assumes that dislocation interactions (hardening of individual slip systems) occur. In the NC Ni originally the average apparent grain size is such that only one dislocation can be present in a grain at a time. The conventional dislocation interaction based work hardening mechanisms are not available to the undeformed NC Ni. However, the grain size trend analysis clearly shows that grain growth occurs during the cold deformation and appears to result in increasing grain size with increasing cold rolling strain. Based on the finding that the texture development of cold rolled NC Ni is similar to that of cold rolled coarse grained Ni and that texture development in FCC metals is deformation mechanism dependent, it would be consistent to propose that dislocation based work hardening should be observed in NC Ni. Furthermore, based on the texture observed in NC Ni after cold rolling it appears reasonable to conclude that twinning does not play an important role during cold rolling of NC Ni. Hence, it is concluded that plastic deformation in the NC Ni during cold rolling is accommodated primarily by glide of unit dislocations producing slip on {111}<110> slip systems., which is consistent with Ni being an intermediate to high stacking fault FCC material.

Grain size analysis shows that significant changes in grain size occur after 16% reduction by cold rolling in the NC Ni. In good agreement analysis of the 111 pole figures (Figure 26) shows an onset of a texture change after 16% deformation. However, the 200 pole figures of the

NC Ni exhibit changes characteristically known for cold rolling texture development from work on coarse grained Ni only after about ~ 40% reduction (Figure 25). This observation corresponds well with a marked change in relative peak intensities of the 200 and the 220 peaks after ~ 40% reduction in thickness (Figure 22). This marked change in the rate of texture development during cold rolling of the NC Ni may be associated with massive dislocation based work hardening taking place in the deforming NC Ni microstructures after about 40% reduction in thickness. The changes in texture discernible in the 111 pole figures after about 16% cold rolling reduction in thickness coincide with grain clustering, the formation of agglomerates of many smaller (~30-50nm) grains of similar orientation observed by TEM analysis (Figure 41).

If storage of non uniform strain occurred in the microstructure the peak broadness should increase. However, within the error margins of the XRD measurements no change in the FWHM was observable from the XRD analysis (Figure 23). While work hardening and non-uniform strain storage would broaden the XRD peaks, an increase in average grain size, especially when the average grain size is in the nm range, is expected to result in a reduction in the width of the XRD peaks. Hence, increases in average grain size and strain storage have mutually compensating effects on the XRD peak width. The results of the grain size analysis clearly (Fig. 74) shows an increase in average grain size. If full compensation is assumed a crude and simple first-order approximation of the stored strain and concomitantly a corresponding dislocation density can be made. The XRD peak broadening due to grain size has been explained [23]

$$B = \frac{0.9\lambda}{t\cos\theta} \qquad \text{Equation 10}$$

(B = broadening in rad; λ = the wavelength, t = grain or particle size)

The change in XRD peak broadening due to strain is given by [23]

$$\beta = 2\varepsilon \tan\theta \Rightarrow \varepsilon = \frac{\beta}{2\tan\theta} \qquad \text{Equation 11}$$

(β = broadening due to strain, ε = strain); the condition for compensation is given by

$$B_1 - B_2 = \Delta B = \beta \qquad \text{Equation 12}$$

(B_1 is the broadening resulting from grain size 1, B_2 the broadening resulting from grain size 2) and

$$\varepsilon = \frac{\Delta B}{2\tan\theta} \qquad \text{Equation 13}$$

Assuming Cu-K_α radiation with a wavelength of λ = 1.542Å, grain size 1 D_m= 26nm grain size 2 D_m = 68nm (the median was used as the more accurate estimate for reasons previously discussed) and using the 400 reflection the stored strain can be estimated

$$\varepsilon \approx 0.0019$$

In first approximation a corresponding dislocation density can be estimated using a Taylor model approach [30] which assumes that the undeformed NC Ni is essentially dislocation free:

$$\Delta\tau = \alpha\mu b\sqrt{\rho}$$ Equation 14

(α is an empirical constant that describes the dislocation character, which for FCC metals can be assumed to be 0.2; μ is the shear modulus; μ_{Ni} = 76GPa, b is the magnitude of the Burgers vector $|\frac{a}{2}\langle 110\rangle|$~0.25nm for Ni; ρ = dislocation density, $\Delta\tau$ = strain increase due to an increase of the dislocation density from 0 to ρ) [42]. Using the result for the stored strain in the microstructure a dislocation density can be estimated as

$$\rho = 1.4 \cdot 10^{11} cm^{-2}$$

This magnitude of dislocation density would be consistent with a heavily cold deformed coarse grained metal and is not unreasonable. Furthermore, this dislocation density value agrees within an order of magnitude with an estimate derived from the experimentally measured hardness values (see later section). Given the broad assumptions and approximations that are required in the estimates performed here, these results derived for the dislocation density via two different routes using the experimental observables of the lack of XRD peak broadening and the hardness are considered to be essentially the same. However, the reader is cautioned here not to be tempted to take these estimates of the dislocation density too literally and refrain from overinterpretation of the numerical values presented here. The dislocation density estimates nevertheless provide qualitative support to the hypothesis that the increase in grain size, which we have determined here experimentally (Figure 71), would be sufficient in magnitude and thus suitable to compensate for the change increase in XRD peak broadening that would be predicted

due to strain storage associated with a very large dislocation density expected for a heavily cold worked metal.

Summing up, the XRD and XRD texture studies show changes that are consistent with concomitant grain growth and the dislocation activity resulting in storage of strain, i.e. work hardening, of the NC Ni during cold rolling. The texture results also indicate that mechanical twinning does not play a major role as a deformation mechanism, implying that plasticity in the NC Ni is facilitated presumably primarily by dislocation glide while contributions from some type of grain boundary mediated mechanisms cannot be excluded based on the XRD work.

4.2 CHANGES IN MORPHOLOGY AND GRAIN SIZE POPULATION

As mentioned above the starting material exhibits a rather strong cube fiber texture. In figure 74 most grains have one of cube directions parallel to the foil normal, whereas the other cube directions can be randomly rotated about the foil normal. TEM diffraction showed an elevated concentration of cube oriented grains confirming the XRD results. For that reason it is not surprising that in the overview bright field image (Figure 24) areas of uniform contrast are observable that are much larger than the average grain size. However, local orientation relationship analysis shows that still a lot of grains are separated by high angle grain boundaries. The cube grains are rotated with respect to each other such that in-rolling plane texture still produces predominantly HAGBs (Figure 74).

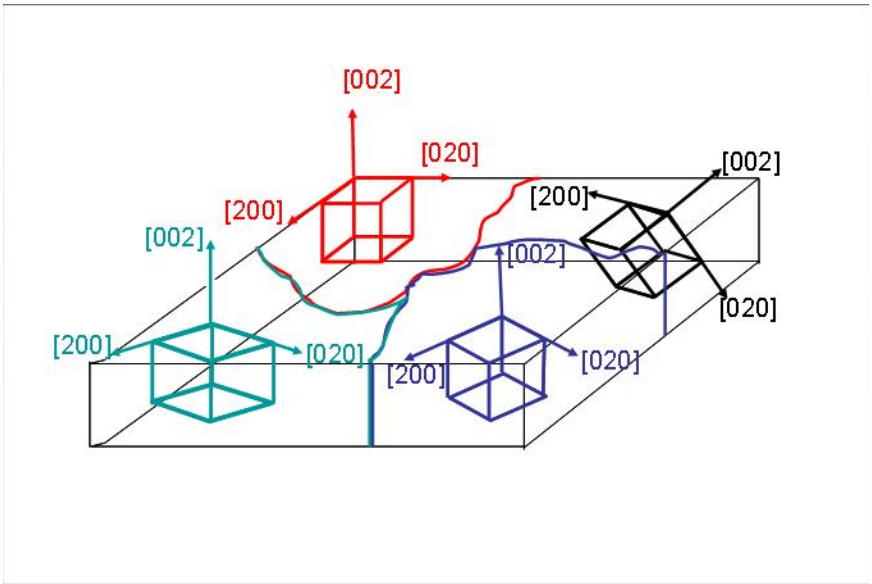

Figure 77. Illustration of grain orientations when a strong cube texture is present. The colored grain areas have one cube direction parallel to the foil normal whereas the other cube directions are rotated about the foil normal

The average grain size D_{ave} = 37±6nm or D_m = 26±6nm determined from TEM measurements is in good agreement with the nominal average grain size D = 20 - 30nm stated by the vendor of the electrodeposited NC Ni material. The grain size population analysis shows a single maximum (Figure 67). For metallic samples of bulk NC material the population of grain sizes is rather narrow. About 50% of the total volume is made up by grains that are smaller than 100nm based on the dark field TEM grain size analyses performed here. It should be noted here, that neither of the populations for any of the different sample states have been unfolded, for reasons explained in the results section. The determined diameters are assumed to always cut through the grain centers. Obviously such an assumption is affected with a certain error. However it still allows qualitative analysis of the changes.

After 7% reduction in thickness the grain size did not change within the error margin of the grain size measurements. However, the local misorientation measurements (Figure 32 and Figure 34) frequently show clusters of grains that are only misoriented by a few degrees, which

could imply LAGBs or at least that only small orientation change is required to accomplish matching of a single set of planes. Cube oriented grains only have to rotate about one axis to become closer in orientation (see colored grains in Figure 74). In addition, the overall energy will be lowered if the grain boundary character changes from that of high angle GB to that of low angle GB. As only single dislocation glide systems are active at a given time, dislocation interactions with the GBs are responsible for these changes, rather than dislocation – dislocation interactions. The GBs might also not be equilibrated after the electro-deposition process used to synthesize the NC Ni. Figure 75 shows an HREM image of a GB of the as deposited NC Ni. A step in the boundary can be seen. Steps are energetically unfavorable. This GB can be considered not to be an equilibrium GB since the step would likely be removed if sufficient thermal or otherwise activation energy were to be provided. Thus, it seem reasonable to suggest that the GB's in the as-deposited and undeformed NC Ni are associated with some excess free energy or simply with non-equilibrium GB structures.

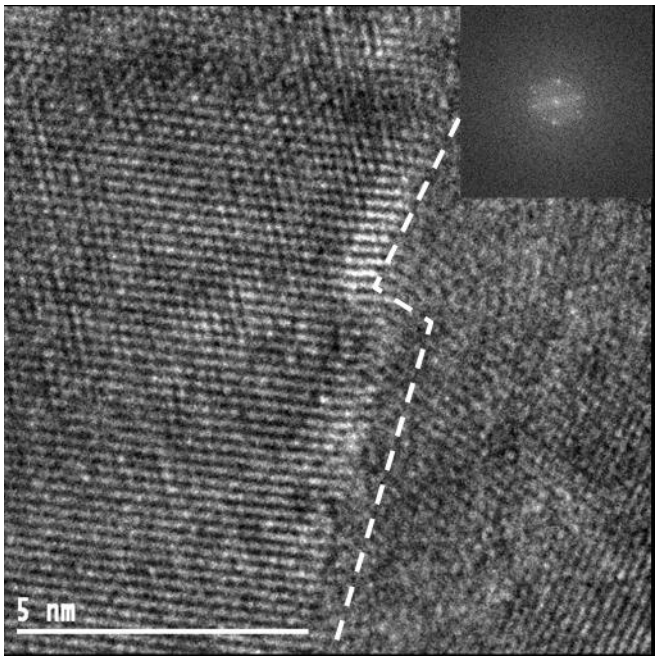

Figure 78. HREM image and FFT of a grain boundary showing a step in the boundary of undeformed NC Ni

The energy provided by the cold rolling deformation might be enough to activate grain boundary relaxation processes. In order to draw conclusions regarding such proposed deformation induced GB rearrangements and GB structure changes, additional and systematic high resolution electron microscopy not only of the deformed but also of the undeformed states is necessary. Future work will include such an investigation of the different states of deformation with HREM to study grain boundaries and defect content. The grain size population did not significantly change as compared to the undeformed state (Figure 70). However, Figure 71 shows a decrease in the fraction of very small grains (0-40nm) and an increase in grains in the size regime 40-80nm. This would be consistent with deformation induced clustering and coalescence of the smallest of grains in the NC Ni during the cold rolling deformation, even after small amounts of thickness reduction. As mentioned above, grains reorient themselves such that their orientations become closer. Grain boundaries likely change their character from high to low angle boundaries due to

energetic reasons. Therefore, the coalescence mechanism seems to be facilitated by the gradual annihilation of low angle grain boundaries rather than a sweeping motion of mobile high angle grain boundaries. Low angle grain boundaries can be thought of as dislocation arrays (Figure 79)

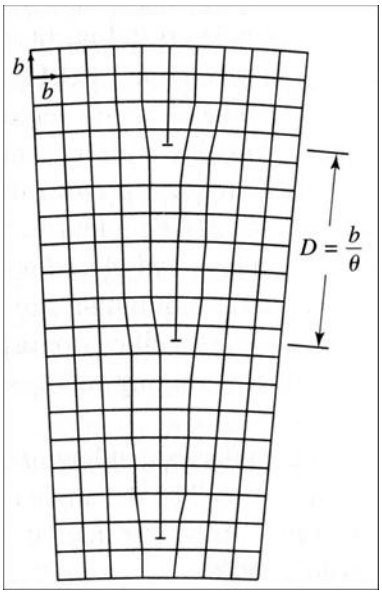

Figure 79. Dislocation based model schematic of a (small) low angle symmetric tilt grain boundary

If dislocations move out of the stable configuration of dislocations forming the low angle grain boundary under an applied stress the boundary will change its character. In other words, the angle of misorientation θ between the two adjacent grains will decrease. As expected, as only single dislocation glide systems can be active in those small grains at a given time, no statistical significant evidence of dislocation – dislocation interactions has been observed. However, it has to be noted that from the lack of observation it cannot be concluded that such interactions do not take place in the microstructure at all. Whether dislocations are observable in the TEM also depends on the imaging conditions [34]. Dislocation – grain boundary interactions (negligible in

CG metals) rather than dislocation – dislocation interactions (dominant in CG metals) are responsible for the observed changes.

In the 16% deformed sample a measurable change in grain size was detected along with an onset in texture change. Some of the clusters of smaller grains must have produced grain coalescence, forming larger grains resulting in the significant change in grain size. The local orientation relationship analysis (Figure 38) shows that most grains in the area are separated by low angle grain boundaries. Larger clusters of similarly oriented grains are observable frequently. These observations are in good qualitative agreement and consistent with the grain size analysis. Figure 67 and Figure 68 show the appearance of grains that are several 100nm in diameter.

In the 34% deformed sample the trend of clustering seems to continue with even higher frequency. Coalescence is confirmed as much larger grains (Figure 46 and Figure 51) were observed. Aside from very large grains, also regions of still very small grains were found. These results are consistent with the grain size population results (Figure 70). The relative change in grain population (Figure 71) with strain clearly indicates that a lot of the very small grains already had disappeared. Larger grains appear which exceed the maximum grain sizes observed in the NC Ni of lower reduction in thickness by cold rolling and the undeformed material. In addition, evidence of dislocation storage was found after 34% reduction by cold rolling (Figure 51). As grains get larger and reach a critical size more than one dislocation slip system can become active at the same time. No longer only one dislocation at a time can be supported by the grain. Dislocation - dislocation interactions become possible. Thus, strain or work hardening of these supercritically sized grains becomes a possibility. From this study no quantitative estimates of the critical size can be determined. From Figure 72 and Figure 73 it can be seen that the grains

larger than ~350nm already make up about 70% of the total volume. Hence, the observation of dislocation storage is not surprising for these ultra fine-grained size grains. In addition to the local misorientation analysis via nano-diffraction, misorientations were estimated from the study of moiré fringe contrast in two-beam TEM images. The misorientations determined from these were less than 5˚. The boundaries analyzed are low angle grain boundaries. Clustering of grains is continuing. Figure 70 shows that the grain size or volume population of this state in deformation is a transition state between the lower and the higher cold rolling thickness reduction deformed samples. Dislocation - dislocation interactions are already possible but clustering and coalescence via dislocation – GB interactions is still a dominant process.

Some grains analyzed in the 53% deformed NC Ni were several hundred nm in cross-sectional dimension, much larger than the larger grains seen in the undeformed and up to 16% deformed NC Ni. As mentioned above, between probably somewhere around 40% reduction the 100 pole figures start to develop characteristic features similar to heavily deformed coarse grained Ni. The 53% deformed sample shows elevated defect content. Strain is stored in form of dislocation arrays and tangles. This observation supports the conclusions drawn form the texture results. Like in the deformation of coarse grained Ni storage of strain due to dislocation - dislocation interactions is responsible for grain rotations resulting in the characteristic texture. Though small grains are still present (Figure 70 and Figure 71) Figure 72 and Figure 73 show that 70% percent of the total volume is made up by grains larger than ~280nm. As compared to the 34% deformed state further stress induced grain growth took place. Figure 73 also shows that the grain size population is more characteristic of a function that exhibits two or more peak-like maxima. Such a behavior distribution of grain sizes would be consistent with abnormal grain

growth by either a clustering mechanism or the migration of mobile high angle boundaries. It however does not favor uniform grain growth.

In the 75% deformed sample clear evidence of dislocation interactions were found. The grain size increased further. The diffraction pattern analysis showed that many grains have a <112> zone axis orientation consistent with the texture development. No evidence of mechanical or deformation twinning was found. In addition, regions of large elongated (Figure 63) grains very similar to what would be expected for coarse grained material was seen. Grains in front of the elongated grains are of very similar orientation as the elongated grains. A coalescence mechanism, which involves the annihilation of low angle grain boundaries, seems to be still active. However, a growth mechanism by the motion of mobile high angle grain boundaries cannot be excluded either. The grain size population analysis shows a prolongation of the trends observed in the 53% deformed sample.

In summary, the combined morphological and grain size population results show that deformation induced clustering of grains and subsequent coalescence, facilitated by dislocation – grain boundary interactions take place. This result is consistent with observations in the literature [43]. The coalescence by dislocation – GB interaction induced dissolution of low angle grain boundaries, especially after small amounts of plastic deformation, seems more likely than motion of high angle grain boundaries. A large number of clusters containing very similarly oriented grains have been observed to form prior to coalescence. Coalescence alone yields only minimal changes in macroscopic texture. Coinciding with a characteristic change in texture after about 40% reduction in thickness large amounts of stored strain in form of an elevated dislocation density has been observed. After a significant volume fraction associated with grains that have become of a size capable of supporting multiple dislocations at the same time, multiple slip and

concomitant dislocation – dislocation interactions occurred. Like in coarse grained metals and alloys dislocation mediated plasticity seems to be responsible for the characteristic change in texture observed after about 40% or larger reduction in thickness by cold rolling for the NC Ni. Similar to coarse grained metals elongated grains form upon large amounts of plastic deformation. Large amounts of deformation induced twinning activities were not observed. Thus, it is the interplay of plastic deformation by dislocation glide with the existing GBs in the NC Ni, which results in changes of the GB structures, formation of clusters of grains separated by LAGBs. Upon further deformation LABGs are increasingly annihilated, presumably by incorporation of additional glide dislocations and dislocation reactions between glide dislocations grain boundary dislocations, i.e. dynamic dislocation and GB structure changes during deformation. This results in the apparent abnormal grain growth and establishment of a majority volume fraction of the material to be comprised of elongated grains that are sufficiently large to support multiple slip system dislocation glide activity, allowing for dislocation interactions leading to work hardening and strain storage in the form of defect arrays and tangles. Thus, large cold work deformation may be a suitable process to establish NC or UFG Ni with a multi- or bi-modal grain size distribution, a composite-like microstructure comprised of very hard NC grains and larger UFG grains. It can be hypothesized that the NC grains would provide for a high yield stress and the UFG grain, which have access to a work hardening mechanism, would provide ductility and elevated toughness to the material by preventing 'localization' of the deformation process and shear softening, which typically has been associated with the small failure strains for NC metals.

4.3 HARDNESS MEASUREMENTS

The hardness measurements in Figure 75 shows very similar results as the FWHM change in the XRD results section (Figure 21). Within the error bar the hardness does not change at all during the increased deformation by cold rolling. This might lead to the conclusion that no work hardening took place. However, previous analysis of this work already showed that the average grain size changes (Figure 71).

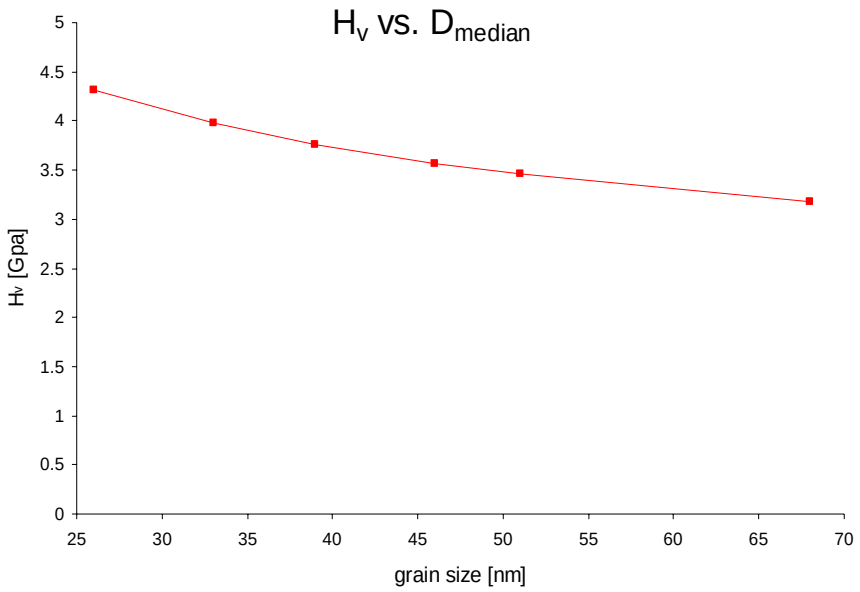

Figure 80. Change in Vickers hardness due to a change in median grain size Dm from 26 to 68nm using data from [40]

That change in average grain size should lead to a change in hardness since the NC Ni studied here resides in the grain size regime where a positive Hall-Petch effect on hardness is expected. Zhang et al. measured a decrease in hardness in NC Cu upon grain growth experimentally [44], [45] which has been theoretically confirmed by Zhu et al. [46].

The H_v versus grain size plot has been obtained theoretically using the experimentally measured median grain sizes and using the equation below with literature data for H_{v0} of 1.33GPa and a K = 15.2Gpa(nm)$^{1/2}$ [47]

$$H_v = H_{v0} + K\frac{1}{\sqrt{D}} \qquad \text{Equation 15}$$

(H_v = Vickers hardness, H_{v0} and K are constants; D is average grain size). Similar to the XRD analysis, it was assumed in the following theoretical considerations and estimate, that an increase in dislocation density, i.e., dislocation facilitated work hardening, entirely compensates the theoretically expected reduction in hardness due to the increase in median grain size for increasing cold rolling deformation of the NC Ni. Assuming a Taylor model and that the NC Ni was essentially dislocation free to start with, we can use the difference in theoretically predicted hardness for the different grain sizes observed to estimate a dislocation density. Using equation 12 and the constants ($\alpha \sim 0.2$, μ_{Ni} = 76GPa, b = 0.25nm), the dislocation density is

$$\rho = 6 \cdot 10^{12} cm^{-2}$$

This result is about one order of magnitude higher than the estimate for the dislocation density obtained from the XRD analysis. Given the level of uncertainty in some of the assumptions these estimates are based on, it can be argued that they are essentially the same. In a coarse grained material these densities correspond to heavily deformed microstructures and most importantly are not unreasonable for metals. A density of ~10^{11}-10^{12} dislocations/cm^2 corresponds to 10-100 x 100nm dislocation line length in a 100nm sized grain. This translates into 1-10 dislocation

every 10nm. Using the correlation shown in Figure 79 to estimate the misorientation angle of a small angle grain boundary

$$D = \frac{b}{\theta}$$ Equation 16

(D = spacing between dislocations, b = Burgers vector, q = misorientation angle) the misorientation angle for an array of edge dislocations in Ni separated by 1-10 nm can be estimated as

$$\theta \sim 1.4^{\circ}\text{-}14^{\circ}$$

This result seems reasonable considering that low angle grain boundaries can have misorientations up to 16˚. In addition, moiré fringe analysis of some of the experimental TEM observations in the significantly cold rolling deformed NC Ni yielded angles on the order of 2˚ to 6˚, i.e. comparable to this result.

The combination of hardness measurements with grain size population analysis, morphology observations and XRD analysis are consistent with the conclusion that an increase in hardness due to work hardening is apparently compensated for by an increase in grain size. The crude theoretical considerations presented here and using a very simple model indicate that work hardening facilitated by dislocation interactions and storage is reasonable for the heavily cold rolled NC Ni. Without over interpreting the simple theoretical considerations, it is clear that the lack of observing the reduction in hardness due to grain size effects translates into reasonable dislocation densities, which have been observed for heavily deformed metals. The dislocation

estimate resulting from the hardness measurement is essentially the same as the result from the XRD analysis.

Hence, it seems reasonable to attribute the constant hardness observed for the NC Ni of different grain sizes after different amounts of cold rolling thickness reduction to a compensating effect from an increase in deformation induced dislocation storage and work hardening. It appears that the XRD, TEM and hardness data obtained during this study provide evidence for the ability of work hardening in NC Ni under cold rolling constraint.

5.0 SUMMARY AND CONCLUSIONS

Nano crystalline nickel has been cold rolled to small, intermediate and large strains. Microstructures of undeformed NC Ni and several deformed states have been analyzed by XRD and TEM. Vickers hardness, texture, morphology changes and changes in grain size population have been measured and determined.

The undeformed NC Ni showed a strong cube fiber texture. Upon plastic deformation up to 16% reduction in thickness, clusters of grains with very similar orientation form. At lower strains mainly dislocation – grain boundary mediated plasticity takes place Deformation induced grain coalescence occurs, most likely facilitated by annihilation of low angle grain boundaries. These results are consistent with the literature. Grain size population analysis results clearly confirm grain growth. Up to cold rolling thickness reduction to about 16% essentially no texture change occurs. After a cold rolling reduction of thickness of 34% evidence of massive dislocation mediated plasticity is observed. Dislocation - dislocation interactions take place. Concomitantly texture changes similar to characteristic changes for coarse grained cold rolled Ni are seen. Dislocation - dislocation induced work hardening facilitates the characteristic texture change. The resulting texture is consistent with the operation of unit dislocations rather than twinning dislocations. TEM observations confirm that twinning as a plasticity facilitating mechanism does not play a role. The grain size population analysis is consistent with abnormal grain growth. Abnormally grown elongated grains were observed with the TEM. XRD and

hardness measurements are consistent. Simple estimates showed that the lack of change in XRD peak broadening due to work hardening can be compensated for by the observed grain growth. Hence the XRD and hardness measurements are consistent with dislocation mediated plasticity.

Stress induced grain reorientation and coalescence takes place. Upon the formation of a sufficient volume fraction of larger grains, deformation is mainly accommodated by dislocation mediated plasticity. The material behaves in many respects like a coarse grained metal upon plastic deformation beyond this point. It would be interesting to test this cold rolled material in tension to evaluate experimentally the possible beneficial effects of the microstructural changes we reported here on the combination of yield stress and elongation to failure, tensile work hardening rate and toughness.

In the undeformed NC Ni the grains are of a size that supports only one active dislocation glide system. Upon plastic deformation, like cold rolling as presented in this study, single dislocations glide can be emitted from grain boundaries glide through the grain and get absorbed on the opposite side. The grain boundaries act as dislocation sources and sinks. This interaction of grain boundaries with dislocations lead to a grain reorientations i.e. a texture change and changes in grain boundary structure and character. High angle grain boundaries turn into low angle grain boundaries thereby lowering the overall energy of the system. The misorientation of grains is reduced, grains from grain clusters, induced by the externally applied stress. Ongoing dislocation – grain boundary especially low angle grain boundary interactions leads eventually to the dissolution of the low angle boundary, grains coalesce. However, only minor changes in texture are observable, up to this point, possibly due to the strong cube fiber texture in the undeformed state. Only minor changes in orientation are necessary to form grain clusters. Summing up, consistent with the literature stress induced grain clustering and subsequent

coalescence via dislocation - grain boundary interactions takes place. Evidence for an alternative mechanism based on the migration of mobile high angle grain boundaries has not been observed. However the occurrence of such a mechanism cannot be excluded.

With ongoing deformations grain growth facilitated via this coalescence mechanism continues. Once grains reach a certain size more than one dislocation glide system can simultaneously be active. Dislocation – dislocation interactions become possible. Similar to plastic deformation behavior of coarse grained Ni dislocation based work hardening takes place. Not only do these dislocation – dislocation interactions allow storage of strain in the microstructure but they are also responsible for major changes in texture.

In summary NC Ni with a starting grain size that can only support one active dislocation glide system at a time seems to undergo two phases during plastic deformation. In the first phase at low to intermediate strains mainly dislocation grain boundary interactions lead to grain rearrangements, the formation of grain clusters and eventually grain coalescence. Dislocation – grain boundary interactions facilitate plastic deformation. This behavior is very different from plastic deformation in coarse grained materials.

Once grains are able to support more than one dislocation glide system at a given time, phase two, dislocation – dislocation interactions become possible. Dislocation – dislocation interactions lead to texture changes and work hardening similar to plastic deformation in coarse grained metals at intermediate to high strains.

6.0 FUTURE WORK

In difference to coarse grained metals dislocation – grain boundary interactions play an important role during plastic deformation in NC Ni and especially for large deformation strains as realized here by cold-rolling. Hence it is important to characterize the character and energetics of grain boundaries not only in the undeformed state but also upon increasing amounts of plastic deformation. This study showed qualitatively that the grain boundary character changes from HAGB to LAGB character. However we did not statistically show whether the grain boundaries initially are equilibrated or not. In the discussion of the undeformed NC Ni only qualitative evidence of an unequilibrated boundary segment has been shown. These unequilibrated steps might act as grain boundary based dislocation sources. Hence, an elevated concentration of those steps, i.e. unequilibrated boundaries, might assist plastic deformation in NC Ni. In other words, we have to ask the question of whether unequilibrated boundary segments preferentially act as source sites? Would unequilibrated boundaries therefore be beneficial to accommodate plastic deformation, increase ductility? On the other hand, from a technological point of view, unequilibrated boundaries will make the microstructure certainly less stable thermodynamically.

What happens to such a grain boundary dislocation source after the emission of a dislocation? Does the boundary segment equilibrate and the step disappears, the source vanishes or not? If the source concentration decreases because grain boundaries equilibrate plastic deformation might become harder. To be sure significant hardening has not been observed. On

the contrary the hardness remained constant. The concentration of other sources like triple junctions at boundaries might be high enough to accommodate this change in available dislocation source concentration.

It has become clear that the determination of not only the change in grain boundary character but also the change in grain boundary structure on an atomic level as indicated in figure 75 will be necessary to answer some of these questions. HREM will be available as a tool in the future to conduct experimental study of the grain boundary structures as a function of processing state in NC Ni.

Simple first order approximations showed that the lack of change in hardness and XRD peak broadening for increasing cold-rolling deformation can be rationalized on the basis of grain growth and simultaneous storage of cold-deformation strain in the microstructure. TEM results are qualitatively consistent with this proposition. An easy way to prove this assumption would be to subject the 75% deformed NC Ni to a short heat treatment. Grain coarsening could be measured and the contribution in hardness estimated as before. If indeed strain has been stored in the microstructure, as all the measurements so far indicate, the drop in hardness should be larger than estimated from the grain growth effect.

In general heat treatments via DSC could potentially yield information on the stability of undeformed and deformed NC Ni. However care has to be taken when analyzing DSC measurement as the thermal signature integrates over all possible thermally activated relaxation processes. Concomitant careful studies of changes in the microstructure are required to identify possible relaxation processes.

Another boundary and stability related aspect stems from the fact that for this study electrodeposited NC Ni has been used. Metals that have been processed via electrodeposition are

known to contain high concentrations of typically interstitial solutes present in the electrolyte solutions (e.g. S in ed-Ni). At low temperatures these solutes usually segregate to grain boundaries for entropic reasons. By decorating the grain boundaries they decrease the mobility of the boundaries. This might cause or at least enhance the development of the bimodal type population. From an applications point of view the bimodal microstructure might actually be advantageous. The large grains might allow work hardening providing ductility whereas the small grains improve strength. The challenge would be to find a way to evenly distribute larger grains among bigger grains. A first step in that direction would be to understand the role of the solutes. High spatial resolution analytical TEM will allow to analyze segregation levels in the undeformed state and the change thereof during plastic deformation. One reason for the coalescence to be mainly facilitated via dislocation – GB interactions rather than a sweeping motion of mobile high angle boundaries could be that most high angle boundaries are immobilized. To meet the challenge to create even distributions, it could be tried to selectively mobilize GBs, via strategic materials engineering.

Summarizing the objectives for future work, chemical and structural characterization on an almost atomic level of grain boundaries and the changes thereof during plastic deformation via analytical TEM and HREM will lead to the next level of understanding of the role of GBs during plastic deformation. Thermal heat treatments will confirm the storage of plastic deformation in the microstructure. Thermal and microstructural analysis during thermo mechanical processing will allow conclusions on the stability of NC metals in the undeformed as well as the deformed state.

APPENDIX A

NANOCRYSTALLINE METALS AND ALLOYS BY PULSED LASER DEPOSITION

A.1 INFLUENCE OF PROCESSING PARAMETERS ON MICROSTRUCTURE IN PULSED LASER DEPOSITED AU THIN FILMS

Appendix subsection Andreas K. Kulovits, John P. Leonard, Jörg M.K. Wiezorek

University of Pittsburgh, Pittsburgh PA 15261

A.1.1 ABSTRACT

It has long been recognized that thin film polycrystalline microstructures are determined by the thermodynamics and kinetics associated with physical vapor deposition, but it is quite process dependent and not easily quantified. We have examined the microstructure in polycrystalline Au films obtained by pulse laser deposition (PLD) under various conditions and interpret the results in terms of three fundamental parameters common to all physical vapor deposition: Flux kinetic energy, substrate temperature, and deposition rate. With this model, it is predicted that nanocrystalline films are formed in the limits of low temperature, flux, and high

deposition rate. The deposited films are analyzed with X-ray diffraction and SEM to determine texture and grain morphology, which are found to fit well within the process maps.

A.1.2 INTRODUCTION

Physical vapor deposition (PVD) of pure gold on SiO_2 is an ideal system for exploring kinetic and thermodynamic processes underlying microstructure formation. Pure gold is non-reactive in most atmospheres, and is particularly difficult to oxidize. Amorphous SiO_2 is easily prepared as a substrate using thermal oxidation of standard silicon wafers, resulting in a high purity, very smooth surface without crystalline order that would affect orientation selection in the early stages of film growth. It is possible that nanocrystalline Au films on SiO_2 may provide an ideal system for mechanical measurements such as nanoindentation or compression.

A.1.3 RESULTS

Gold films have been deposited by pulsed laser deposition (PLD) on SiO_2 substrates under different deposition conditions. A polycrystalline gold target of 99.999% purity was ablated with 248nm KrF excimer laser irradiation at 25 ns FWHM, 10 Hz, target rotation, a spot size approximately 1 x 3 mm, and fluence 8.37 to 9.56 J/cm^2. A high vacuum chamber with base pressure 1 x 10^{-7} Torr was backfilled with high purity Argon gas, and distance between the target and the substrate was 58 mm. Background pressure and the substrate temperature were varied for each deposition. The deposition rates were from 3.3A/s (room temperature deposition with no

background gas) 4.4 A/s (room temperature deposition with a background gas pressure of 500mtorr) and 3.6A/s (220˚C and 500mtorr). Figure 81 shows overview backscatter electron SEM and BSE images of the different resulting microstructures obtained under these deposition conditions. The film that has been deposited at room temperature with no background gas pressure is continuous. Grains with an apparent size on the order of 150 – 200 nm can be seen as well as grains that appear to be almost an order of magnitude smaller. It seems that the grain size distribution of this film is somewhat bimodal. The film that has been deposited at room temperature using Ar gas at a pressure of 500 mTorr is discontinuous and fissured, with grain size on the order of a few nanometers. The film that has been deposited at elevated temperature with a background pressure is continuous. The results of X-ray analysis can be seen in Figure 82b. The 111 and 200 pole figure of the low temperature, vacuum deposited film show that almost all 111 planes are parallel to the film surface whereas the orientations of the 200 planes are randomly distributed in a ring shape at an angle of 54.7º. This is the typical signature of a 111 fiber texture. In the film that has been deposited at temperature with a background gas the sharp intensities seem to become more spread out, consistent with a more randomized texture. Additionally, θ/2θ scans were measured in a symmetric Bragg Brentano setup in Figure 82a. Very strong 111 and 222 Au peaks are present for the sample that was deposited at room temperature without any background gas. This is indicates that most of the 111 planes are parallel to the film surface, hence the possible presence of a 111 fiber texture.

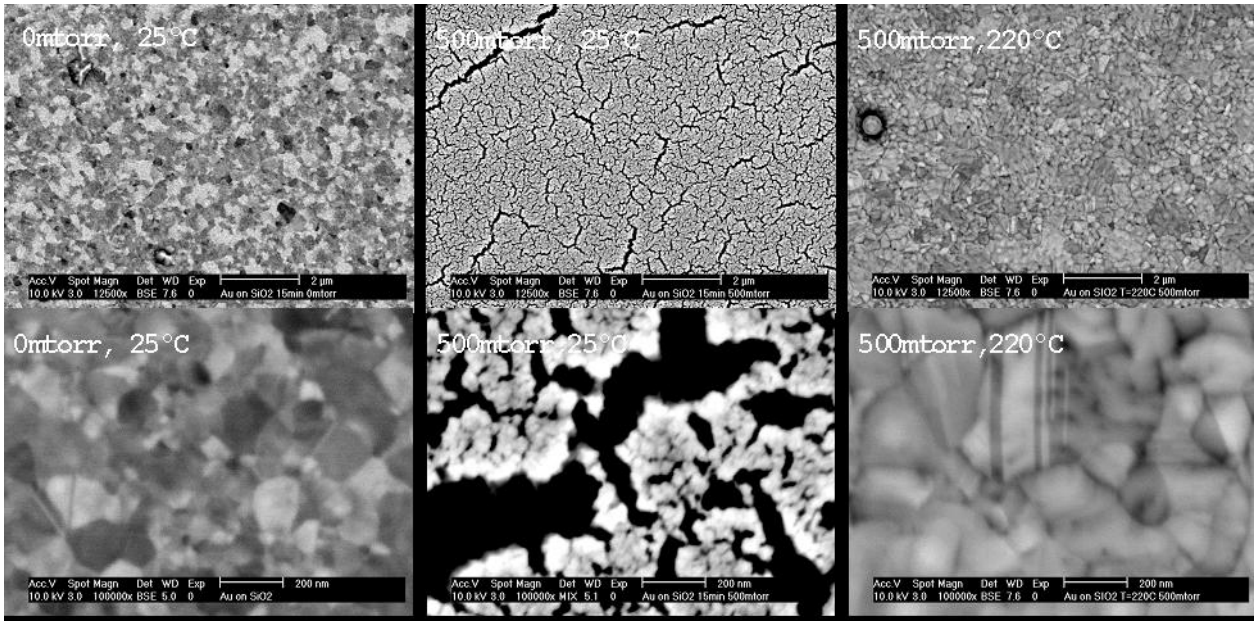

Figure 81. Backscatter SEM or BSE micrographs of Au on SiO2 thin films deposited using different background gas pressures and different substrate temperatures, scale bar is 2um (top row), 200nm (bottom row)

A similar scan on the sample that was deposited at room temperature and 500 mTorr Ar background gas pressure, shows the emergence of a 200 Au reflection, indicating a possible weakening of any present texture. It should be noted however that the film in this case has a fissure network so that it is partially discontinuous, as seen in the SEM images of Figure 81.

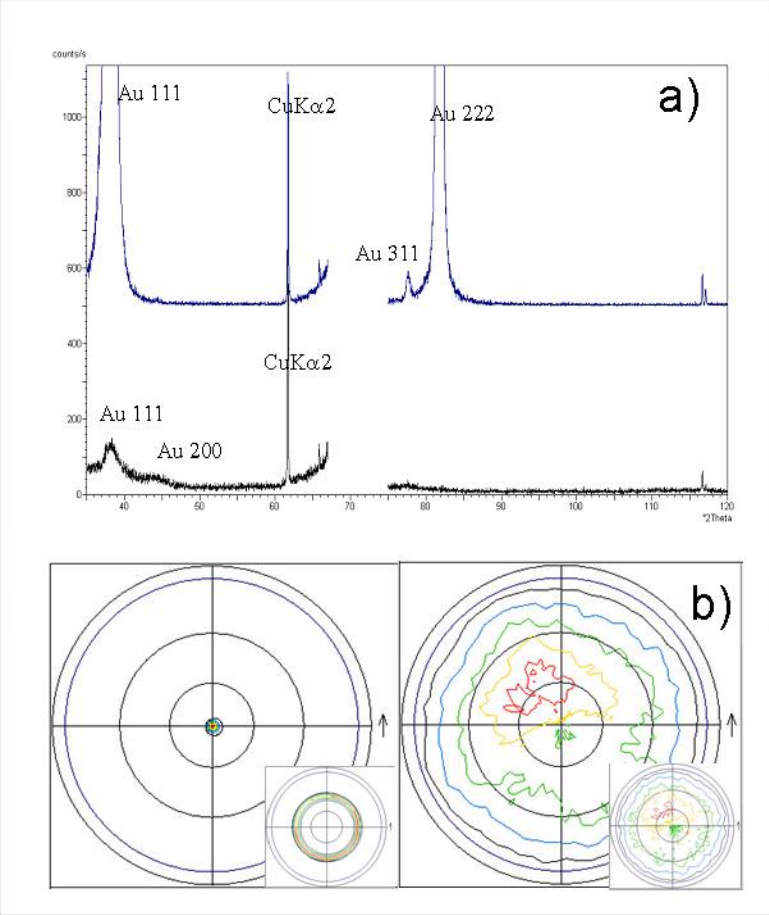

Figure 82. a) θ/2θ symmetric Bragg Brentano XRD scans, deposited at room temperature, 0 mTorr (upper), and at 500 mTorr (lower); b) 111 pole figures measured by XRD (with inset 200 pole figures) for 0 mTorr background gas (left), room temperature with 500 mTorr background (right). The highest intensities are about a factor of 5 larger than random.

A.1.4 DISCUSSION

A comprehensive survey of the literature finds over 25 papers since 1966 that specifically have investigated microstructure in PVD of Au thin films on SiO_2 (or glass). The results are remarkably consistent over the decades. This is in contrast to epitaxial systems where control of trace contaminants or surface structure [48] is difficult, but can improve with newer experimental techniques. Also, in systems of reactive materials, variability in chamber pressure and

cleanliness make comparisons to the literature difficult. Deposition of compounds is also often highly variable when stoichiometry cannot be easily controlled.

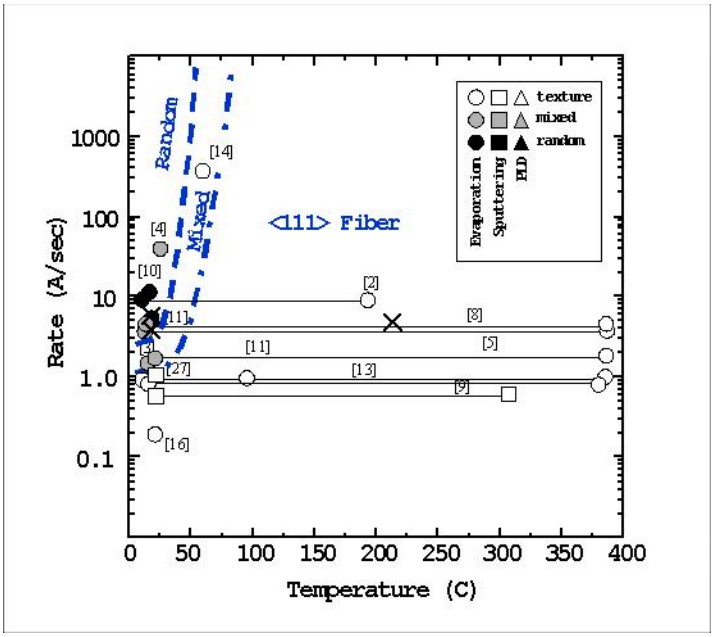

Figure 83. Microstructure map for physical vapor deposition of gold on SiO2 for various deposition rates and substrate temperatures. Current experimental conditions are shown as crosses.

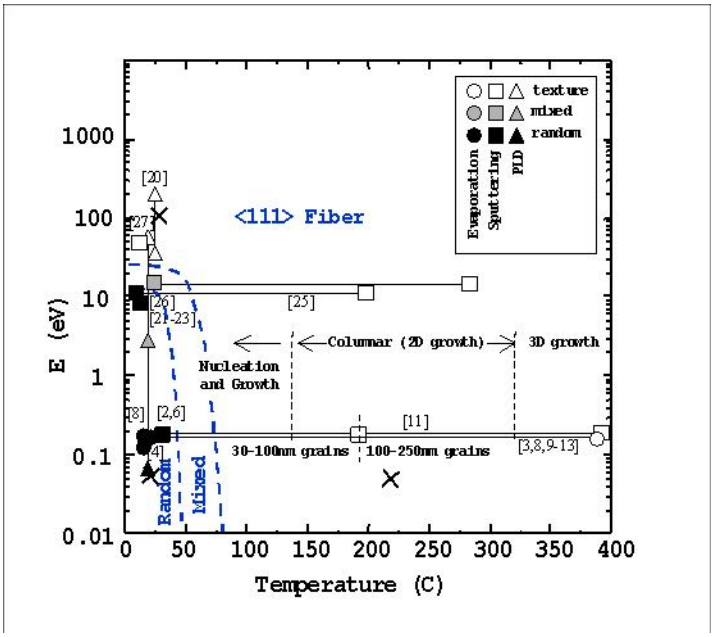

Figure 84. Microstructure map for physical vapor deposition of gold on SiO2 for various flux energies and substrate temperatures. Current experimental conditions are shown as crosses.

Thin films of pure gold on amorphous SiO_2 have been prepared under a wide variety of process conditions using evaporation [49-67], sputtering [49, 60, 68-71], or pulsed laser deposition (PLD) [72-75]. The various microstructures obtained have frequently been interpreted in terms of the kinetics and thermodynamics of the specific deposition process. Although a number of reviews [76], [77] with zone models for deposition of polycrystalline film evolution have now emerged, to our knowledge a comprehensive survey and unified model for PVD in the Au/SiO_2 system has not been attempted.

We postulate that there are three fundamental parameters governing the microstructure in PVD of Au on SiO_2: 1) Substrate temperature, 2) Flux energy, and 3) Deposition rate. This model is applied in the process-microstructure maps of Figure 83 and Figure 84, and easily unifies each of the three deposition techniques:

Evaporation. Evaporation is the simplest physical vapor deposition technique, involving an atomic flux from a liquid source in proximity to the substrate. Flux energy is typically small,

on the order of kT_m (0.115 eV) for gold. The geometry of the flux distribution is well known and deposition rates can be varied by changes in the substrate temperature, distance, or source.

Sputtering. Sputter deposition involves the bombardment of a target by ions accelerated in an inert gas plasma such as Ar. The ion-target collision process, typically involving energies of hundreds of eV, results in the ejection (sputtering) of atoms from the target material. These atomic species can be neutral or ionized, and their interaction with the plasma involves complex interactions and energy exchange. A wide variety of sputtering techniques including DC and RF discharge, magnetron, and ion beam sputtering have been developed [79], each with specific characteristics regarding bombardment energies, plasma density, and ionization processes. During deposition, the arriving flux typically contains ions and neutrals, distributed over a range of energies. As such, the energy distribution of the incident flux is coupled to the deposition rate and not directly adjustable. Only in the case of ion-beam sputtering, which does not involve a plasma, can the energy distribution of the flux be independently controlled.

Pulsed laser deposition (PLD). Utilizing a focused laser beam to generate a plasma flux, this is an easily adjustable technique [79] to obtain a wide range of microstructures, from high-quality epitaxial films to highly non-equilibrium nanocrystalline morphologies. Much like ion beam sputtering, energetic neutral and ionized atomic species are ejected from the target.

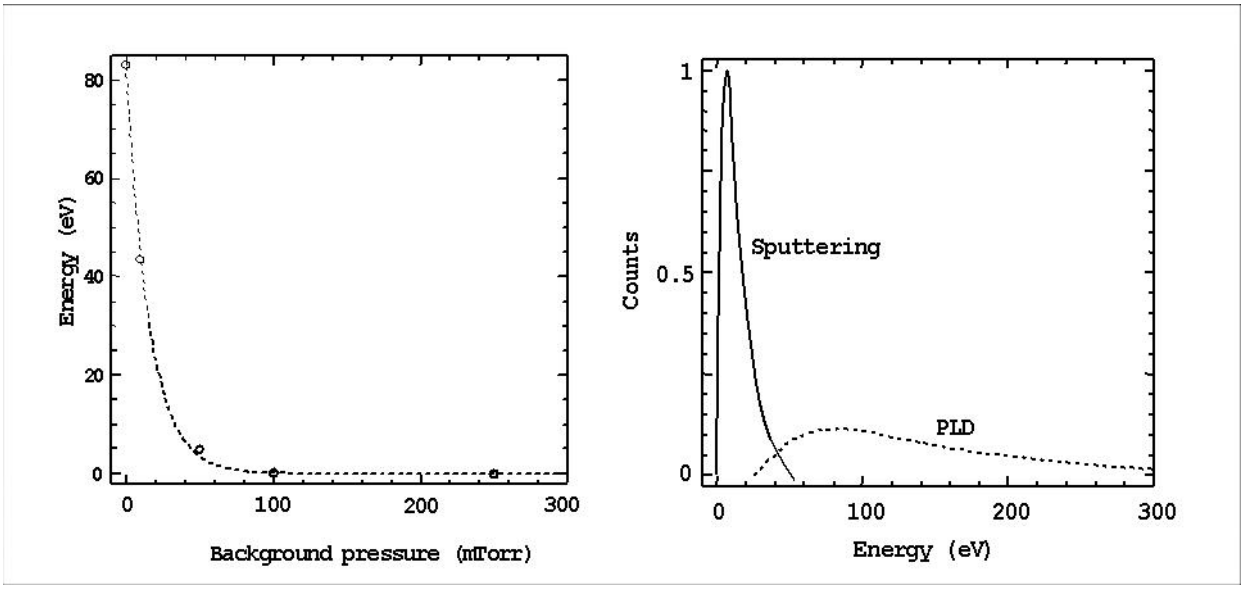

Figure 85. a) Typical energy distributions in deposition flux for DC sputtering Au (solid line) and vacuum pulsed laser ablation of Cu, adapted from [30,31]. b) Mean energy of flux in PLD plume arriving at substrate positioned 40 mm from the target, adapted from [26].

Coupled thermal, mechanical, and plasma hydrodynamic processes result in a localized plume with an energy distribution dependent on the laser fluence, thermophysical properties of the target material, and to a lesser extent the size and uniformity of the irradiated spot. A typical energy distribution is given in Figure 85b. The addition of an inert background gas, such as Ar, to the deposition chamber provides a low temperature bath into which the hot plasma can be quenched. It has been shown [75] that background pressures on the order of 100mTorr can effectively quench out the kinetic energy, leaving a concentrated pulse of high density flux at energies equivalent to that of thermal evaporation.

A.1.5 CONCLUSSIONS

The current experimental results for deposition of using PLD fit well into universal process-microstructure maps that have been compiled for polycrystalline Au on amorphous SiO_2. The three parameters and their influences are easily understood with simple arguments:

Substrate temperature. Surface diffusion is the primary transport mechanism governing film evolution during deposition. In Au, strong <111> texture and columnar growth is found for any substrate temperatures above 50C. This is due to the lower energy of the close-packed <111> surface of FCC metals, favoring nucleation [77] and growth of grains with this orientation. Only at the lowest temperatures is this effect suppressed.

Energetic flux. An energetic flux has been shown to lead to enhanced surface diffusion at low substrate temperatures, or implantation damage that can affect surface nucleation. In the map of Figure 84, there is a clear transition from random nanocrystalline to textured <111> material at a flux energy of 10 eV.

Deposition rate This affects adsorbed monomer densities, and island nucleation rates, and the timescale associated with burying surface features. Generally, higher rates lead to more non-equilibrium films [77]. In PLD, the deposition consists of microsecond pulses separated by long (msec) times without flux. Some systems may be affected by this and yield different microstructures relative to sputtering, but this does not appear to be the case with Au/SiO_2.

A.2 MICROSTRUCTURAL EVOLUTION DURING POST DEPOSITION ANNEALING OF PULSED LASER DEPOSITED FE(X)PD(1-X) THIN FILMS

Andreas K. Kulovits, John P. Leonard, J.M.K. Wiezorek University of Pittsburg, Pittsburgh PA 15261

A.2.1 ABSTRACT

FePd belongs to a group of $L1_0$ - intermetallics with attractive uniaxial hard-ferromagnetic properties. In this study thin films of different composition Fe_XPd_{1-X}, X= 50, 60, were deposited by pulsed laser deposition (PLD) on amorphous SiO_2 and Si_3N_4. We characterized the microstructural evolution during the different order/disorder phase-transformations during post-deposition annealing relative to the as-deposited state in terms of morphology, grain size, texture and presence of short-range order using SEM, XRD and TEM. VSM measurements were used to monitor magnetic properties. Differences in these microstructural parameters are due to different ordering reactions FCC to $L1_0$ ordering and concomitant phase separation of α–Fe vs. FCC to $L1_0$ ordering upon heat treatment. The relationships of the different phase transformation products to properties are discussed.

A.2.2 INTRODUCTION

FePd belongs to the family of intermetallics with interesting magnetic properties that undergoes a FCC to $L1_0$ ordering transformation [80]. In contrast to FePt in the Fe-Pd system does not form a $L1_2$ ordered Fe_3Pd phase in the Fe rich part of the phase diagram but rather separates into α–Fe and $L1_0$ ordered FePd (Figure 86). A careful study of the Fe rich part of the FePd phase diagram shows that many different stable and even more metastable phase transformation modes are possible depending on the alloy composition as well as the heat treatment details. For example, thermo-elastic martensite forms upon quenching a $Fe_{34}Pd_{66}$ alloy from the FCC phase field to room temperature [81]. In order to optimize magnetic properties or to design other interesting properties and behaviors of these alloys the phase transformation behavior during processing has to be understood. For this reason numerous investigators have been studying these alloys in bulk as well as thin film form [82-84]. For thin film preparation usually some type of physical vapor deposition, e.g. magnetron sputtering, is used [85]. In this study pulsed laser deposition (PLD) has been used to obtain FePd thin films of the compositions $Fe_{50}Pd_{50}$ and $Fe_{60}Pd_{40}$. PLD utilizes a high-energy laser to irradiate a solid target material, producing a plasma that subsequently impacts a substrate producing a thin film. Ablation rates for different materials are typically very similar, resulting in high-fidelity transfer of the target composition to the deposited film. Thus, together with possible stoichiometric rates, the excellent compositional control for alloy and complex multi-element compound thin films is considered as the main advantage of PLD. Here the evolution of microstructures of PLD thin films of Fe_XPd_{1-X}, X= 50, 60, deposited at room temperature and elevated substrate temperature have been

compared and rationalized utilizing the FePd phase diagram. Furthermore, the microstructural evolution during subsequent annealing has been investigated and changes in magnetic properties have been monitored.

A.2.3 EXPERIMENTAL

$Fe_{50}Pd_{50}$ and $Fe_{60}Pd_{40}$ targets have been produced form high-purity elemental starting materials using vacuum arc melting in a purified Argon gas atmosphere. $Fe_{50}Pd_{50}$ and $Fe_{60}Pd_{40}$ thin films were produced by ablation with a 248nm KrF excimer laser irradiation at 25ns FWHM in a high vacuum chamber with a base pressure of $1.3\ 10^{-5}$ Pa. Films of both compositions were deposited on SiO_2 and Si_3N_4 substrates. In all depositions the spot size was approximately 1 x 3mm, the fluence 8.37 to 9.56J/cm^2, the laser pulse frequency 10Hz and the deposition rate about 2.3Å/s. The target to substrate distance was 58mm. The targets have been rotated during deposition. Films have been deposited for different times (60s and 600s) and using different substrate temperatures (300K and 494K). Post-deposition annealing has been performed in a controlled atmosphere/vacuum furnace for 1800s at 823K using pure Ta foil as sacrificial oxygen gettering agent to prevent any significant and detrimental oxidation of the uncapped Fe-Pd thin films. Compositions of the as deposited films were $Fe_{48.5\pm3.0}Pd_{51.5\pm3.0}$ and $Fe_{60.5\pm2.0}Pd_{39.5\pm2.0}$ as determined by X-ray energy dispersive spectroscopy in a transmission electron microscope (TEM) and were identical to those of the target materials. X-ray diffraction (XRD) was performed in symmetric Bragg Brentano setup using a Philips PW 1830 diffractometer with Cu-K_α radiation. A JEOL JEM2000FX operating at 200kV has been used for the TEM work. The magnetic properties have been measured with a Vibrating Sample Magnetometer (VSM)

performing M-H loops with a maximum applied field of 2T. Samples for TEM study have been obtained by directly depositing the intermetallic alloy films onto Si_3N_4 coated windowed Si TEM grids.

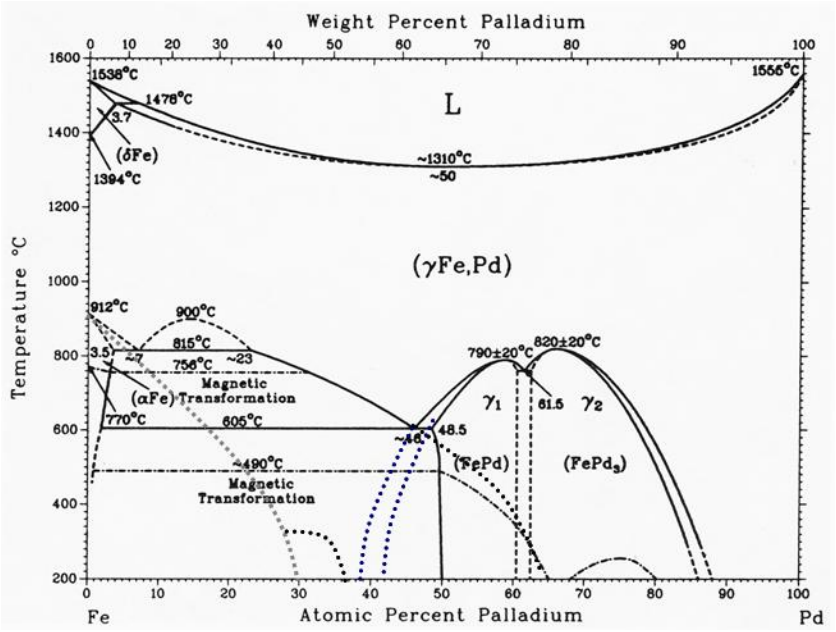

Figure 86. Binary FePd phase diagram including schematic extensions of metastable phase fields, marked in dotted lines

A.2.4 RESULTS

ROOM TEMPERATURE DEPOSITION (300K): $Fe_{50}Pd_{50}$ and $Fe_{60}Pd_{40}$ PLD films both exhibit very narrow grain size distributions after room temperature deposition onto the amorphous (SiO_2 and Si_3N_4) substrates (Figure 87). The largest grain diameters observed by dark field TEM were about 30nm. The average grain size determined from TEM dark field images using populations in excess of 200 grains for the $Fe_{50}Pd_{50}$ and $Fe_{60}Pd_{40}$ thin films is 7.4 ± 4.0nm, and 7.0 ± 3.0nm respectively. TEM selected area diffraction patterns exhibited a considerable diffuse background intensity associated with scattering from the amorphous Si_3N_4 substrates,

which prevented conclusive identification of possibly present weak intensities in $L1_0$ superlattice reflections near the transmitted beam (Figure 89). However, XRD scans clearly showed evidence of diffraction from a small volume fraction of $L1_0$ ordered phase in addition to FCC phase in the as-deposited films (Figure 88).

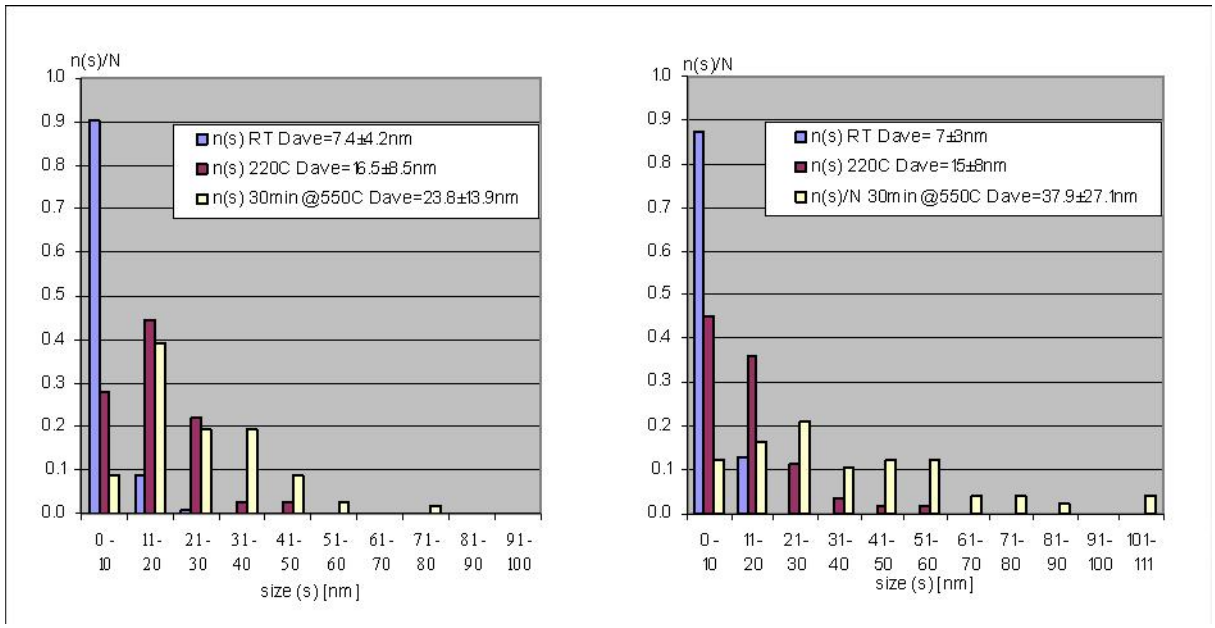

Figure 87. Effects of deposition temperature and post-deposition annealing on normalized grain size distribution n(s)/N with N the total number of grains of PLD Fe50Pd50 (on the left) and Fe60Pd40 (on the right) on Si3N4; deposited at 300K≈25˚C=RT, at 494K≈220ºC and deposited at 220˚C with subsequent annealing for 30min at 823K ~550˚C respectively.

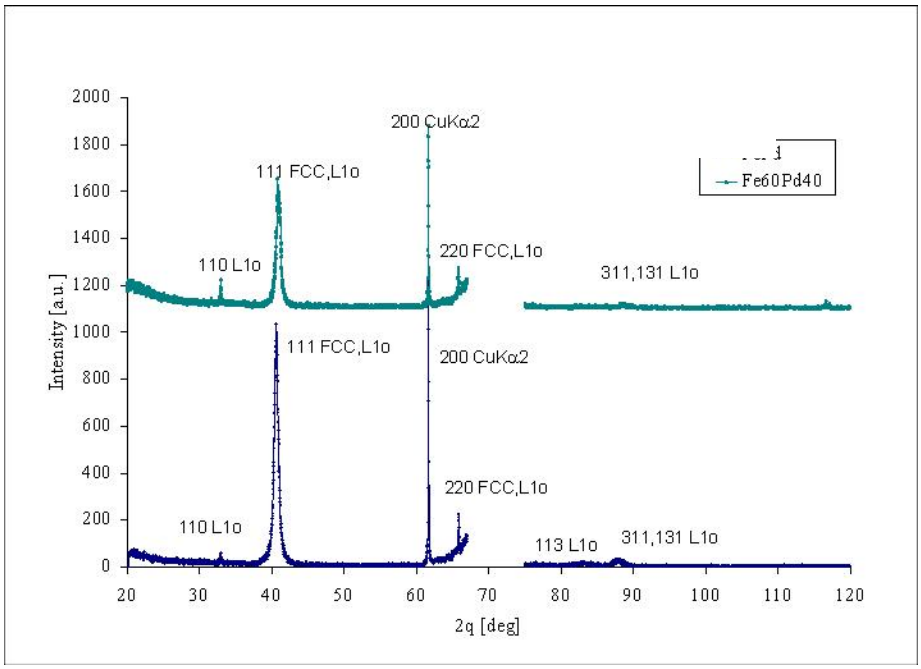

Figure 88. θ/2θ XRD scans of the PLD Fe50Pd50 (blue curve) and Fe60Pd40 (green curve) films on SiO2 (300K substrate temperature). The excessively intense Si peak at 69˚=2θ has been blocked.

ELEVATED TEMPERATURE DEPOSITION (≈494K): The $Fe_{50}Pd_{50}$ composition film shows an increase in average apparent grain size to 16.5 ± 8.5nm. i.e. by about 125% relative to room temperature film deposition. The normalized grain size distribution broadens (Figure 87). No significant change in the volume fraction of $L1_0$ ordered phase was determined using analyses of the corresponding diffraction patterns (Figure 88). The diffraction pattern of the Fe rich $Fe_{60}Pd_{40}$ film shows the emergence of α-Fe phase in addition to FCC and some small fraction of $L1_0$ phase, confirming previous reports [85]. The increase in substrate temperature during deposition by about 200K resulted in an increase in average grain size to 15 ± 8nm, again about a factor of two relative to the room temperature deposited film (Figure 87), and was accompanied by a broadening of the grain size distribution (Figure 87).

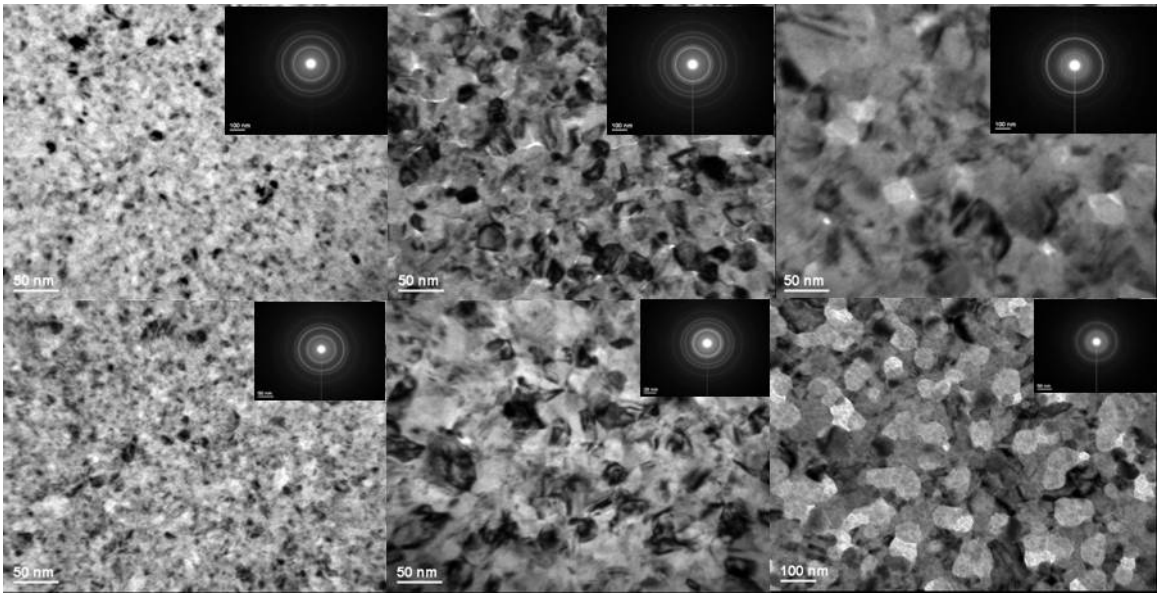

Figure 89. TEM bright field micrographs, inset selected area diffraction patterns; effects of deposition temperature and post-deposition annealing on microstructure of PLD Fe50Pd50 (top three images)and Fe60Pd40 (bottom three images) on Si3N4; left - deposited at 300K; middle - deposited at 494K; right - deposited at 494K with subsequent annealing for 30min at 823K, respectively.

POST-DEPOSITION ANNEALING: During annealing for 1800s at 823K the apparent average grain size changes to 23.9 ± 14.0nm in the $Fe_{50}Pd_{50}$ thin films. Grains up to ~ 90nm are observed. The grain size distribution broadens further but does not become bimodal (Figure 87). A significant amount of $L1_0$ ordered volume fraction developed during annealing, as indicated by superlattice reflections in the diffraction pattern (Figure 88), and resulted in an increase in coercivity from about 53 Oe for the as-deposited film to 837 Oe after annealing. Similarly, for the $Fe_{60}Pd_{40}$ thin films the apparent average grain size increased to 37.9 ± 27nm, with some grains larger than 100nm. The grain size distribution broadened more as compared to the distribution of the equiatomic films (Figure 87). Diffraction studies revealed the presence of α–Fe along with $L1_0$ ordered FePd. The coercivity increased from about 24 Oe to roughly 362 Oe after annealing, consistent with an increase in $L1_0$ ordered volume fraction.

A.2.5 DISCUSSION

The apparent average grain size of the room temperature deposited PLD Fe_xPd_{1-x} films for both compositions is about 7nm with relatively narrow size distributions, which is similar to reports of grain sizes and size distributions obtained for sputtered Fe-Pd thin films [82], [86].

In films of both compositions some small volume fraction of $L1_0$ ordered phase has been observed. This finding clearly indicates that even during room temperature depositions the kinetic energy of material in the plasma is sufficient to allow for some atomic mobility upon arrival on the substrate. This result is in contrast to reports for sputter deposited FePd thin films. Sputtered films contain typically just the high temperature FCC phase [82]. During deposition the temperature of the FePd solid film rapidly reaches that of the substrate (300K). Thus, the kinetic energy of the plasma which transforms into heat upon impact with the substrate, results in some limited surface diffusion leading to the formation of the metastable $L1_0$ ordered phase. For processes that involve long range grain boundary and bulk diffusion the transferred energy is insufficient. They are kinetically limited.

The absence of α–Fe phase in the Fe rich thin film deposited at room temperature can be in first approximation rationalized by consideration of the metastable extensions of the $\gamma/L1_0$ two phase field in the FePd bulk equilibrium phase diagram to lower temperatures and Fe-rich compositions (Figure 86). Thermodynamically the excess free energy can be lowered by precipitating some small volume fraction of presumably metastable ordered $L1_0$ phase and enriching the FCC matrix in Fe at the same time. This process might lead to a faster free energy release than phase separating into the equilibrium composition α–Fe and $L1_0$ ordered stoichiometric FePd. This reaction path is only possible if the metastable $\gamma/L1_0$ two phase field

seems accessible during room temperature PLD. The $Fe_{60}Pd_{40}$ composition has to lie within the metastable $\gamma/L1_0$ phase field at room temperature.

In contrast, for the Fe rich film deposited at 494K (~220°C), the elevated substrate temperature allows for sufficient long range grain boundary and bulk diffusional atomic rearrangements to facilitate some decomposition into the equilibrium α-Fe and $L1_0$-FePd phases during the deposition. Thus, the kinetic frustration is avoided. From a thermodynamic point of view the system can no longer access the metastable two phase field extension. The $Fe_{60}Pd_{40}$ composition has to be shifted above the $\gamma/L1_0$ field due to the moderately elevated substrate temperature (ΔT~200K).

The increased average grain size and broadened size distribution observed for both composition films deposited at elevated substrate temperature is consistent with the increased grain boundary and bulk diffusion during the elevated temperature deposition. Despite this enhanced surface diffusion, the resulting atomic mobility is still insufficient to allow for the phase transformation to complete in both composition films. As a result ordered volume fraction is only slightly increased relative to the room temperature (300K~$0.2T_m$) deposited films. Like in the room temperature deposited films the observed small fraction of $L1_0$ ordered material in the PLD Fe_xPd_{1-x} films can be still mostly attributed to effects of the kinetic energy of the ablated plasma as the energy contribution of the heated substrate is minor. This observation is consistent with 474K~$0.3T_m$ (T_m~1700K, Figure 86) thermodynamically being still a rather low homologous temperature. This speculative conclusion requires further evaluation by study of films deposited for systematically varied PLD processing parameters and is planned for the future.

At the isothermal annealing temperature, 823K~0.5T_m, atomic mobility is sufficient for the phase transformations to occur. The difference in coercivity, H_C, in the Fe rich and the equiatomic thin films can be attributed to the difference in volume fraction of fully ordered $L1_0$ FePd. Under equilibrium conditions the Fe rich films are expected to comprise about 20% volume fraction of α – Fe, reducing the total volume fraction of the magnetically hard $L1_0$ phase by about 20% relative to an equivalent molar mass of the equiatomic composition films. This is consistent with a lower coercivity as is observed here, namely 840 Oe for $Fe_{50}Pd_{50}$ versus 360 Oe $Fe_{60}Pd_{40}$.

A.2.6 CONCLUSIONS

Fe_xPd_{1-x} thin films have been successfully deposited using PLD. The compositions of the deposited films are the same as the targets. The grain size distributions are narrow with an apparent average grain size of about 7nm. The observed changes in microstructure upon changes in deposition temperature are consistent with inferences based on the equilibrium phase diagram of FePd. The change in magnetic properties during post-deposition annealing has been attributed to the formation of the $L1_0$ ordered FePd a magnetically hard phase.

A.3 MICROSTRUCTURE OF PULSED LASER DEPOSITED FEPD THIN FILMS ON AMORPHOUS AND CRYSTALLINE SUBSTRATES

A. Kulovits, J. Leonard, J. Wiezorek

Department of Mechanical Engineering and Materials Science

University of Pittsburgh

A.3.1 ABSTRACT

Equiatomic FePd thin films have been deposited at room temperature by pulsed laser deposition (PLD) on amorphous (Si_3N_4, SiO_2) and crystalline, (100)-NaCl, substrates and have been characterized by X-ray diffraction (XRD) and transmission electron microscopy (TEM). We observed a complex orientation relationship between grains in nanocrystalline thin films of FCC FePd and the single crystal NaCl substrates. FePd films obtained under identical deposition conditions using the amorphous substrates also exhibited nanocrystalline morphology but with a <111> fiber texture and consisted of a phase mixture of FCC FePd and the tetragonal ordered $L1_0$-FePd phase.

A.3.2 INTRODUCTION

The stable high temperature phase of equiatomic FePd is a FCC solid solution. Upon cooling below the order/disorder temperature FePd forms an $L1_0$ ordered intermetallic phase via a first order phase transformation. $L1_0$-FePd belongs to the family of ordered intermetallics like FePt, CoPt and MnAl that exhibit very promising uniaxial magnetic properties. The high magnetocrystalline anisotropy along with the large theoretical $(BxH)_{max}$ triggered consideration of these phases for potential use as perpendicular magnetic recording media. In bulk form they might be used as permanent magnets. Most of the important quantities like the coercivity or the energy product $(BxH)_{max}$ strongly depend on the microstructure. Hence, especially texture development, control of scale and development of long-range order during deposition and during post deposition processing have to be very well understood. For this reason numerous investigators have been studying these alloys in bulk as well as thin film form [87-89]. Compared to bulk FePd alloys texture control in thin films poses additional challenges. The elevated surface to bulk volume ratio in the film geometry and the interaction of ordering transformation stresses with the film surface may influence the texture development.

With the exception of one report [91], most prior studies used magnetron sputtering [91-96] or molecular beam epitaxy [97-100] for thin film deposition of FePd. In many of these studies the effect of deposition temperature on the volume fraction of $L1_0$-phase and its impact on the magnetic properties has been investigated [e.g. 97-100]. Furthermore, typically metallic, e.g. Pd, buffer layers have been used to affect epitaxial growth of the FePd [100]. Here, we report initial results of the study of the influence of substrate structure (amorphous or crystalline)

without the use of seed layers on microstructures of room temperature deposited FePd thin films using pulsed laser deposition (PLD). FePd films are deposited using identical deposition parameters on amorphous substrates (Si_3N_4 and SiO_2) and a crystalline substrate (single crystalline (100) oriented NaCl) and characterized by X-ray diffraction (XRD) and transmission electron microscopy (TEM). In the future we will use these films to investigate the influence of the different as-deposited states on the ordering phase transformations and morphological changes during post-deposition processing.

PLD utilizes a high-energy laser to irradiate a solid target material, producing a plasma plume that subsequently impacts a substrate producing a thin film. This ablation process typically provides congruent transfer, resulting in a film composition that is very close to that of the target. For PLD, critical processing parameters such as deposition rate, flux kinetic energy, and substrate temperature, can be controlled independently, allowing for very good microstructural control [101]. This is an advantage over other deposition techniques, where these parameters are interdependent and often cannot be directly or individually controlled. Hence, PLD offers some potentially advantageous characteristics for the low temperature synthesis of FePd thin films compared to other more commonly used deposition techniques and a systematic study of the PLD method in the context of preparation of thin films of uniaxial anisotropic ferromagnetic $L1_0$-phases appears warranted.

A.3.3 EXPERIMENTAL

Nominally equiatomic FePd targets have been produced from high-purity elemental starting materials using vacuum arc melting in a purified Argon gas atmosphere (reference). FePd thin films were produced by PLD with a 248nm KrF excimer laser irradiation pulsed at 25ns FWHM in a high vacuum chamber with a base pressure of 10^{-7} Torr. Films were deposited on amorphous SiO_2 and Si_3N_4 and crystalline NaCl substrates at room temperature. In all depositions the spot size was approximately 1 x 3mm, the fluence 8.3 to 9.6J/cm^2, the laser pulse frequency 10hz and the deposition rate about 2.3Å/s. The target to substrate distance was 58mm, with targets rotated during deposition. Deposition times for films on amorphous Si_3N_4 and crystalline NaCl were 60s and 900s for films on amorphous SiO_2. The approximate film thicknesses were 15nm for the 60s depositions and 210nm for the 900s depositions, measured with a stylus profilometer. Using X-ray energy dispersive spectroscopy (XEDS) in a TEM the thin film compositions were determined as $Fe_{48.5\pm3.0}Pd_{51.5\pm3.0}$ and within experimental error were consistent with those of the target materials, $Fe_{45.6\pm3.0}Pd_{54.4\pm3.0}$, determined by standardless XEDS using an SEM Philips XL30 FEG operating at 15kV. XRD was performed in symmetric Bragg-Brentano setup using a Philips PW 1830 diffractometer with Cu-Kα radiation. A JEOL JEM2000FX operating at 200kV has been used for the TEM work. The software suite Desktop Microscopist from Virtual Laboratories has been used for simulations of TEM diffraction patterns. For the thin films on amorphous substrates samples for TEM study have been obtained by directly depositing the intermetallic alloy films onto amorphous Si_3N_4 coated windowed Si TEM grids. For the thin films on crystalline NaCl substrates TEM samples were obtained using

Cu TEM grids glued onto the FePd films followed by subsequent dissolution of the NaCl substrates in deionized water.

A.3.4 RESULTS

TEM bright field images exhibited continuous FePd films with equiaxed grain morphology and nanocrystalline grain sizes (Figure 91a and Figure 93a). TEM dark field images (e.g. Figure 91b and Figure 93b) of populations of in excess of 200 grains have been used to determine grain sizes for the FePd thin films on amorphous Si_3N_4 and crystalline NaCl substrates.

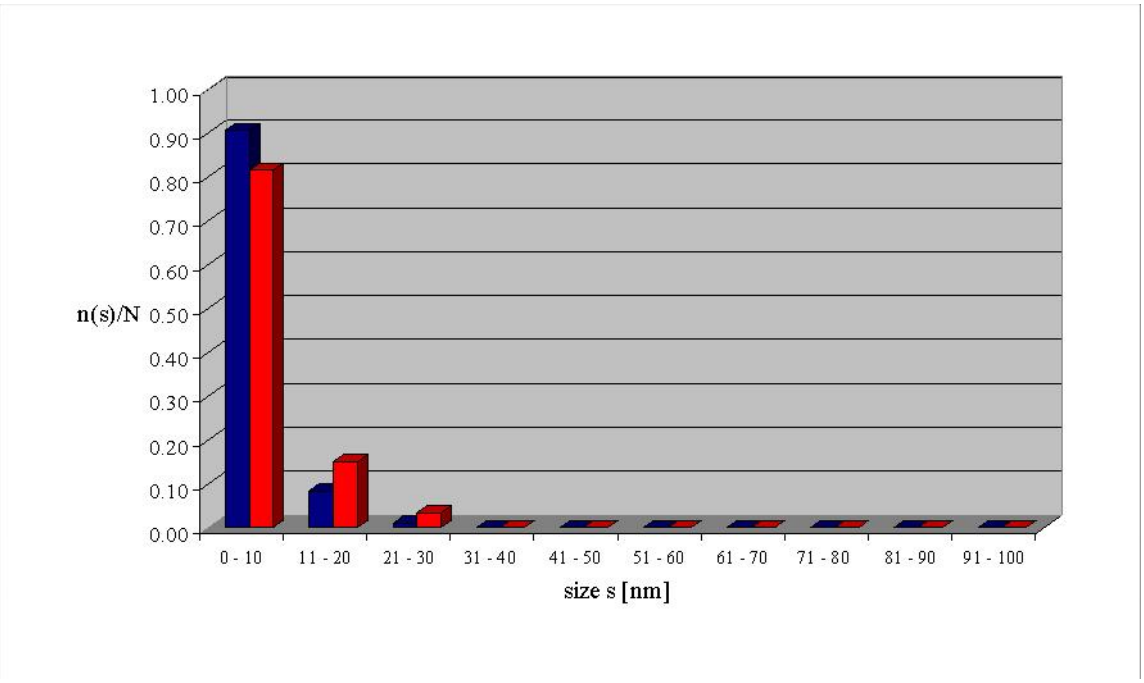

Figure 90. Grain size measurement results: Comparison of FePd on amorphous Si3N4 (blue) and (100)-NaCl (red) (number of grains normalized by the total number of measurements n(s)/N plotted vs. size regimes)

The results of the grain size analyses by dark field TEM are summarized in Figure 90. The geometric average of the grain sizes for FePd on Si_3N_4 was (7.4 ± 4.0) nm and for the FePd films on NaCl (10.4 ± 12.0) nm. The largest grain diameters observed by dark field TEM were about 30nm for the NaCl substrate (Figure 90, Figure 91, Figure 93).

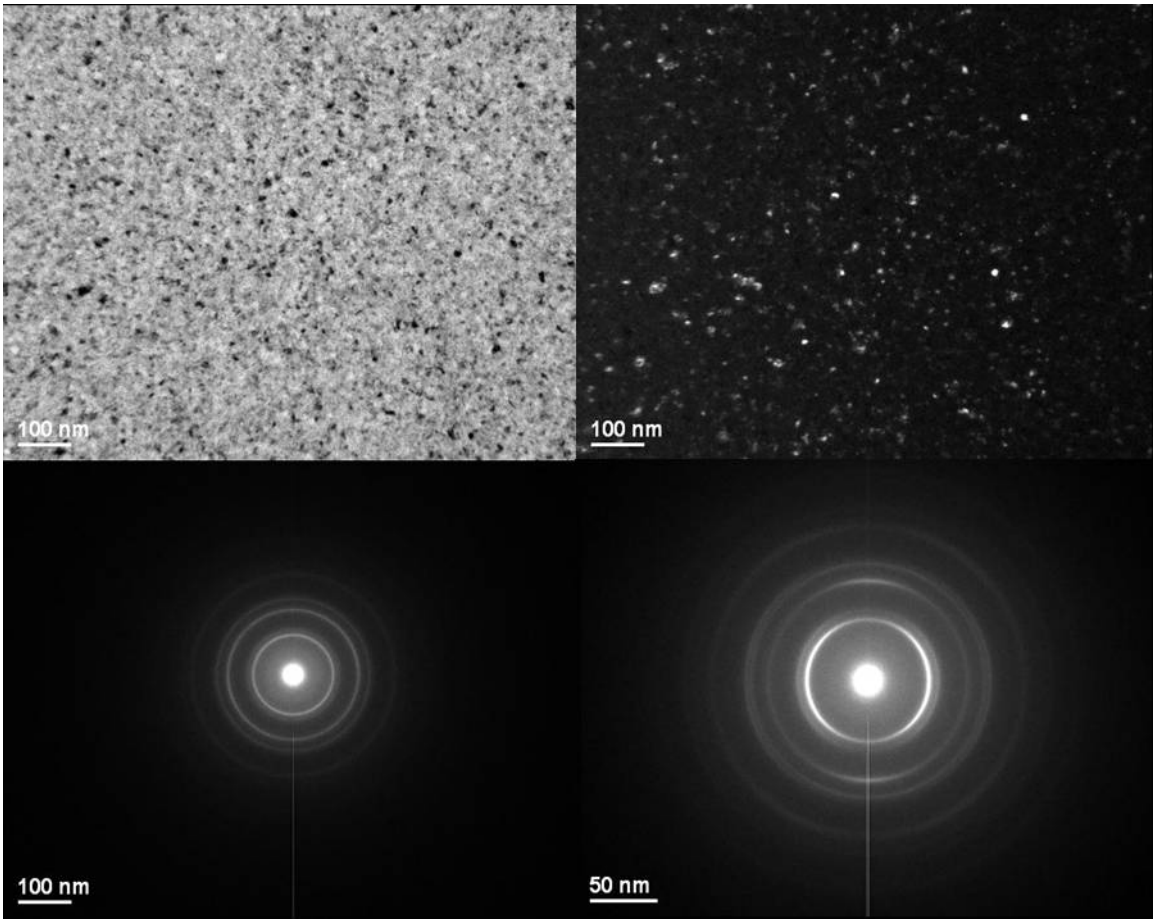

Figure 91. TEM of Fe50Pd50 thin films on Si3N4, a) Bright field, b) dark field and c) corresponding diffraction pattern for zero degrees of sample tilt and d) diffraction pattern for +10˚ of sample tilt; arching in the intensity of the SADP was symmetric for equal and opposite tilts about the two mutually perpendicular tilt-axis, thus indicating the presence of a fiber texture.

TEM selected area diffraction patterns (SADP) of the FePd films on Si_3N_4 exhibited considerable diffuse background intensity associated with incoherent scattering from the amorphous Si_3N_4 substrates. This prevented conclusive identification of possibly present weak

intensities associated with $L1_0$ superlattice reflections near the transmitted beam (Figure 91). However, XRD of FePd films on amorphous SiO_2 provides clear evidence for diffraction from a small volume fraction of $L1_0$ ordered phase in addition to FCC phase in the as-deposited films (Figure 92).

Tilting experiments in the TEM of FePd films on Si_3N_4 (Figure 91d) indicate the presence of a fiber texture with a fiber axis parallel to the thin film normal. The rings in the diffraction pattern of the tilted nanocrystalline specimen break up into discontinuous segments or arches, a characteristic observation if a fiber texture is present [102],[103].

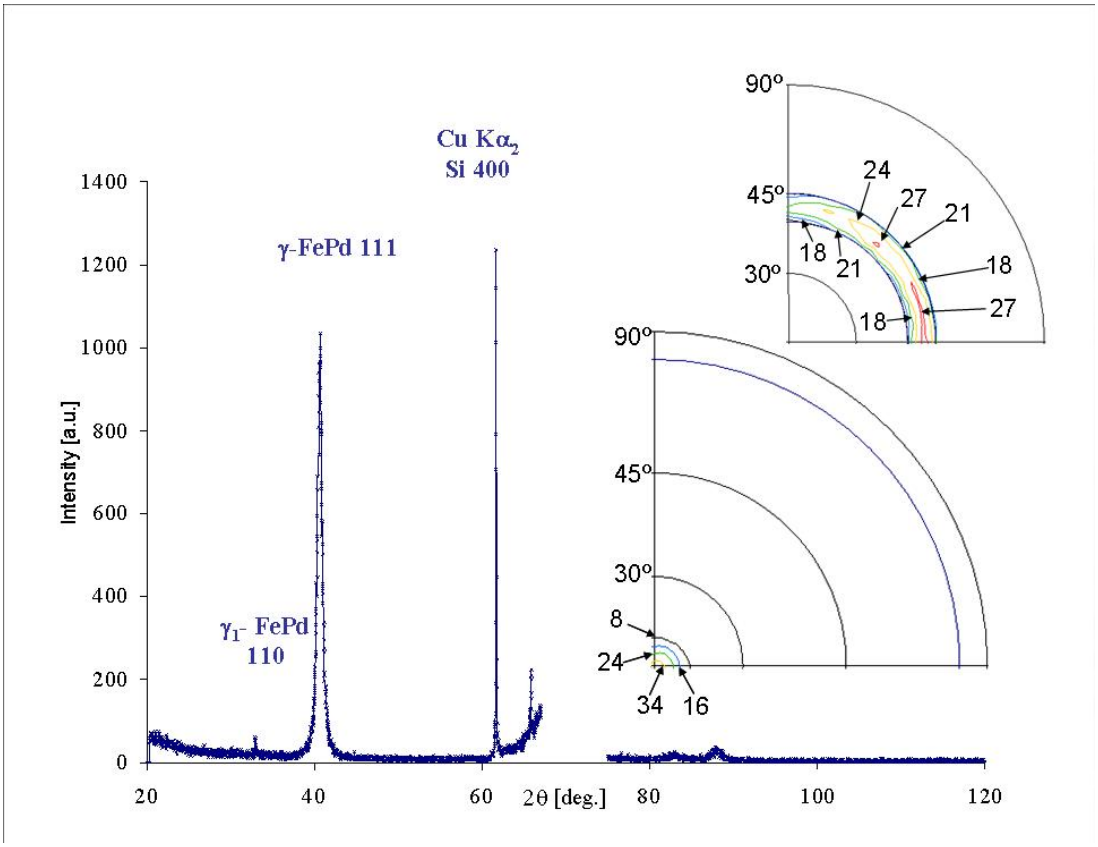

Figure 92. a) XRD symmetric Bragg-Bretano diffractogram (the strong substrate peak centered at 2θ=70.5˚, Si 400 is suppressed in this depiction), b) 111 and c) 200 as measured pole (small inset in the upper right corner) figures of FePd SiO2 (strong intensities {red} are about 8 times as large as weak intensities {black} in the case of the 111 pole figure and about 2.5 times as large in case of the 200 pole figure)

Furthermore, a 111-fiber texture was identified by XRD texture measurements for the FePd film on amorphous SiO_2 substrates (Figure 92b). While we have not determined the fiber axis for the FePd films on the amorphous Si_3N_4 substrates, the observation of a fiber texture in the latter by TEM (Figure 91) is consistent with the presence of the 111-fiber texture for the films on the SiO_2 substrates (Figure 92b). Furthermore, SEM backscatter electron (BSE) images (not shown for brevity) of FePd on amorphous SiO_2 exhibit similar microstructural morphology and scale as the films deposited on amorphous Si_3N_4.

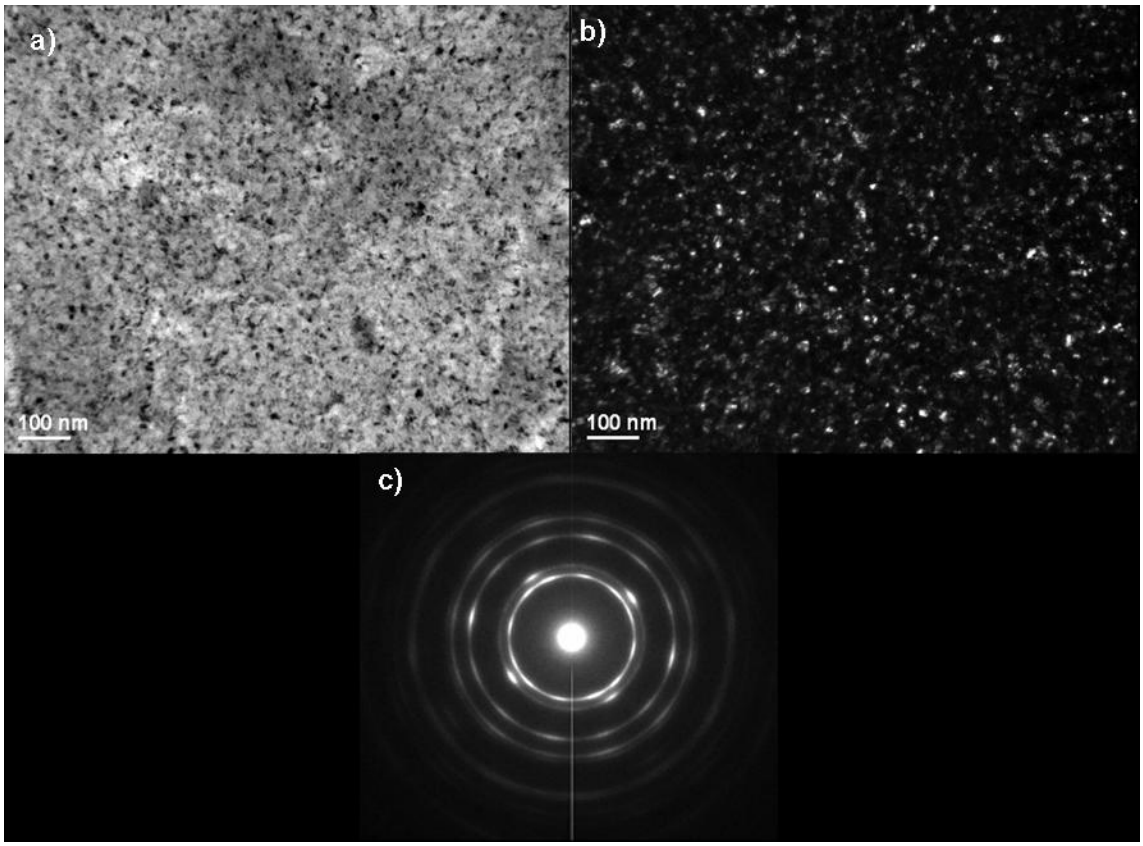

Figure 93. TEM of FePd on NaCl, a) Bright field, b) dark field and c) corresponding diffraction pattern.

Hence, while it is tempting to speculate that the FePd films on both amorphous substrates may exhibit 111-fiber textures, based on the data currently available we can only conclude that they exhibit similar grain morphology and scale with fiber textures.

For the FePd films on crystalline NaCl the scale of the grains was about twice as large but the morphology was similar to that of the microstructures of the films deposited on the amorphous substrates (Figure 91a, Figure 93a). Superlattice reflections have not been observed in the TEM diffraction experiments for the free-standing FePd films studied in the TEM after PLD on NaCl. Thus, unlike in the case of the FePd films deposited on the amorphous substrates, where ordering was observed by XRD (Figure 92), for the films on the NaCl substrates the FePd did not exhibit detectable ordering. However, the diffraction pattern of FePd on NaCl reveals significant differences in the film structures to those of FePd on amorphous Si_3N_4 (Figure 91c and Figure 93c). The nanocrystalline FePd films on the amorphous substrates (Figure 91, Figure 92) exhibited fiber textures with the fiber axes, presumably <111>, parallel to the film normal. The slightly coarser nanocrystalline FePd films on crystalline NaCl substrates (Figure 93) exhibit a more complex texture, apparently comprised of multiple zone axis orientations of relatively high symmetry. In order to identify the orientations present in the experimental diffraction pattern for the FePd films on NaCl we compared them with computer simulations obtained with the commercial software package Desktop Microscopist from Virtual Laboratories (Figure 94).

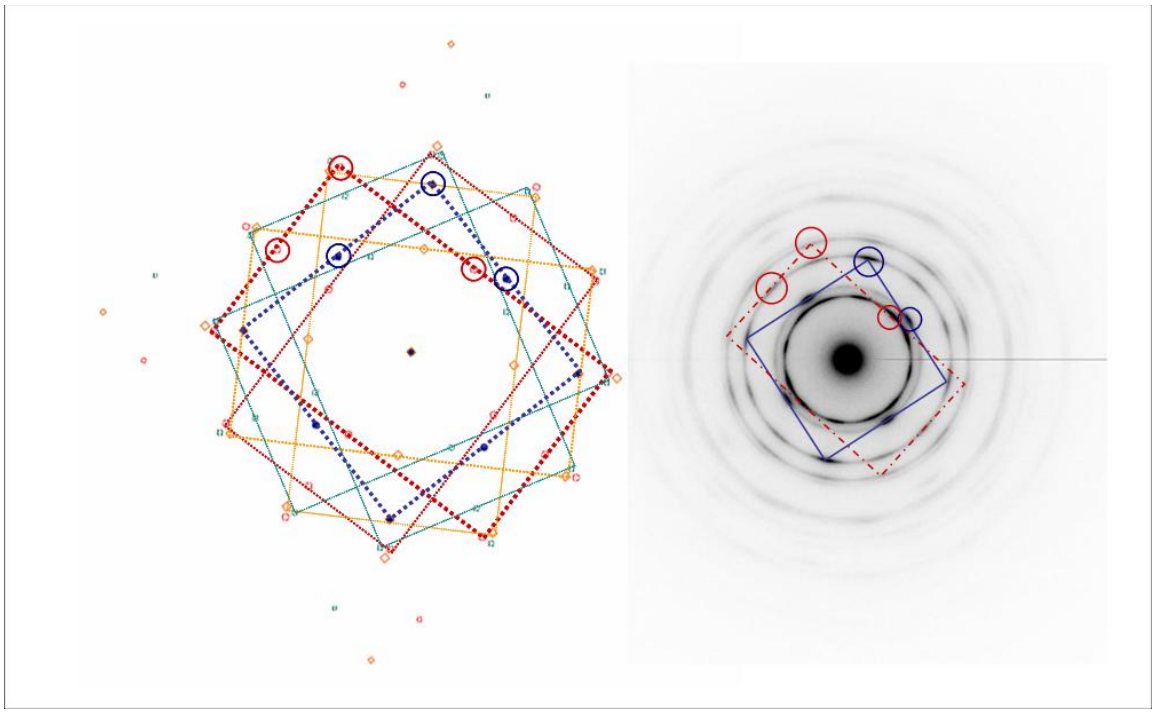

Figure 94. Simulated diffraction pattern of FePd on NaCl (on the left) as compared to inverted measured TEM diffraction pattern.

The simulation matching the main features of the experimental data has been obtained for the FCC FePd solid solution for superimposition of a [001] zone axis and six different <112>-type zone axes. The 111-type diffraction vectors associated with the six different <112>-zone axes are rotated 15° and 45° about the incident beam direction with respect to the 020-type diffraction vectors in the [001] zone axis. The 220-type diffraction vectors of the different <112>-zone axes are rotated by 30° with respect to each other about the incident beam direction. The equivalent points marked in Figure 94 clearly indicate that the main features of the distribution of the diffracted intensities in the experimental pattern are reproduced by the simulation. Thus, the model of the six <112> variants and a single <001> variant of the FCC FePd used in the simulation reasonably represents the approximate orientations of grains that are present in the FePd film on the crystalline NaCl substrate. The diffraction maxima in the experimental pattern are elongated into arches indicating rotational misorientations of the grains

representing the relevant different orientation variants of the FCC FePd after room temperature PLD on (100)-NaCl.

A.3.5 DISCUSSION

The grain sizes of the room temperature deposited PLD FePd films on the amorphous and on the crystalline substrates are about 7nm and 10nm, respectively. These grain sizes are of the same magnitude as reported previously for sputtered FePd thin films [87], [104].

The presence of a <111>-fiber texture parallel to the film normal in the FePd films deposited on amorphous SiO_2 and at least a fiber texture for those deposited on amorphous Si_3N_4 may be rationalized in terms of surface free energy minimization arguments. The {111} planes have the lowest surface free energy in FCC materials, and it is known [105] that the termination of many grains with {111} surface planes would be consistent with minimization of the total surface free energy.

The presence of a small volume fraction of $L1_0$-ordered phase in the films deposited on amorphous substrates suggests that there may be enhanced mobility processes active during deposition. An energetic flux such as with PLD can provide this mobility via transient diffusion upon arrival of adatoms at the surface [106] or other atomic displacement and sputter-related effects[107].These processes typically lead to enhanced surface transport, but at low substrate temperatures such as in the current experiments, volume and grain boundary diffusion likely remain unaffected. This probably results in a rather low volume fraction of $L1_0$-ordered material. This observation of some long range ordering in the room temperature PLD films contrasts with reports for sputter deposited thin films, which typically consist entirely of the FCC

high temperature phase [87]. Thus, it appears promising to explore further the PLD process parameters controlling the kinetic energy of the plasma plume of ablated target material on the thin film structure as well as the deposition rate.

The lack of $L1_0$-ordered phase in the films grown on crystalline NaCl substrate may be rationalized as follows. The available excess kinetic energy upon arrival on the substrate surface is exhausted by atomic rearrangements to achieve at least partial epitaxy during growth, as can be seen in the diffraction pattern (Figure 93, Figure 94) and hence, is insufficient for substantial concomitant long range ordering. The observation of the cube zone axis in the TEM diffraction patterns can be explained by possible lattice matching of FePd on NaCl, leading to some epitaxial growth. Relatively good lattice matching can be achieved if the {200} of FCC FePd are parallel to {200} of NaCl and <020> of FCC FePd are parallel to <022> of NaCl. The linear lattice mismatch along the <020> direction of FePd in this case is ~ 4.7% of the FePd lattice:

$$\frac{d_{020-FePd} - d_{022-NaCl}}{d_{020-FePd}} = \frac{\Delta d}{d}_{FePd[020]\|NaCl[022]} \approx 4.7\%$$

Here $d_{hkl\text{-}phase}$ is the lattice plane spacing along the indicated directions. Resulting strain could lead to slight tilts and hence deviations of the FCC FePd grain orientations from the cube zone axis. Those grains would, however, no longer contribute significantly to the diffraction pattern if the tilts exceed the magnitude of about twice the Bragg angle, ~0.8˚ for $d_{020FePd}$ and 200kV electrons. Hence, the arching observed in the diffraction pattern (Figure 91c and Figure 93c) is attributed to grains rotated with respect to each other essentially about the incident electron beam direction, here the film normal (Figure 93). Figure 95 schematically depicts a possible rotational degree of freedom of the FePd lattice on the NaCl lattice for

$(002)_{FePd}||(002)_{NaCl}$ which would be consistent with the experimental diffraction data (Figure 93). For such an arrangement of the FePd and the NaCl lattices the angular spread of the 200 type reflections of FePd would be expected to be about 14° to 16° (Figure 95). The slightly rotated cube oriented grains also cause their corresponding cube diffraction patterns to be rotated in reciprocal [107], consistent with the arches observed in experimental SADP.

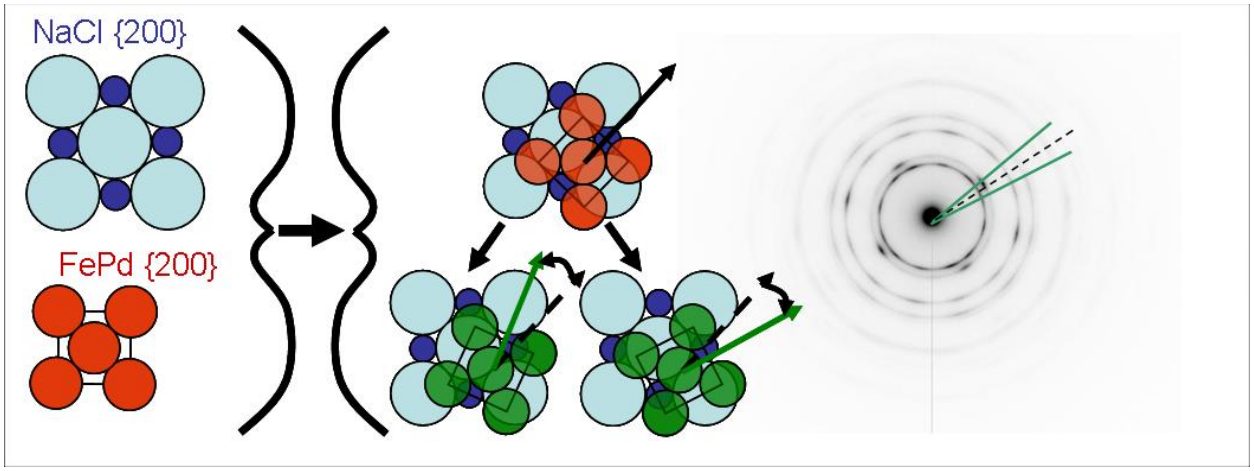

Figure 95. Schematic depiction of possible lattice matching and atom configurations for the FePd on NaCl thin film. Schematic depiction of a) the NaCl and FCC FePd unit cells in cube orientation; b) the lattice matching for the 45 degree rotated lattices in cube plane normal; c) angular range of arches associated with the 020 reflections in the experimental TEM diffraction pattern of about 16˚.

The presence of six different <112>- zone axes might be related to the formation of {111}-twins during growth through thickness. In such a crystallographic arrangement the twin conjugation plane {111} would be inclined by about 20° with respect to the sample surface in order for the {112} planes of the twin related orientation variants of the FCC FePd to remain parallel to the film surface. The tilt range of the TEM sample holder is insufficient to investigate this proposition further using plan view TEM samples of the thin films. Hence, cross sectional samples are required to best evaluate this working hypothesis by TEM experiments planned for the future.

A.3.6 SUMMARY AND CONCLUSIONS

Equiatomic FePd thin films have been successfully deposited on amorphous and crystalline substrates using PLD. The compositions of the deposited films are the same as the targets. The apparent average grain size is about 7 nm on amorphous and 10 nm on the crystalline substrates for the PLD processing conditions used here. The nature of the substrate strongly influences the resulting film microstructure. The FePd thin films deposited on amorphous substrates show the presence of fiber texture, confirmed as a 111-fiber for the amorphous SiO_2 substrates. Effects of epitaxy have been observed for the FePd films deposited on NaCl. These films represent useful starting conditions for future study of the influence of the different starting textures on the microstructural evolution during post deposition annealing and the phase transformation.

BIBLIOGRAPHY

1. M.F. Ashby: Acta Metallurgica, 20 p.887 (1972)
2. T.H. Courtney: Mechanical Behavior of Materials; McGraw-Hill p. 169-173 (1990)
3. J. Schoitz, K.W. Jacobsen, Science 301 p. 1357 (2003)
4. A.H. Chokshi, A. Rosen, J. Karch, H. Gleiter, Scripta Metallurgica 23 p. 1679 (1989);
5. H. Conrad, J. Narayan, Journal of Applied Physics Letters 81 p. 2241 (2002)
6. D. Wolf , V. Yamakov, S.R. Phillpot,A. Mukherjee, H.Gleiter: Acta Materialia 53 p.1-40 (2005)
7. P. Mulvaney: MRS Bulletin; p. 1009 -1014 (2001)
8. X. Zhang, C. Jia: Materials Science and Engineering (in press) (2006)
9. J. Weertman and J.R. Weertman: Elementary Dislocation Theory; Oxford University Press; New York, Oxford; p. 123-126 (1992)
10. K.S. Kumar, S. Suresh, M.F. Chisholm, J.A. Horton, P. Wang: Acta Materialia 51 p. 387–405 (2003)
11. M.A. Meyers et al.: Progress in Materials Science 51 p. 427–556 (2006)
12. Z. Shan et al.: Science 305 p. 654 (2004)
13. D. H. Warner et al.: Scripta Materialia (in press) 2006
14. F.H. Dalla Torre E.V. Pereloma, C.H.J. Davies.: Acta Materialia 54 p. 1135 -1146 (2006)
15. Meyers M, Ashworth E: Philosophical Magazine A 46 p. 737. (1982)
16. Kim HS, Estrin Y, Bush MB.: Acta Materialia 48 p. 493–504. (2000)

17. M. Zehetbauer T. Ungár, R. Kral, A. Borbély, E. Schafler, B. Ortner, H. Amenitsch and S. Bernstorff: Acta Materialia 47 p.1053-1061 (1999)

18. K.S. Kumar S. Suresh, M.F. Chisholm, J.A. Horton, P. Wang: Acta Materialia 51 p. 387–405 (2003)

19. Weertman JR, Sanders PG. Solid State Phenom; 249 p. 35–36: (1994)

20. Li: JCM. Trans Metallurgical Society; 227; p. 239 (1963)

21. Fu HH, Benson DJ, Meyers MA: Acta Materialia; 49 p. 2567–82 (2001)

22. B. Fultz, J. Howe: Transmission Electron Microscopy and Diffractometry of Materials; Springer Verlag Berlin, Heidelberg, New York p.72 (2001)

23. Cullity Elements of X-RAY DIFFRACTION (second edition); Addison-Wesley Publishing company, Inc.; p. 284-292 (1978)

24. Z. Budrovich et al.: Science 304 p. 273-276 (2004)

25. L. Tang et al.: Journal of Applied Crystallography 29 p. 411-418 (1996)

26. D.S. Gianola S. Van Petegem, M. Legros, S. Brandstetter, H. Van Swygenhoven, K.J. Hemker: Acta Materialia 54 p. 2253–2263(2006)

27. E. Thiele et al.: Materials Science and Engineering A 390 p. 42–51 (2005)

28. N. Yagi et al.: PHYSICAL REVIEW B 74, p. 144105 (2006)

29. A. V. Sergueeva et al.: Philosophical Magazine; Vol. 86, No. 36 p. 5797–5804 (2006)

30. D. Kuhlmann Wilsdorf: Philosophical Magazine A: Vol. 79, No. 4 p. 955-1008 (1999)

31. B.D. Cullity: Elements of X-RAY DIFFRACTION (second edition); Addison-Wesley Publishing company, Inc.; p. 296 (1978)

32. P.B. Hirsch, A. Howie, R. B. Nicholson, D.W. Pashley, M.J. Whelan: Electron Microscopy of thin crystals; London Butterworths p. 169, 343 (1965)

33. D. A. Hughes, N. Hansen.: Acta Materialia 48 p. 2985-3004 (2000)

34. L.J. Chen et al.: Physica Status Solidi (A): Vol. 25, Issue 1, p. 193-204 **(**1974**)**

35. C.V. Howard and M.G. Reed: Unbiased Stereology Three Dimensional Measurements in Microscopy; Bios Scientific Publishers Limited p. 4-6

36. R.J. McAfee, I. Nettleship: Scripta Materialia 52 p. 1281-1285 p. 1281-1285 (2005)

37. Saltykov SA: Stereometric metallurgy; English Translation by Technical Documents Liaison Office MCLTD, Wright-Patterson Air Force Base, Ohio (1961)

38. D.M. Schwartz: Journal of Microscopy 96 p. 25 (1972)

39. Bergenstof Nielsen et al.: Journal of Applied Electrochemistry: Vol. 27, Issue 7, p. 839-845 (1997)

40. E.A. Marquis et al.: Journal of Applied Electrochemistry: Vol. 36, Issue 6, p. 669-676 (2006)

41. H-R Wenk et al.: Reports on Progress in Physics; **67** p. 1367–1428 (2004)

42. T.H. Courtney: Mechanical Behavior of Materials; McGraw-Hill p. 169 (1990)

43. P.L. Gai et al.: Scripta Materialia 56 p. 25–28 (2007)

44. Zhang et al.: Journal of Applied Physics Letters 85 (22) p. 5197-9 (2004)

45. Zhang et al.: Journal of Applied Physics Letters 87 (6) p. 061921 (2005)

46. Zhu R.J. Asaro, P. Krysl, K. Zhang, J.R. Weertman: Acta Materialia 54 (12) p. 3307 – 3320 (2006)

47. L. Chang et al.: Scripta Materialia 56 p. 713–716 (2007)

48. M. Levlin, A. Laakso, H.E.M. Niemi and P. Hautojarvi, Appl. Surf. Sci. **115**, 31 (1997)

49. K.L. Tai, P.A. Turner and D.D. Bacon, J. Vac. Sci. Technol. **6**, 687 (1969)

50. N. Mancini and E. Rimini, Surf. Sci. **22**, 357 (1970)

51. K.K. Kakati and H. Wilman, J. Phys. D **6**, 1307 (1973)

52. M. Adamov, B. Perovic and T. Nenadovic, Thin Solid Films **24**, 89 (1974)

53. J.R. White, Thin Solid Films **22**, 23 (1974)

54. R.E. Hummel, R.T. DeHoff, S. Matts-Goho and W.M. Goho, Thin Solid Films **78**, 1 (1981)

55. M.S. Zei, Y. Nakai, G. Lehmpeuhl and D.M. Kolb, J. Electroanal. Chem **150**, 201 (1983)

56. J. Krim, Thin Solid Films **137**, 297 (1986)

57. C.C. Wong, H.I. Smith and C.V. Thompson, Appl. Phys. Lett. **48**, 335 (1986)

58. T. Jach, G. Hembree and L.B. Holdeman, Thin Solid Films **187**, 133 (1990)

59. Y. Golan, L. Margulis and I. Rubinstein, Surf. Sci. **264**, 312 (1992)

60. J. Hwang and M.A. Dubson, J. Appl. Phys. **72**, 1852 (1992)

61. M. Aguilar, A.I. Oliva, P. Quintana and J.L. Pena, Surf. Sci. **380**, 91 (1997)

62. D. Stamou, D. Gourdon, M. Liley, N.A. Burnham, A. Kulik, H. Vogel and C. Duschl, Langmuir **13**, 2425 (1997)

63. D.L. Everitt, W.J.W. Miller, N.L. Abbott and X.D. Zhu, Phys. Rev. B **62**, R4833 (2000)

64. N.G. Semaltianos and E.G. Wilson, Thin Solid Films **366**, 111 (2000)

65. R.D. Emery and G.L. Povirk, Acta Materialia **51**, 2079 (2003)

66. M.J. Rost, D.A. Quist and J.W.M. Frenken, Phys. Rev. Lett. **91**, 026101 (2003)

67. D.M. Mattox, J. Appl. Phys. **37**, 3613 (1966)

68. N. Schell, T. Jensen, J.H. Petersen, K.P. Andreasen, J. Bottiger and J. Chevallier, Thin Solid Films **441**, 96 (2003)

69. J.Y. Kwon, T.S. Yoon, K.B. Kim and S.H. Min, Journal of Applied Phys. **93**, 3270 (2003)

70. M. Adamov, B. Perovic and T. Nenadovic, Thin Solid Films **24**, 89 (1974)

71. H.J. Scheibe, A.A. Gorbunov, G.K. Baranova, N.V. Klassen, V.I. Konov, M.P. Kulakov, W. Pompe, A.M. Prokhorov and H.J. Weiss, Thin Solid Films **189**, 283 (1990)

72. E. Irissou, B. Le Drogoff, M. Chaker and D. Guay, Journal of Applied Physics **94**, 4796 (2003)

73. E. Irissou, B. Le Drogoff, M. Chaker and D. Guay, Applied Physics Letters **80**, 1716 (2002)

74. E. Irissou, B. Le Drogoff, M. Chaker, M. Trudeau and D. Guay, J. Mater. Res. **19**, 950 (2004)

75. P.B. Barna and M. Adamik, Thin Solid Films **317**, 27 (1998)

76. C.V. Thompson, Ann. Rev. Mater. Sci. **30**, 159 (2000)

77. S. Rossnagel, in Handbook of Thin-Film Deposition Processes and Techniques (K. Seshan ed.) Ch. 8, 319 (2002)

78. Y. Franghiadakis, C. Fotakis and P. Tzanetakis, Appl. Phys. A **68**, 391 (1999)

79. D.B. Chrisey, G.K. Hubler, Pulsed laser deposition of thin films, Wiley (1994)

80. O. Kubaschewski, Iron – Binary Phase diagrams (Berlin,: Springer – Verlag, 1982) 88-91

81. M. Sugiyama et al.: Materials Transactions, JIM 25 (1984) pp. 585-592

82. H. Xu et al.: Intermetallics 11 (2003) 963–969

83. A.R. Deshpande et al.: Scripta Materialia 54 (2006) 955–960

84. T. Klemmer et al.: Scripta Metallurgica et Materialia, Volume 33, Issues 10-11, 1 December 1995, Pages 1793-1805

85. Z. Wang et al.: Materials Transactions, JIM, Vol. 41, No 9 (2000) pp. 1139 – 1141

86. Y. Sugimura et al.: J. Mater. Res., Vol. 20, No 9, Sep 2500, pp. 2279 – 2287

87. H. Xu et al.: Intermetallics 11 (2003) 963–969

88. A.R. Deshpande et al.: Scripta Materialia 54 (2006) 955–960

89. T. Klemmer et al.: Scripta Metallurgica et Materialia, Volume 33, Issues 10-11, 1 December 1995, Pages 1793-1805

90. M. Sorescu et al.: Intermetallics 14 (2006) 780–783

91. J. L. Menéndez et al. :Journal of Magnetism and Magnetic Materials, Volume 206, Issues 1-2, November 1999, Pages 1-7

92. A. Cebollada et al.: Journal of Magnetism and Magnetic Materials, Volume 203, Issues 1-3, August 1999, Pages 162-164

93. A. Asenjo et al.: Journal of Magnetism and Magnetic Materials, Volumes 196-197, 1 May 1999, Pages 23-25

94. P. Caro et al.: Acta Materialia, Volume 46, Issue 7, 10 April 1998, Pages 2299-2303

95. Z. Wang et al.: Materials Transactions, JIM, Vol. 41, No 9 (2000) pp. 1139 – 1141

96. P. Kamp et al.: Physica B: Condensed Matter, Volume 248, Issues 1-4, 15 June 1998, Pages 127-132

97. V. Gehanno et al.: Journal of Magnetism and Magnetic Materials, Volume 172, Issues 1-2, 1 August 1997, Pages 26-40

98. D. Halley et al.: Surface Science, Volume 481, Issues 1-3, 10 June 2001, Pages 25-32

99. B. Gilles et al. MRS Symp. Proc. Vol. 615 G.1.7.1 (2000)

100. A. Kulovits et al.: MRS Symposium Proceedings Vol. 980 2007 in print

101. Tang L, Laughlin DE.: J Appl. Cryst. 1996;29:411.

102. L. Tang et al.: Materials Research Society Symposium - Proceedings 562, pp. 105-116

103. Y. Sugimura et al.: J. Mater. Res., Vol. 20, No 9, Sep 2005, pp. 2279 – 2287

104. E. Grantscharova: Thin Solid Films 224, 28 (1993).

105. B. Shin, J.P. Leonard, J.W. McCamy and M.J. Aziz, : Appl. Phys. Lett. 87, 181916 (2005)

106. G.H. Gilmer and C. Roland: Appl. Phys. Lett. 65, 824 (1994).

107. C. Herring; Structure and Properties of Solid Surfaces, University of Chicago Press, Chicago, 1953, p. 5.